Microchemical Systems for the Synthesis of Nanostructures: Quantum Dots

by

Jinyoung Baek

B.S. Chemical and Biological Engineering, Seoul National University, 2007
M.S. Chemical Engineering Practice, Massachusetts Institute of Technology, 2009

Submitted to the Department of Chemical Engineering
in Partial Fulfillment of the Requirements for the Degree of

Doctor of Philosophy
at the

MASSACHUSETTS INSTITUTE OF TECHNOLOGY

May 2012

Signature of Author..
Department of Chemical Engineering
May 21, 2012

Certified by.. .... Klavs F. Jensen
Professor of Chemical Engineering
Thesis Supervisor

Accepted by.................................. ... Patrick S. Doyle
Professor of Chemical Engineering
Chairman, Committee for Graduate Students

Microchemical Systems for the Synthesis of Nanostructures: Quantum Dots

by

Jinyoung Baek

Submitted to the Department of Chemical Engineering
on April 23, 2011 in partial fulfillment of the requirements for the degree of
Doctor of Philosophy in Chemical Engineering

Abstract

We have developed a continuous multi-stage high-temperature and high-pressure microfluidic system. High-pressure conditions enabled the use low molecular weight solvents that have previously not been available for quantum dot (QD) synthesis such as hexane or octane. The use of supercritical phase provided excellent mixing, which was critical in producing high quality QDs. In addition, the microfluidic system allowed precise control of synthetic conditions for the fast screening of reaction parameters. The continuous multi-stage microfluidic system enabled separating of reaction conditions such as mixing and aging steps, which was not possible in batch synthesis, as a result it was possible to conduct systematic investigation of the synthesis of indium phosphide (InP) QDs.

We investigated synthesis of InP QDs with a continuous 3-stage high-temperature and high-pressure microreactor system without incorporating any batch manipulations between the synthesis steps. By separating the mixing process from the following aging process, we found that InP QD synthesis were mainly dominated by coalescence processes. Indium to fatty acid ratio showed the largest effect on particle size due to enhanced inter-particle processes. Concentrations or mixing temperatures changes, which are important reaction parameters of cadmium selenide (CdSe) QD growth, had no significant impact.

We also synthesized larger (>3.2 nm) InP QDs with a sequential injection microreactor consisting of 6 sequential alternative monomer injections similar to the successive ion layers adsorption and reaction (SILAR) method. We obtained InP QDs with size distributions as narrow or narrower than the InP QDs synthesized via the ripening process.

Indium phosphide / zinc sulfide (InP / ZnS) core-shell QDs were obtained with a 5 or 6 -stage microreactor system consisting of additional shell growth reactors, in addition to the three-step InP growth system. We were able to obtain narrow emissions with high quantum yield. This system was also used for the synthesis of indium phosphide / cadmium sulfide (InP / CdS), indium arsenide / indium phosphide (InAs / InP), and indium arsenide / cadmium sulfide (InAs / CdS) core-shell QDs.

We also investigated the growth of InAs QDs using the same system for InP QD synthesis. We found that the InAs growth from indium myristate ($In(MA)_3$) and tristrimethylsilyl arsine ($(TMS)_3As$) precursors showed similar behavior as InP growth. However, different from the growth of InP nanocrystals, the amount of excess fatty acid did not affect on the growth of InAs nanocrystals.

Indium phosphide arsenide (InP_xAs_{1-x}) alloy nanocrystals were also synthesized by precise control of phosphorus (P) and arsenic (As) precursor amounts. Mixing two anionic and cationic precursors at an elevated temperature followed by fast heating up to the reaction zone is very important for InP_xAs_{1-x} alloy nanocrystal synthesis. A multi-stage microfluidic system with a mixing reactor with gradient temperature was a useful tool for this synthesis. InP_xAs_{1-x} alloy nanocrystals were characterized with optical measurements and wide angle X-ray diffraction scattering.

We investigated growth of InAs nanocrystals from a less reactive arsenic precursor, tris(trimethygermyl) arsine (TMG_3As). We obtained InAs nanocrystals with better size distribution than those synthesized from TMS_3As. We also compared the growth behavior of InAs nanocrystals synthesized from those two different arsenic precursors. With TMG_3As, we observed a growth behavior potentially following a similar nucleation and growth model to that of growth of II-VI QDs.

Thesis Supervisor:	Klavs F. Jensen
Title:	Department Head, Chemical Engineering
	Warren K. Lewis Professor of Chemical Engineering
	Professor of Materials Science and Engineering

Acknowledgments

First and foremost, I would like to express my gratefulness to Professors Klavs Jensen, Moungi Bawendi, and Michael Strano for their help, advice, and support, as well as encouragement throughout my PhD career. Klavs has been an encouraging mentor, always providing me with the big-picture and ultimate goals of the project. Moungi provided experimental and theoretical backgrounds of nano-materials as well as perspective in chemistry field. I would also like to thank Michael, as a member of my thesis committee. He always provided good approaches to solve problems in my projects.

My decision to pursue a graduate degree in Chemical Engineering was largely influenced by the great mentorship that I received from Professor Kookheon Char at Seoul National University; he provided me with a great opportunity to work on as an undergraduate researcher in his group.

I would like to acknowledge the US Army Research Office through the Institute for Soldier Nanotechnology (ISN), the US National Science Foundation, and Samsung scholarship from the Samsung Foundation of Culture for their financial support.

All the members in the Jensen group and Bawendi group made me feel very comfortable during my graduate life. Guidance from Samuel Marre and Jongnam Park was very helpful in familiarizing myself with my graduate research in the beginning. Discussions with Andrea Adamo, and Lei Gu about microfabrication processes were notably invaluable. Research discussions with Peter Allen and Daniel Harris, helped me to deepen my knowledge in chemical synthesis and mechanisms. All the Jensen group members, Kevin Nagy, Seung-kon Lee, Baris Unal, Jason Moore, Patrick Heider, Vicki Dydek, Jerry Keybl, Chris Marton, Everett Oneal, Simon Kuhn, Stephen Born, Armon Sharei, Tatyana Shatova, Maria Jose Remacha, Jen Lee, Xiaoying Liu, Sidy Ndao, Brandon Reizman, Jonathan McMullen, Nikolay Zaborenko, Hemant Sahoo, Ling Chao, Soubir Basak, and Flurin Hanseler were very nice, and daily discussions with them were very helpful for me. I appreciate to Shuo Wang, an undergraduate student, for her help. She helped me for 8 month, and was very productive. It was great time to discuss with and hang out with all the Bawendi group members, Hee-Sun Han, Raoul Correa, Jose Cordero, Jian Cui, Russ Jensen, Liang-Li Chang, Gyu Weon Hwang, Ou Chen, Cliff

Wong, Dorthe Eisele, Jie Bao, Oliver Bruns, Andrew Beyler, Jennifer Scherer, Tara Sarathi and Darcy Wagner. Two ski trips at the Killiongton were unforgettable in my life. I also thank members of the staff at MIT: Suzanne Maguire, Alina Haverty, Li Miao, and Joel Dashnaw, who were always willing to listen and help.

Finally I want to thank my family and friends, especially our classmates, friends in the chemical engineering department, in the GSC, and in the Sidney-Pacific community for their support and encouragement.

Table of Contents

List of Figures

List of Tables

Chapter 1

Introduction and Motivation

1.1. Introduction to microfluidic system

Microreactor systems provide enhanced mass and heat transfer, feedback control, and excellent reproducibility.[1-5] The small reaction volumes combined with the fast heat and mass transfer rates allows for fast or extremely exothermic reactions that are not easily performed in conventional batch reactors due to the limit in mixing or safety issues.[4-5] This small volume also allows for the low consumption of reagents while finding optimal production conditions. Low consumption of the reagents has been important for productions of high value products from expensive reagents or from reagents that are hard to handle in large scale due to toxicity or danger of explosion.[4, 6-7] The microfluidic system can be modified to include in-line sensors such as a UV-Vis absorption spectrometer or a dynamic light scattering (DLS).[8-9] These in-line systems offer fast screening of reaction parameters, as well as provide feedback control to find optimal production conditions.

Batch synthesis often suffers from inherit drawback such as irreproducibility of nanomaterial qualities from batch to batch since injection rates, local temperatures and concentrations, and cooling rates are not easily controllable.[5] Therefore, a microfluidic system offers better opportunities for synthesis of inorganic nanomaterials with uniform and tunable size distribution than batch system. A microfluidic system is also a useful tool for the synthesis new materials as well as for investigation of nanocrystal growth mechanisms.[9-12] The synthesis of new nanostructures of materials such as III-V semiconductor nanocrystals often involved the use of toxic and highly reactive precursors.[9, 13-18] Therefore, microfluidic systems are well suited for the investigation of growth of semiconductor nanocrystals.[9, 19]

1.2. High-pressure and high-temperature system

Microreactor systems using a single-phase or segmented flow at atmospheric pressure have been introduced for the synthesis of inorganic materials such as CdSe.[11-12] Since the system is operating at ambient pressure, the choice of solvent selection has been limited to the same solvents typically used in a batch system. These solvents need to dissolve the precursors at room temperature, and need to remain liquid at the reaction temperature. Considering that typical reaction temperature for inorganic synthesis such as CdSe, CdS, or ZnS synthesis is at high temperature, typically between 250 °C and 360 °C, solvents with high molecular weights have been commonly used: 1-octadecene as a non-coordinating solvent, or oleylamine or trioctylphosphine oxide (TOPO) as coordinating solvents. In some cases, polymer solvents such as polyethylene glycol have also been used.[20] However, those solvents are typically very viscous, which results in poor mixing and a broad residence time distributions (RTD). Segmented flow created by using two immiscible phases such as liquid-gas or liquid-liquid provides better mixing than the single-laminar flow, but flow segmentation is not enough for some fast reactions. The broad RTD leads to broad size distribution of inorganic nanoparticle products.

High-pressure microfluidic system allows for usage of a broad range of solvents, precursors and ligands not accessible in a conventional batch synthesis system (figure 1.1).[8-9] Solvents with low molecular weight such as pentane, hexane or octane remain either liquid or supercritical (sc) phase at the reaction temperature for nanomaterials synthesis.[9-10, 21] Gas phase reactants such as hydrogen sulfide or ammonia could also be used for nanomaterial synthesis, sulfur source or nitrogen sources respectively.[22]

Figure 1.1 shows that the pressure – temperature phase diagram of a pure solvent. In particular, supercritical phase allows tuning the density of a fluid from gas-like to liquid-like.[21] This phase provides fast diffusion rates typical of gases and sufficient densities to solubilize a variety of precursor or ligand compounds. The resulting expanded set of reaction conditions opens opportunities for synthesis of nanostructures not easily achieved in batch.

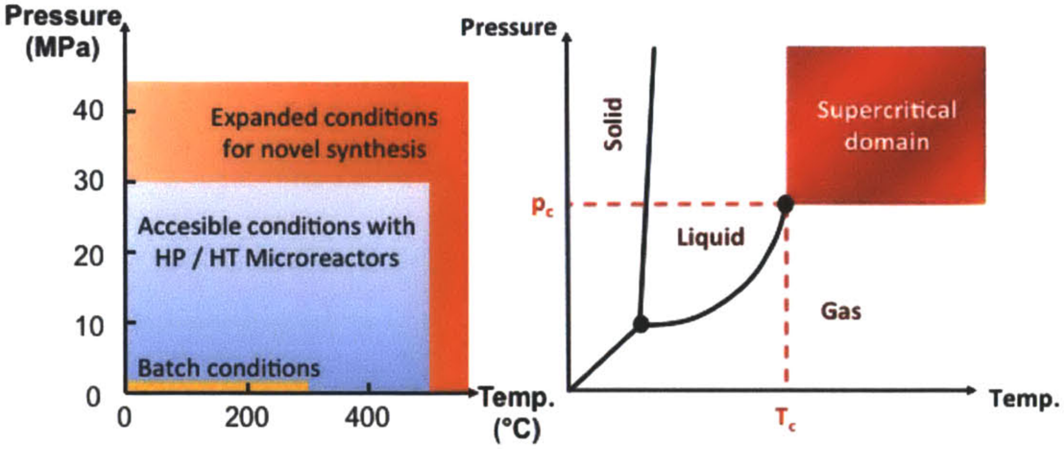

Figure 1.1: Pressure / Temperature diagram with typical batch conditions and potential on chip processes using microfluidic systems operating at high-pressure and high-temperature.

The silicon-based microreactor can withstand high-pressure and high-temperature, but connecting microreactors to high-pressure pump without leaks has been a challenge.[5, 9-10, 23] Development of an interface system (packaging) with leak tight connections has enabled the realization of a microfluidic system operating at a high-pressure and a high-temperature (figure 1.2).[23] The microreactor is mounted on a water cooled compression part. The cooling water is always maintained at 25 °C. The compression part (figure 1.3) has four O-rings at the interface between the silicon surface of the microreactor and the stainless steel compression part. The o-rings can be changed based on the chemical compatibility. Viton is typically used for aliphatic organic materials and Kalrez perfluoroelastomer for aromatic compounds. The temperature of the microreactor is controlled with an aluminum heating block.[5, 8, 23] The details of the design will be described in Chapter 2. A 0.8 mm graphite sheet was inserted in between the silicon surface and aluminum in order to maintain uniform temperature along the reactor surface. High-pressure pumps were connected to the compression part and used to inject the reagents into the microreactor. The product stream flowed to the in-line measurement device such as in-line UV-Vis (figure 1.2) and was collected in a chamber that was maintained at high pressure.[9]

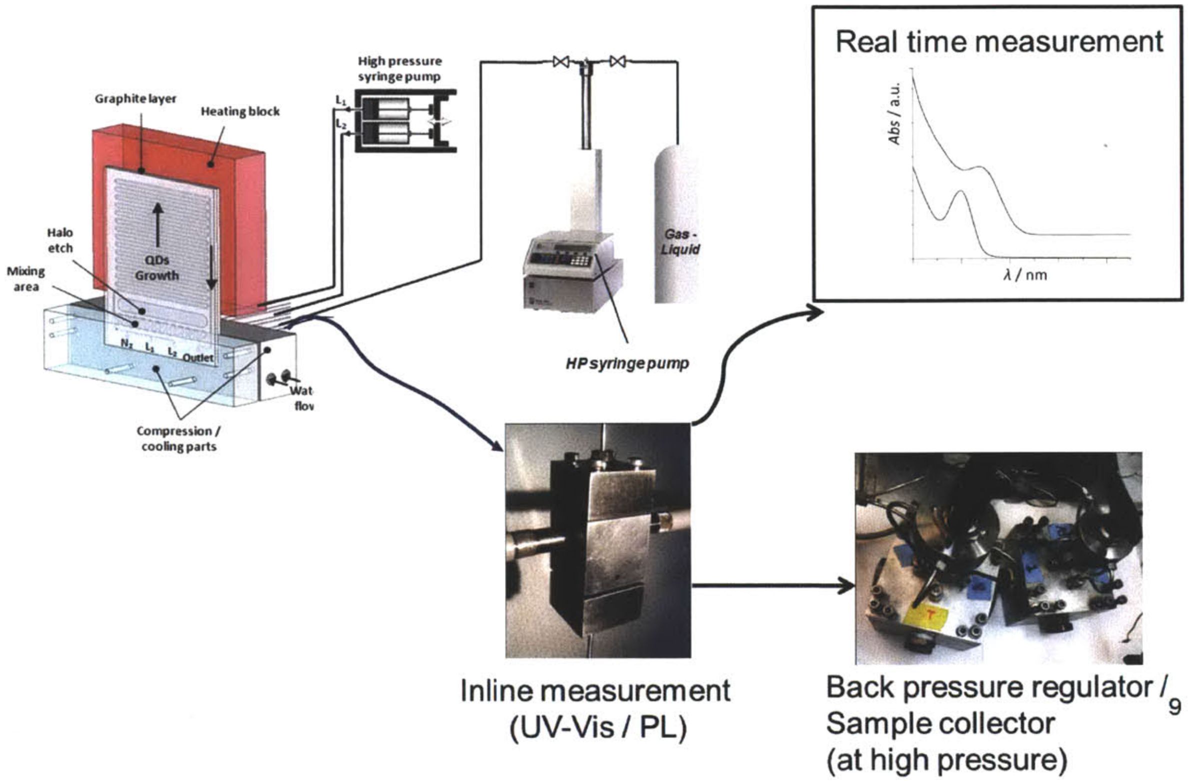

Figure 1.2: High pressure and high temperature microfluidic system for chemical synthesis combined with in-line measurement device. Adapted from the reference 9, and edited.

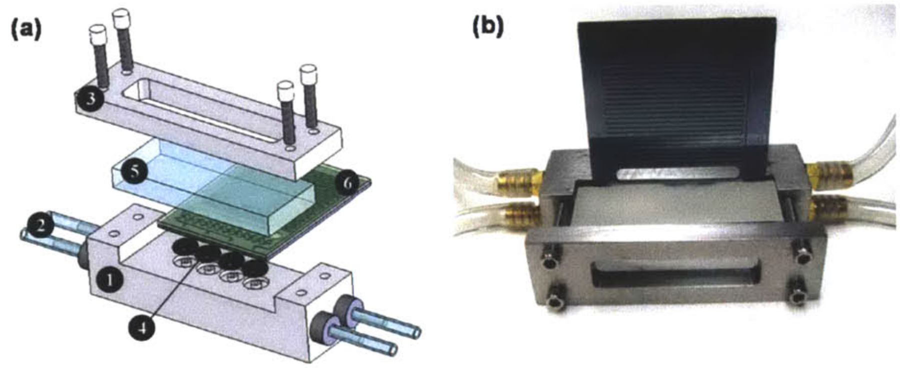

Figure 1.3: (a) Assembly of microreactor system: (1) a compression part, (2) tubes for cooling water, (3) a cover, (4) O-rings, (5) a Pyrex cover glass, and (6) a microreactor. (b) A picture of a microreactor mounted on to the compression part. Adapted from the reference 24.

The in-line measurement allows for fast optimization of the microfluidic system. In-line UV-Vis systems (figure 1.2) can be integrated with control algorithms, and find a optimal condition for the production of the desired products (figure 1.4). The details of the in-line device will be described in Chapter 2. This system allows for collecting reaction space-resolved information. In-line measurements are not limited to optical measurements such as (UV-Vis, IR, or Raman) but can also include physical measurements (e.g., thermocouples and piezo electric pressure sendors). Other in-line measurements such as dynamic light scattering (DLS) or particle image velocimetry (PIV), which provides information about particle size distributions and flow profiles, also can be integrated into the microreactor system.[5] By combining these in-line characterization devices with optimization software, high-pressure and high-temperature microfluidic systems can be utilized for process optimization.[24]

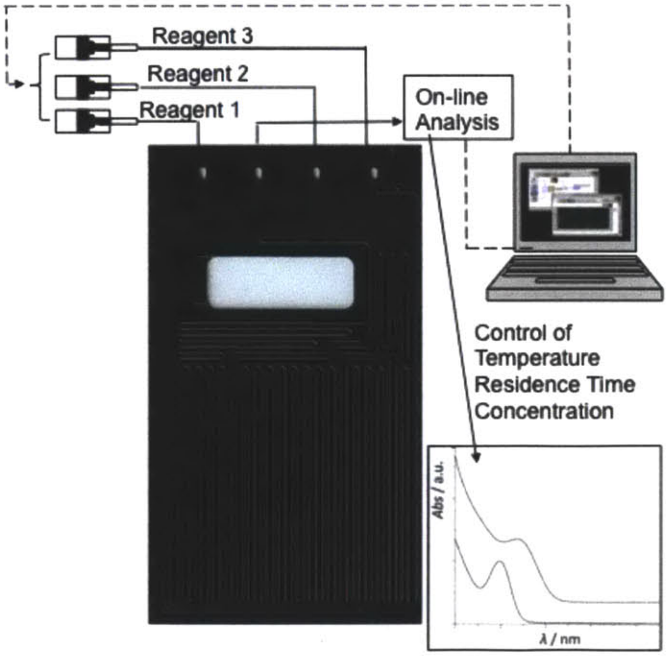

Figure 1.4: General scheme of an in-line high-pressure and high-temperature optimization set-up.

1.3. Semiconductor nanocrystals (Quantum Dots)

1.3.1. Properties and applications

Semiconductor nanocrystals (quantum dots) have been of great interest due to their tunable optical and electronic properties with particle size.[25-28] As the size decreases, the number of the molecular orbitals decreases, and therefore, the band-gap energy increases. This band-gap energy change is one of the main reasons of the tunable properties. This energy tuning is normally observed when the particle size is reduced to several nanometers for most semiconductors.

After a semiconductor material absorbs photons under the right conditions, it generates an electron-hole pair, called an exciton. The radius of a free exciton (Wannier-Mott exciton) is much larger than the atomic spacing of a material. We can observe quantum confinement effect when the physical size of the particle is smaller than Bohr exciton radius of the bulk material.[29] Table 1.1 is a list of band gap energies and Bohr radius of several semiconductor materials.

Table 1.1: Band gap energies and Bohr radiuses of several direct band gap semiconductor compounds. Adapted from the reference 30.

Crystal	Material Group	Band Gap (eV)	Bohr Radius (nm)
GaN	III-V	3.5	3.1
ZnSe	II-VI	2.8	4.5
CdS	II-VI	2.6	2.7
ZnTe	II-VI	2.4	5.5
CdSe	II-VI	1.8	5.4
CdTe	II-VI	1.6	6.7
GaAs	III-V	1.5	13
InP	III-V	1.4	12
GaSb	III-V	0.8	23
InSb	III-V	0.2	100

In figure 1.5, as the particle radius become below the Bohr radius, the energy structure becomes discretized. Under strong spatial confinement condition, the reciprocal lattice vector (**k**) is no longer a good quantum number. Therefore, the processes of intraband and interband relaxation are modified. The time for the exciton energy decay by thermal processes involving phonon vibration becomes longer. Therefore, the thermal energy decay process of the exciton is slowed down. This enables a process called multi-exciton generation (MEG). An exciton that has at least twice the energy of the band-gap can generate two excitons, each of which has half of the original exciton energy.[30-31] Due to the MEG process, it is reported that the quantum efficiency of a quantum dots is over 100%.[32]

As another unique property of quantum dots, the electron-hole pair is no longer correlated since the pair is strongly confined in a space. In a free space, when a hole or an electron moves around, the other one follows it. However, under a confined geometry, the confinement effect becomes much greater than the electronic force between an electron and a hole, and therefore, the electron and hole pair becomes uncorrelated.[29]

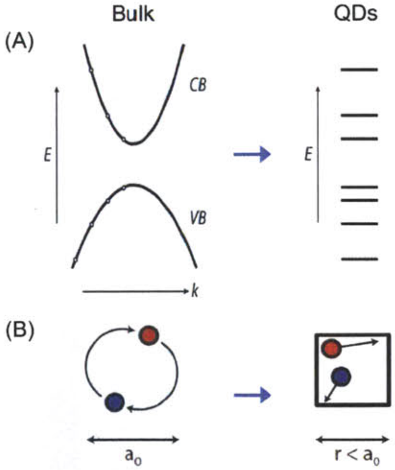

Figure 1.5: (a) Energy level becomes discretized as the size of the size of the material decreases. (b) Under strong confinement atmosphere, electron-hole pair is uncorrelated.

Due to the quantum confinement effect described above, optical and electronic properties of the materials are very sensitive to the size. Figure 1.6 is a series of absorption spectra of cadmium selenide (CdSe). As the size of the CdSe nanocrystals decreases, the first absorption feature shifts to blue.[25-26] This quantum confinement effect can also be found from other semiconductor materials. Figure 1.7 is the absorption spectra of a size series of indium arsenide (InAs) nanocrystals.[33]

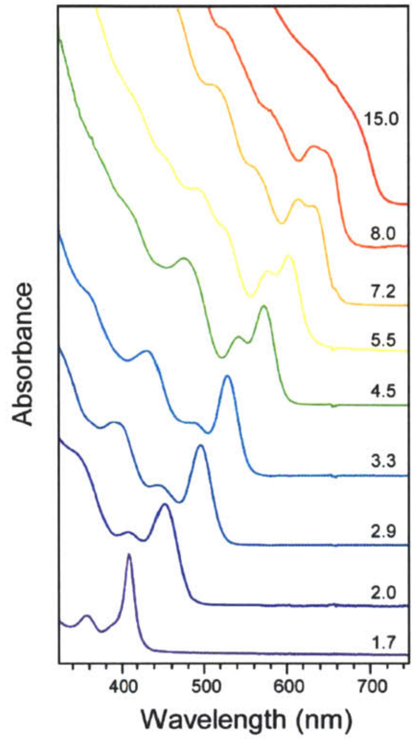

Figure 1.6: Absorbance spectra of CdSe quantum dots with different sizes. The corresponding average diameters (nm) of the quantum dots are shown at each spectrum. Adapted from Murray, C. B. Ph.D. Thesis, Massachusetts Institute of Technology, Cambridge, MA, 1995.

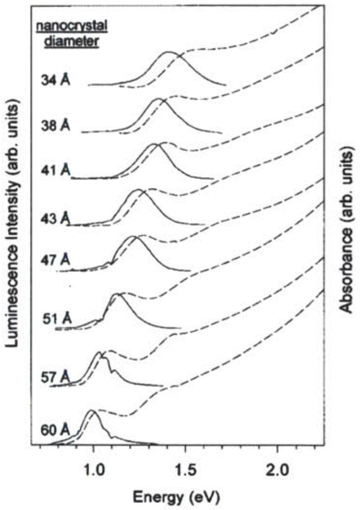

Figure 1.7: Absorbance spectra of InAs quantum dots. The corresponding average diameters (nm) of the quantum dots are shown at each spectrum. Adapted from the reference 34.

In addition to size-dependent properties, quantum dots have narrow emission spectra compared to typical organic fluorophores. This narrow emission can be used in lighting and displays to achieve high color saturation. The enhanced color saturation is critical for applications such as displays, and also potentially increases electrical efficiency of display devices. These most display panels use optical filters to obtain pure RGB color, and narrow emissions increase the filtering efficiency.

Quantum dots have great photostability, and therefore they are a good material for bio-imaging applications.[28] Core-shell structured quantum dots[34-41] have better checmial resistantace than typical organic fluorophores. By attaching co-polymer surfactants[42] to the surface of the quantum dots, quantum dots can be a sensor or an indicator of different chemical environments in an animal body. In addition to those applications described in this section, quantum dots have been also studied for other applications such as light emitting devices and lasers.[43-50]

1.3.2. Core-shell quantum dots

As synthesized, quantum dot surfaces are typically passivated with organic molecules, called ligands (figure 1.8). Since the sizes of the quantum dots are only a several nanometers in diameter, the surface-to-volume ratio is very high. Therefore, the quantum dot surface needs to be surrounded by protecting materials. Organic ligands protect quantum dot surfaces by forming complexes between the surface atoms and the ligands. However, most cases, the organic ligands do not effectively protect quantum dot cores, and therefore, the exciton in a quantum dot is exposed to surface related trap states. These trap states induce fast non-radiative energy loss, so the quantum efficiency of the quantum dots is significantly reduced.

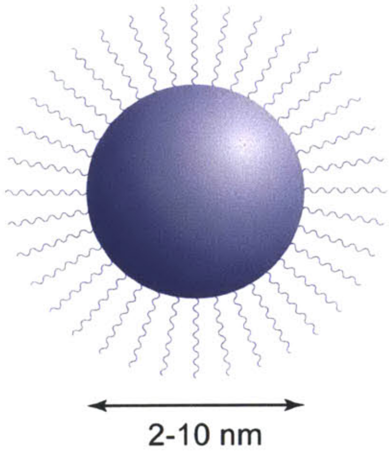

Figure 1.8: Cartoon of a nanocrystal consisting of the quantum dot core and a layer of organic ligands. Adapted from Yen, B. Ph.D. Thesis, Massachusetts Institute of Technology, Cambridge, MA, 2007.

In order to improve the quality of the surface passivation an inorganic shell is typically grown on the core of the quantum dots. This is called a core-shell structure. As an example, figure 1.9 is an illustration of an InP quantum dot and an InP / ZnS core-shell quantum dot. The shell effectively confines the exicitons in the core quantum dots, and therefore the quantum efficiency increases. Also, the stability against photo-oxidation is significantly improved.

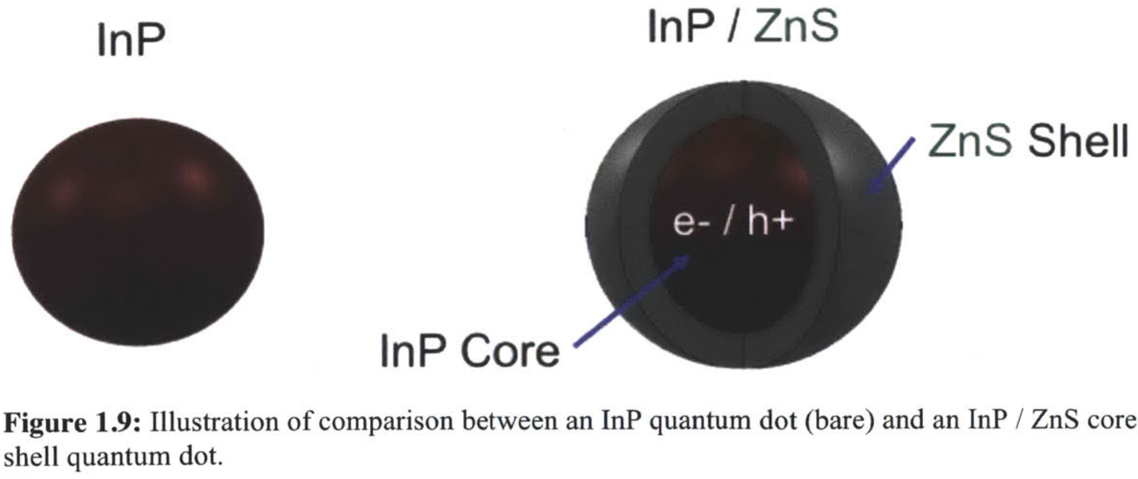

Figure 1.9: Illustration of comparison between an InP quantum dot (bare) and an InP / ZnS core-shell quantum dot.

In order to protect the core, the shell needs to grow epitaxially on the core material since defects existing at the interface between the core and the shell act as trap states. For the epitaxial growth, the difference of the lattice constants of between the core material and the shell material needs to be very small. Also, the crystal structures of the two materials need to be compatible. An additional shell also can be grown for the even better protection for the QD system.

Core-shell quantum dots are divided into three types based on the alignment of band gaps of between the core and the shell: type I, type II, and reverse type I (figure 1.10).[51] In the type I, the band gap of the core material is smaller than that of the shell, and therefore the exciton is confined to the core. The shell acts as a protective layer on the surface of the core. Due to the effective exciton confinement in the core, this type I core-shell quantum dots shows improved quantum efficiency. Typically the shell material has high photo-stability, and therefore this quantum dots show improved stability against photo-degradation. An example of a type I core-shell quantum dot structure is ZnS on CdSe.[35]

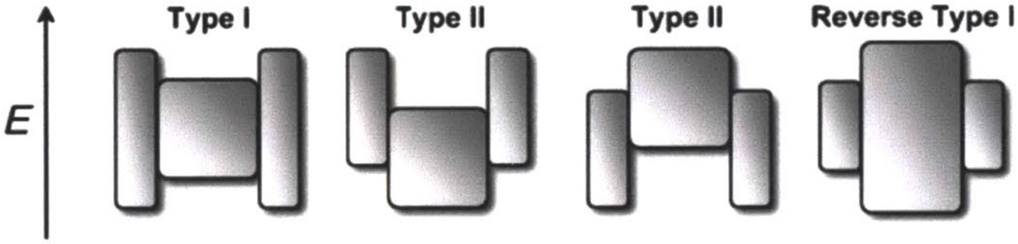

Figure 1.10: Schematic of the energy level alignments in type I, type II, and reverse type I core-shell quantum dots.[34]

In the type II, energy levels of both the valence band and conduction band of the shell material align either higher or lower than those of the core material. One of the electron or hole stays in the core, and the other stays in the shell. This electron-hole separation leads to a smaller effective band gap than either the core or the shell material. Therefore, the thicker shell growth causes a red-shift of the absorption and emission spectra.[52] Owing to the lower overlap of the electron and hole wavefunctions, photoluminescence decay times are significantly prolonged.[51] Since either electron or hole locates in the shell material, this type II core-shell quantum dots needs to be protected with another high band gap materials in order to improve the quantum efficiency.

The band alignment of the reverse type I is the opposite of the type I core-shell quantum dots. The exciton is confined only in the shell. Since the shell thickness is tunable from very small (sub nanometers) to several nanometers, the band gap energy is greatly affected by the shell thickness. Those core-shell quantum dots also need another protective layer with high band gap material to confine the exiton.[53]

1.3.3. Ostwald ripening

Investigation of particle growth is very important to obtain highly crystalline and monodisperse quantum dots. Previously, Yen, B. (Ph.D., Massachusetts Institute of Technology) summarized the classical nucleation and growth model of II-VI nanocrystal growth in his thesis.[54-55] Therefore, we include a short introduction of Ostwald ripening [56] which lead to growth of larger particles at the expense of smaller particles. Ostwald ripening of the formed nanocrystals appears to be particularly important in the growth of III-V nanocrystals, the topic of this thesis.

The Ostwald ripening is a particle growth process by interactions between existing particles. From the Gibbs-Thomson relation (eq. 1.1), the smaller particles have higher solubility.

$$C_r = C_\infty \exp\left(\frac{2\gamma V_m}{rRT}\right) \qquad \text{Eq. 1.1}$$

C_r is the size dependent solubility, C_∞ is the solubility concentration for a flat surface, γ is surface energy, V_m is the molecular volume, and r is the radius of the particle. This size dependent solubility is the cause of the Ostwald ripening.

This Ostwald ripening can be controlled either by the diffusion rate of the solute or the growth / dissolution reaction. Once the solute diffusion controls the ripening, the size distribution function in steady state of growth and dissolution follows eq. 1.2.

$$f(r,t) = \frac{constant}{\left(1+\frac{t}{\tau_D'}\right)^{\frac{4}{3}}}\rho^2\left(\frac{3}{3+\rho}\right)^{7/3}\left(\frac{3/2}{\frac{3}{2}-\rho}\right)^{11/3}\exp\left(\frac{-\rho}{\frac{3}{2}-\rho}\right) \qquad \text{Eq. 1.2}$$

If the Ostwald ripening is controlled by reaction, by assuming that both the dissolution and growth are first-order reaction with the same reaction constant, the size distribution function is given by eq. 1.3

$$f(r,t) = \frac{constant}{\left(1+\frac{t}{\tau_R'}\right)^{2}}\rho\left(\frac{2}{2-\rho}\right)^{5}\exp\left(\frac{-3\rho}{2-\rho}\right) \qquad \text{Eq. 1.3}$$

ρ is r/r^*,and t is time. τ_R' and τ_D' are time constants. r^* is the particle radius at equilibrium with the solute. r is the radius of the particle.

Ac actual growth process is likely to be more complex. The diffusion of solute and surface reactions could be coupled. The dissolution rate or particle growth rate probably do not follow a first-order reaction model. Systematic investigations of the particle growth are needed to understand the growth of nanocrystals with narrow size distributions.[57]

1.3.4. Successive Ion Layer Adsorption and Reaction (SILAR)

Successive ion layer adsorption and reaction (SILAR)[37] is a method for shell formation on the core nanocrystals by multiple injections of monomers; anoinic and cationic precursors are alternately injected into the core. Since the cationic and anionic monomer precursors do not coexist with each other in the reaction vessel, undesired nucleation is naturally suppressed. Therefore, half a monolayer of a shell is formed at each injection, and the shell growth on the core surface is very uniform. The excellent shell quality provides up to unity quantum efficiency. Usually the precursors of the shell materials are air-stable and inexpensive. An example of the core-shell nanocrystal made using this SILAR method is CdSe / CdS.[37]

In the SILAR method for syntheses of CdSe / CdS core-shell nanocrystals, the CdSe core is purified to remove all the unreacted monomers in the solution. The core is re-dispersed in 1-octadecene with oleylamines, and heated up to the desired shell formation temperature. Since all the cadmium and selenium monomers are removed, the CdSe core is not growing further at the shell formation temperature, between 160 °C and 240 °C. This temperature is also not high enough to promote Ostwald ripening of the particles within several hours.

After cadmium oleate ($Cd(OA)_2$) is injected into the growth solution, the first absorption feature shifts slightly (figure 1.11). In reaction of the sulfur precursor (elemental sulfur) further shifts the first absorption feature. By repeating this process, 5 monolayers of CdS is formed on the CdSe core, and this shell formation shifts the first absorption features up to 45 nm in wavelength. Higher temperature at 240 °C leads to thicker CdS shell formation. The resulting quantum efficiency is as high as 40 %.

SILAR method provides improved relative to a single injection of the all shell materials into the growth solution, which typically resluts in poor quality shell formation. Alternate injection of cationic precursor and anionic precursor makes it possible to control the number of shell layers precisely. Besides this precise size controllability, the SILAR method produces nanocrystals with excellent photoluminescence (PL) properties. If there are very few dislocations at the boundary between the core and the shell, and both the core and the shell have few defects, the PL properties of the nanocrystals are excellent. The reason for the dislocation at the boundary is mainly due to strain that comes from different crystal structures or different lattice parameters. In order to avoid dislocations, the shell must be thin. Another common defect is grain boundaries resulting from multiple nucleation sites on the core. The SILAR method produces thin shell structures with precise control and few grain boundaries.

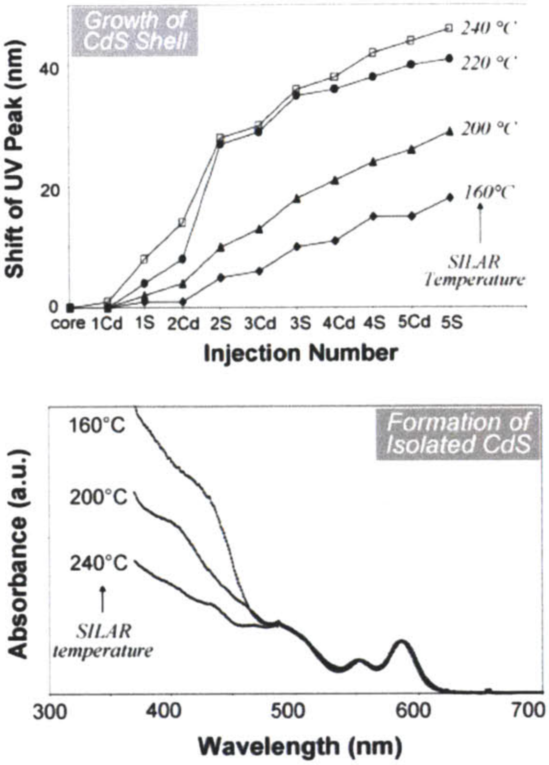

Figure 1.11: Red shift of the first absorption spectrum of CdSe / CdS core-shell nanocrystals, and optimal temperature for the CdS shell formation. Adopted from the reference 37.

Elimination of homogeneous nucleation of shell materials and uniform monolayer growth on the existing core are essential to obtain uniform shell structures. Relatively stable and safe alternative precursors that have weak reactivity to avoid homogeneous nucleation but sufficiently high reactivity to promote the epitaxial growth on the core are required to get uniform shell structure.

The SILAR method is also used for the synthesis of giant CdSe / CdS core-shell nanocrystals.[39] Figure 1.12 is the TEM images of CdSe / CdS nanocrystals with 11 monolayers of CdS shell. This thick shell confines the exciton in the CdSe core effectively with resulting excellent optical properties.

The SILAR method is not always needed for high shell quality. It is reported that thiols, as a sulfur source, can be used for the synthesis of multi-layers of high quality CdS shells.[58] In this case, cadmium monomers and thiols can be injected simultaneously since the threshold temperature for CdS nucleation is lower than when elemental sulfurs are used as the sulfur source. High temperature (300 °C) can be also used for the shell formation. The use of high shell growth temperature offers better quality shell formation. Understanding of these synthesis techniques in batch systems provides a good starting point for the development of continuous core-shell nanocrystal synthesis.

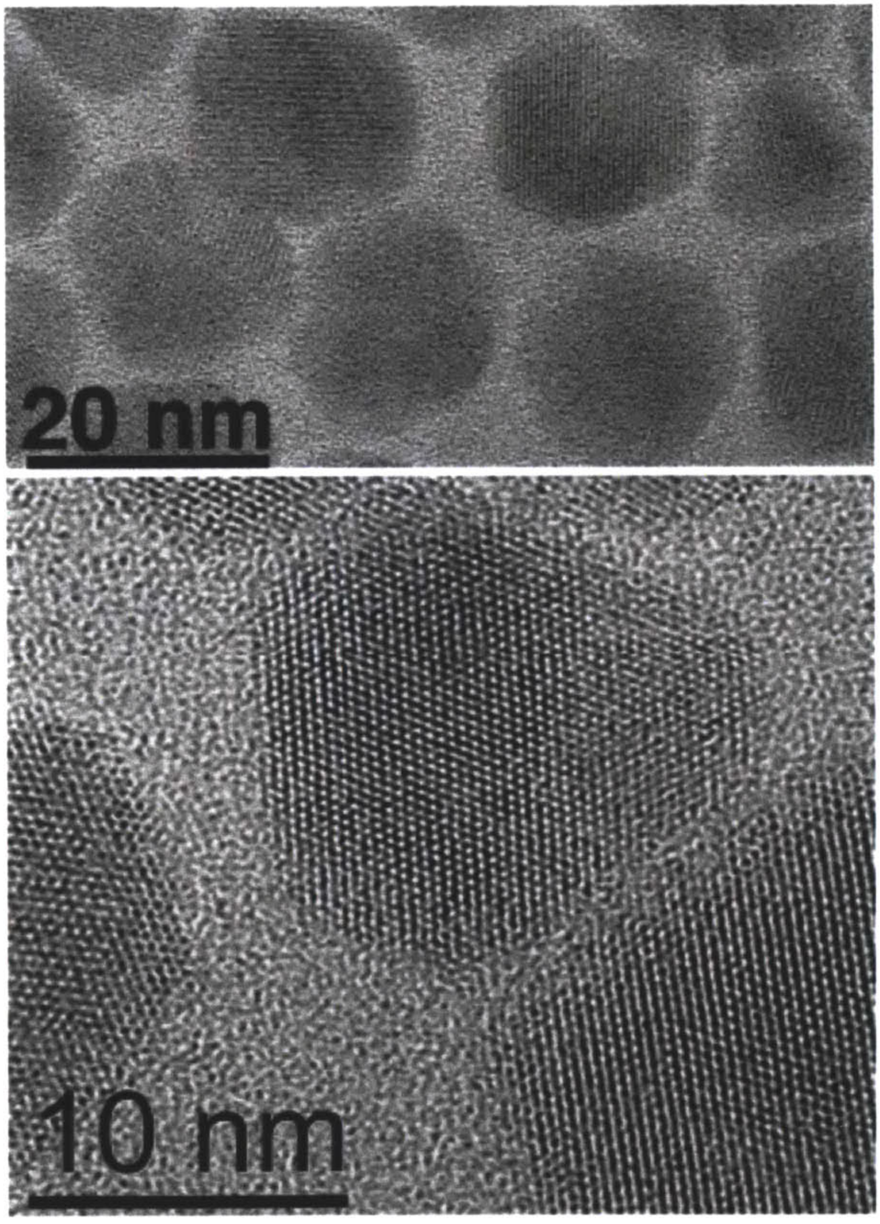

Figure 1.12: TEM images of CdSe / 11 CdS core-shell nanocrystals. High quality thick CdS shell suppressed the blinking behavior of the quantum dots. Adopted from the reference 39.

1.3.5. Line Broadening

Optical properties such as absorbance and photoluminescence are important to determine the quality of quantum dots. Obtaining uniform size distribution of quantum dots has always been challenging in order to obtain narrow emission. However, it is difficult to obtain very narrow emission even with perfectly monodisperse particles due to homogeneous broadening.[59] This homogeneous broadening is attributed to coupling to lattice vibration and ligands on the surface of the quantum dots. Exciton trapping on the particle surface defect site also causes the homogeneous line broadening. However, the detailed understanding still remains questioning.

Typically, an ensemble line width of quantum dots is broader than a single dot emission due to particle size distribution. Particles with different sizes have different energy levels. Therefore, once quantum dots have broad size distribution, the emission of the ensemble becomes broader. This is called inhomogeneous broadening.

In our work, we provided many absorption and emission spectra. Most of our results showed sharper first absorption features and narrower photoluminescence spectra than reported literatures. We speculate those narrower and sharper features were mostly because we obtained better size distribution of quantum dots, rather than reducing homogeneous line broadening.

1.4. Specific aims

- ***Design and the characterization of microfluidic reactors for the synthesis of nanomaterials and complex engineered nanostructures, in conjunction with understanding and controlling the kinetics of the growth process of semiconductor colloidal nanostructures.***

  This thesis will describe the development of a multi-stage microfluidic system operating at high-pressure and high-temperature for the synthesis of structured nanocrystals. By utilizing the advantages of a microfluidic system we can obtain a product with high quantum efficiency and narrow size distribution. In particular, additional side channel injections with precise control of temperature will provide a means to develop a continuous shell formation similar to the Successive Ion Layer Adsorption and Reaction (SILAR) method for the synthesis of heterostructure systems.

- ***Development of continuous cost efficient micro scale processes for the synthesis of QDs, including materials difficult to obtain or not yet synthesized with a batch process (QDs of III-V semiconductors including InP, InAs, or InP_xAs_{1-x} alloy compound).***

  Current methods for synthesizing NPs require the use of potentially harmful, expensive, and often limited numbers of available compounds. Therefore, one of the goals of this thesis work is to develop new processes for high quality QDs synthesis which allows for the use of expanded numbers of reagents and chemistries, taking advantage of microsystems working at high pressure and high temperature. In order to work on difficult synthesis, the development of a proper in-line monitoring device is also very important. For the characterization of semiconductor nanocrystals, in-line UV-Vis would be a good device. Understanding growth mechanisms of III-V materials as well as finding important parameters for the growth is necessary to obtain high quality nanocrystals.

- ***Improvement for nanostructures synthesis.***

  This will include the use of the pre-developed multi-stage microfluidic systems to synthesize nanocrystals, including InP, InAs, InP_xAs_{1-x}, and core-shell structured nanocrystals. By developing microreactors with large volumes (> 400 μl) and utilizing a temperature gradient, we can improve production rate of these nano-materials.

1.5. Thesis overview

This thesis presents the design of different types of microreactors for nanocrystal synthesis as well as the development of a multi-stage high-pressure and high-temperature microfluidic system. Chapter 2 describes the reactor designs and multi-stage high-pressure system construction. This chapter also includes the detailed procedure of microfabrication. Chapter 3 shows investigation of indium phosphide (InP) synthesis. Chapter 4 describes indium phosphide / zinc sulfide (InP / ZnS) core-shell particle syntheses. This chapter also includes other core-shell materials such as indium phosphide / cadmium sulfide (InP / CdS) and indium arsenide / indium phosphide (InAs / InP) core-shell nanocrystals. Chapter 5 describes growth study of indium arsenide (InAs) nanocrystals for NIR applications. This chapter also includes the investigation of InAs growth from two different phosphorus monomer precursors: tris(trimethylsilyl)arsine (TMS_3As) and tris(trimethylgermyl)arsine (TMG_3As). Chapter 6 describes the synthesis of InP_xAs_{1-x} alloy nanocrystals. Chapter 7 compares InAs nanocrystal growths from two different arsenic sources: tristrimethylsilyl arsine (TMS_3As) and tristrimethylgermyl arsine (TMG_3As). Chapter 8 is the summary of the thesis and future opportunity.

Chapter 2

Multi-Stage High-Pressure and High-Temperature Microfluidic System

2.1. Introduction

Microfludics have been used to synthesize nanocrystals with great control of size and size distribution.[5, 9-10, 12] These nanocrystals, especially semiconductor nanocrystals,[60] are used for such applications as displays, bio-chem sensing, photovoltaics, and bio-imaging.[28] In order to improve the performance of these devices, it is important to develop production method with excellent controllability and reproducibility is important.

Typically, nanocrystals have been synthesized in batch systems. However, batch system shows limited reproducibility due to the difficulty in control of material concentrations, compositions, and temperatures. Therefore, the quality of the product varies batch to batch, and the scale-up of the batch process has been also greatly challenging. Besides these difficulties, developing an optimization method for fast screening of reaction parameters in batch has also been a difficult task.

Continuous synthesis with microfluidics provides controllability of reaction parameters, and reproducibility, as well as fast heat and mass transfer, in-situ reaction monitoring, and fast screening of reaction parameters. Improved heat and mass transfer allows for homogeneous reaction conditions that are critical for chemical synthesis, and enables use of highly reactive compounds for nanocrystal synthesis. In-situ monitoring system with in-line UV-Vis or photoluminescence enables fast screening of reaction parameters.

The use of high-pressure and temperature expands reaction space in the choice of solvents, ligands or precursors, and also allows for use of conditions that are not accessible in batch system. In particular, the use of supercritical phase allows for improved mixing and tunable solvent densities as described in Chapter 1. Synthesis of structured nanocrystals such as core-shell structures is generally not possible in a single microfluidic device, and therefore requires the development of a multi-stage microfluidic system.

Such a multi-stage microfluidic system allows for stage-by-stage control of reaction conditions. Microreactors are connected in series, and each stage has independent reaction conditions (e.g., a temperature and a residence time). By utilizing different types of microreactors at the each step, the multi-stage system enables the synthesis of structured nanocrystals such as core-shell or nano-rods with hetero-junctions. However, the development of a multi-stage system is challenging, and only limited numbers of examples have been reported. It is especially very difficult to introduce high-pressure and high-temperature condition to the multi-stage systems. Furthermore, structured nanocrystal synthesis without incorporating any manual between steps has also been difficult.

In this chapter, we introduce some of the critical components in developing a high-pressure and high-temperature multi-stage microfluidic system for structured nanocrystal synthesis.

2.2. In-line optical measurement device

2.2.1. Design and Setup

In the synthesis of semiconductor nanocrystals, it is useful to measure optical information such as absorbance or photoluminescence spectra in order to characterize the properties of the nanocrystals such as size, size distributions as well as material structure changes. Incorporating an in-line optical device with the high-pressure flow system provides real-time information of the resulting particles at different controlled conditions, and as a result, enables the systematic study of nanocrystal growth. Although it is obvious that in-situ UV-Vis or photoluminescence measurement allows for fast screening of reaction parameters during the synthesis, it has been challenging to design such an optical measurement device operating at high-pressure with a small dead volume. The device also needs to have an enough signal to noise intensity. Currently, Ocean Optics Company sells in-line absorption or photoluminescence measurement devices, but the maximum operating pressure is less than 55 bar, which is not sufficient for the high-pressure applications considered in this thesis.

A particular challenge in operation of a high-pressure systems is that one does not know the quality or type of the resulting products before the system pressure is reduced to ambient pressure. This is especially the case for difficult syntheses of materials such as III-V quantum dots. Even though high-pressure microfluidic systems provide advantages, the each of a proper in-line characterization tool has always been the bottleneck preventing fast screening. Therefore, except for some II-VI semiconductor synthesis such as CdSe, whose chemistry is very simple and well developed, the synthesis of other materials has been a very time consuming process. In particular, there is no report of the successful synthesis of the III-V semiconductor materials at high pressure. Thus, considering that synthesis of structured nanocrystals is even more challenging, it would be very difficult to synthesize structured III-V nanocrystals without suitable in-line optical measurement device.

Figure 2.1 shows a three-dimensional (3D) schematic of the in-line optical cell. Two stainless steel (type 316) compression parts are compressing a quartz capillary with a length of 2 cm and an inner diameter of 500 μm, and each compression part is connected to the 1/16" tubes. The capillary is sealed with multi-purpose aluminum block with holes with a diameter of 500 μm. Two optical cables are connected to those holes. One cable is connected to the white light source (deuterium and halogen lamps), and the other is connected to a detector. UV light enters perpendicularly to the optical cable connected to the detector.

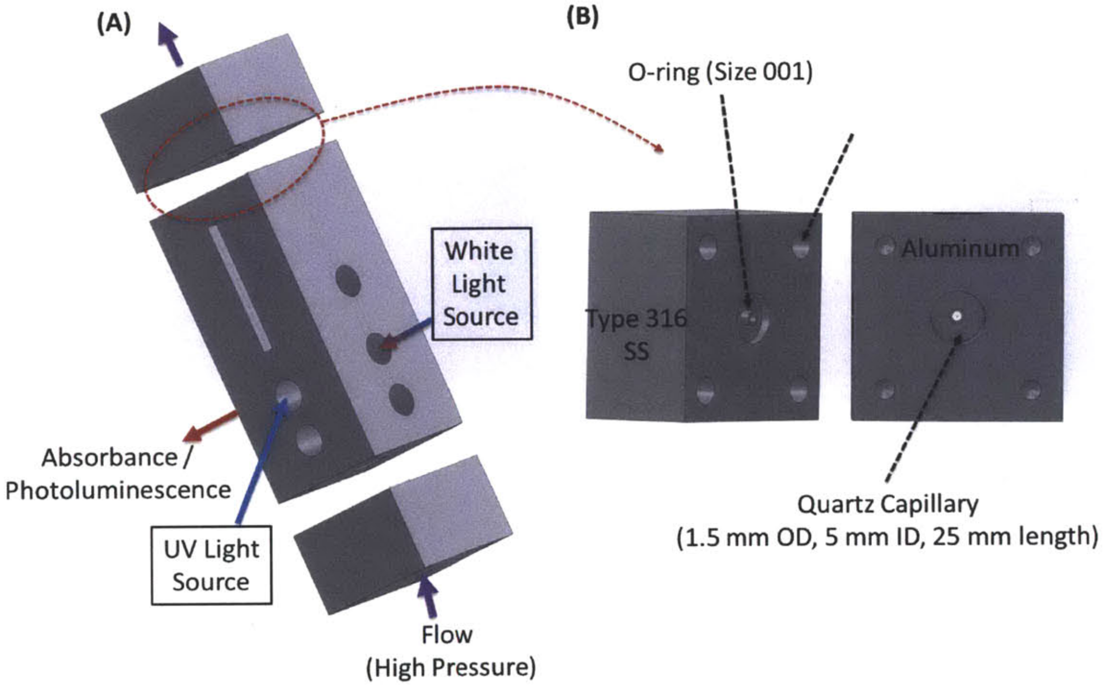

Figure 2.1: In-line optical device for the absorbance and photoluminescence measurements. This can withstand up to 100 bar (Normal operation pressure was between 65 - 80 bar.). A quartz capillary with 0.5 mm inner diameter was compressed by two stainless steel (type 316) caps. Karlez O-ring (size 001, from Mcmaster) was used at the interface between the quartz tube and the cap.

Figure 2.2 shows a photograph of the optical device operating at high-pressure, and figure 2.3 illustrates of the connections of the optical device with accompanying equipment. Proper filters are required to use in order to obtain better signal to noise ratio. A sky-blue filter (Hoya) was typically used for absorption measurements in between 350 nm – 800 nm wavelengths. A strong light emitting diodes (LED) UV source (1W, eBay) was used for photoluminescence measurements. Figure 2.4 shows an image of a multi-stage microfluidic system combined with this optical device.

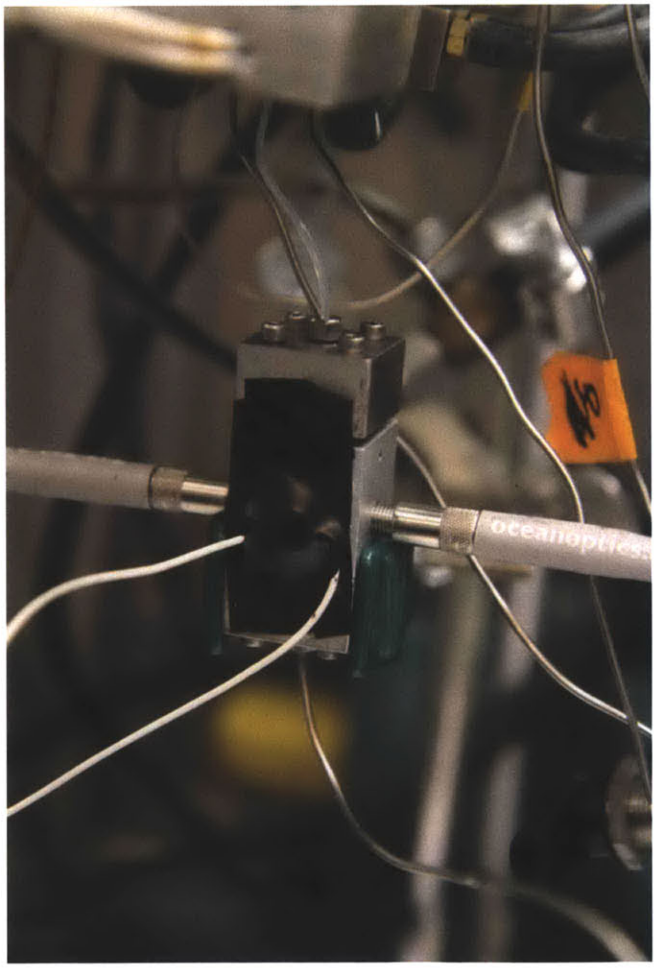

Figure 2.2: Real picture of the optical cell.

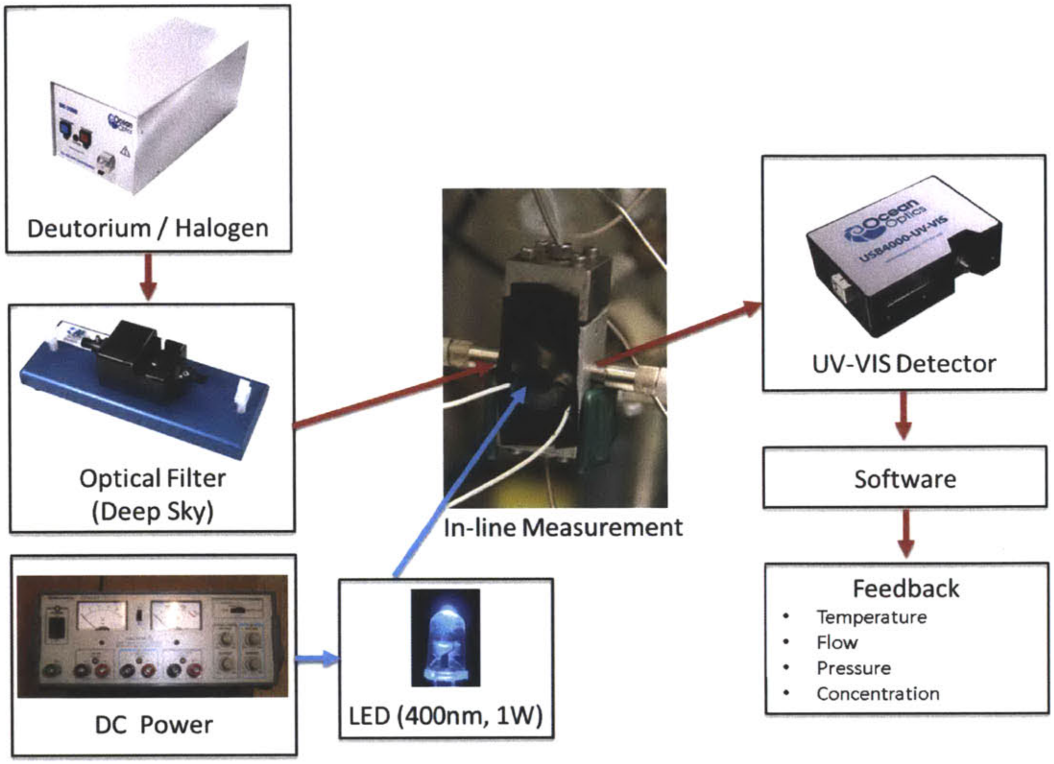

Figure 2.3: Full setup of the in-line optical cell. Deep-Sky camera filter was used to even the intensity of the light source from UV to VIS (300 nm to 800 nm). 1W UV-LED was used to measure photoluminescence from the semiconductor nanocrystals.

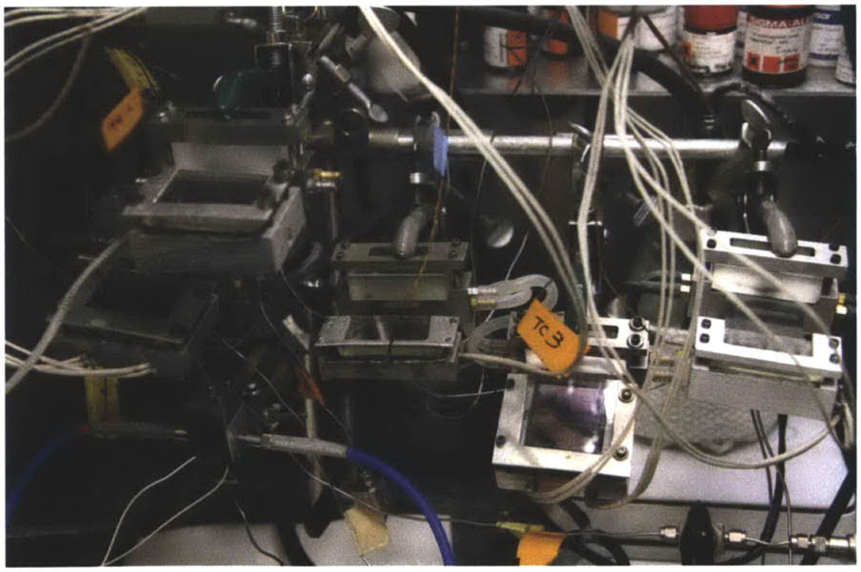

Figure 2.4: Five-stage microfluidic system combined with in-line optical measurement device.

2.2.2. Accuracy of the in-line measurement device

In order to test the accuracy of the in-line measurement device, we synthesized indium phosphide (InP) nanocrystals, and measured the absorption spectrum with the both in-line device and a Hewlett Packard 8452 diode-array spectrometer (bulk measurement). For the bulk measurement, 2.5 mL quartz cuvette (Ocean Optics) was used as a sample holder. The scanning time of the each in-line measurement was 25 ms, and the data were averaged for 20 measurements. We also measured the same InP samples with the Hewlett Packard diode-array.

Comparison of spectra measured with the two device shows that the two peaks were located at the same position (figure 2.5). However, the signal intensities at the first absorption feature were slightly different, which could be due to either measurement method differences (device difference), or oxidation of InP particles in bulk by exposure to air. Considering that the most important information is the location of the first absorption feature, this in-line device provides the same information as other spectrometers that measure samples in bulk scale. All the data reprinted in the thesis as final results from quantum dot synthesis were by the Hewlett Packard 8452 spectrometer measurement. The in-line device was only used to decide whether to collect samples during system operation.

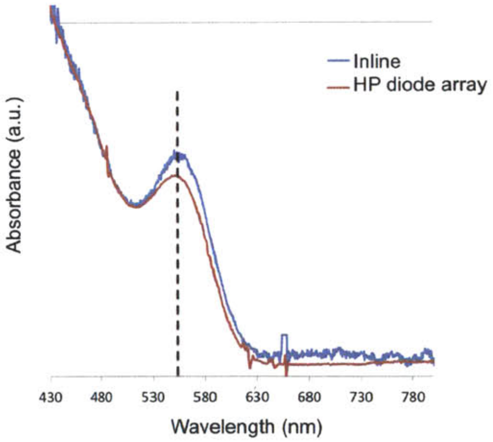

Figure 2.5: Comparison of absorbance measured by the manual in-line device and Hewlett Packard 8452 spectrometer. We can see the peak locations from a same sample with different devices are identical.

2.2.3. Noise Reduction

The signal-to-noise ratio in the in-line data was improved by reducing random high frequency noise. Two methods were conducted, Fourier transform, and smoothing by averages. We can easily convert the absorption signals to frequency space, and eliminate high frequency terms. Or we also can reduce the nose by smoothing method by averaging adjacent data points since the spectrometer for in-line measurement device has many more data points (every 0.47 nm in wavelength) than the Hewlett Packard 8452 spectrometer (every 1 nm in wavelength).

Figure 2.6 shows the noise reduction by different noise reduction methods. Smoothing method provides better features compared to Fourier transform method. In reality, we did not use this method in data reports since it could eliminate other important information in measurements. However, smoothing could be a useful tool while processing data for automatic data analysis such as automated optimization.

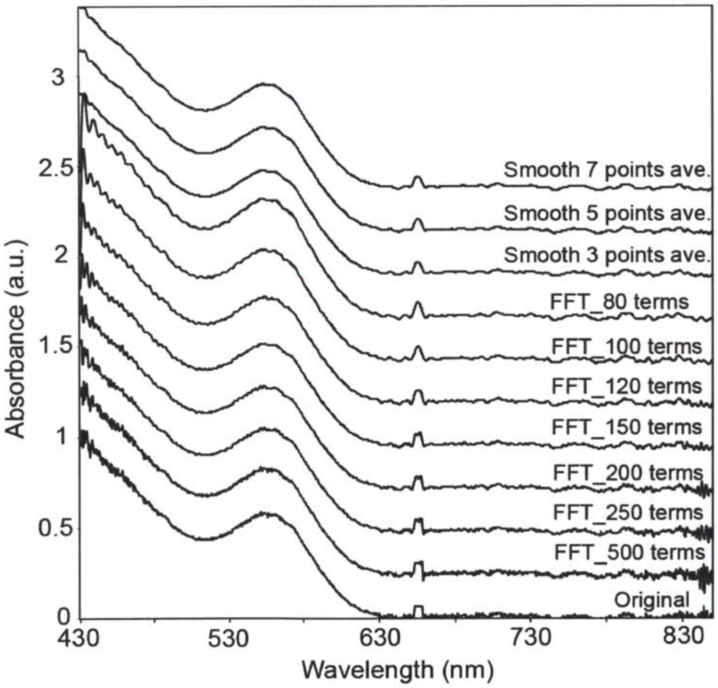

Figure 2.6: Comparison of different noise reduction methods.

2.3. Microreactor Design

2.3.1. Consideration in designing a microreactor

Designing of the microreactor requires consideration of several factors, including reactor volume, channel surface, mixing temperature, and channel dimensions. In order to design a microreactor with side channels,[9] we also need to consider flow distributions that are function of temperature and flowrates. In designing and operation of microfluidic system, the number of injection ports on a microreactor and the number of available syringe pumps are limited. Therefore, we need to design a microreactor with a desired performance under those restrictions. In this section, we will describe the microreactor design procedure, and show examples of microreactors.

2.3.2. Consideration on mixing temperatures

The mixing temperature is very important in nanocrystal synthesis. For example, the nucleation rate is highly dependent on the mixing temperature. Sometimes, we need to inject additional materials at two different temperature regimes, one at hot temperature and the other at cold temperature.

Figure 2.7 is a description of four different mixing strategies in terms of mixing temperatures. Two precursors can be mixed at a cold temperature and delivered to hot regimes (cold mixing). This mixing type is the simplest type and commonly used for organic synthesis. Hot mixing is when two precursors are pre-heated at the desired reaction temperature, and mixing at the reaction temperature. This type of mixing is commonly used for nanocrystal synthesis, since mixing temperature is important to determine the number of nuclei. A moderate temperature mixing reactor is used when hot mixing is desired, but thermal stability of the precursor is poor. Precursors are pre-heated just before their decomposition temperature, and mixed. Then the mixture enters the hot reaction temperature in a short time. Gradient temperature can be used when the mixing temperature is not important. This special temperature strategy allows for fast production of nanocrystals without causing any side effects such as clogging or deposition inside a channel.

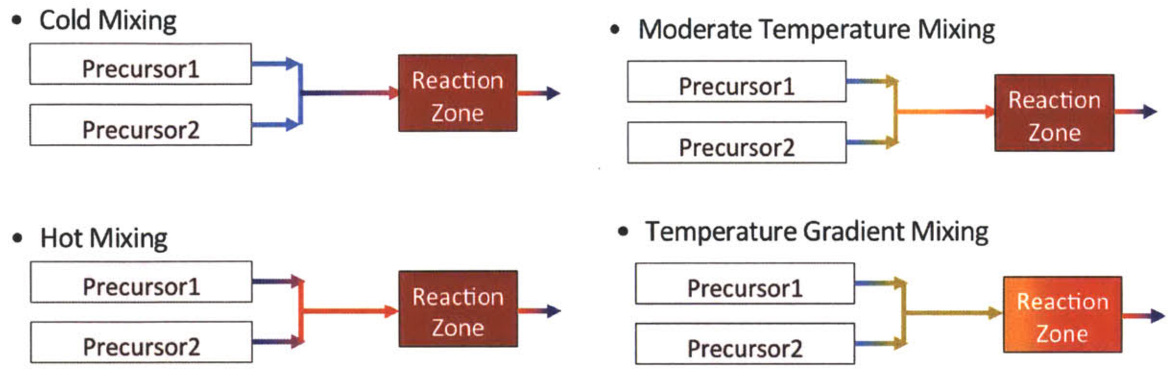

Figure 2.7: four different types of mixing temperatures: cold mixing, moderate temperature mixing, hot mixing, and gradient temperature mixing.

Figure 2.8 is a cartoon of two different microreactors with different mixing schemes. In figure 2.8-(a) all the three precursors are mixing at an elevated temperature, and continuously flow to the reaction zone maintained with gradient temperature. The mixtures are gradually heated to the hot temperature. Figure 2.8-(b) is a microreactor with a cold mixing and a hot mixing. Two materials are mixed at a cold temperature and flow to the hot reaction zone. Another material bypasses the hot reaction zone and is pre-heated prior to being mixed.

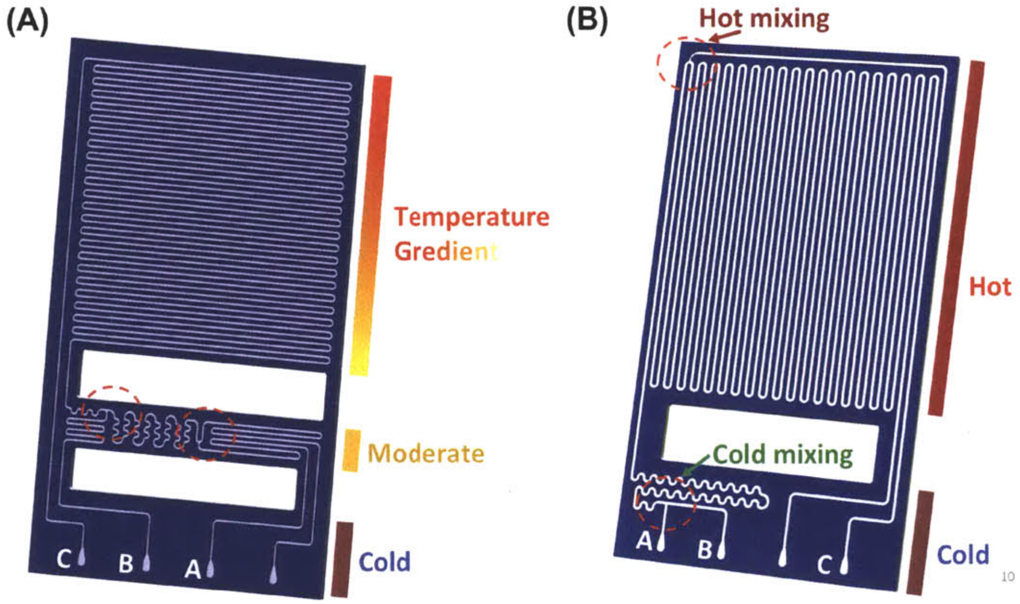

Figure 2.8: Two different microreactors with different mixings. (A) Three precursors are mixing at a moderate temperature and delivered to the reaction regime. Gradient temperature was applied on the reaction zone. (B) Two precursors are mixing at a cold temperature and flowed to the hot temperature reaction zone. Another material is mixing with the mixture at a hot temperature.

2.3.3. Pressure drop / flow distribution calculation

In nanocrystal synthesis, sometimes it is necessary to inject additional materials to grow nanocrystals larger or to build a nanostructure such as core-shell nanocrystals. Although single channel microreactors have been widely used for chemical synthesis they are unable to maintain a low concentration of materials along the reaction channel, which can be very important to suppress undesired nucleation. Therefore, microreactors with side channels were designed to achieve gradual addition.

As a first step, we need to consider the flow distribution, and residence times after each side injection. The fluid distribution depends on temperatures as well as dimensions of channels, since density and viscosity of a fluid is function of a temperature. We also need to consider operational restrictions such as the number of available syringe pumps or location of injection ports on a reactor.

In figure 2.9-(a), we divided each side stream (additional flow to the main stream) into a number of sub-side streams. In order to maintain desired sub-side channel flow distributions, each sub-side channel has different channel dimensions. Typically sub-side channels has much higher flow resistance to prevent any potential back flow from main channel to the origin of the sub-side channel. Figure 2.9-(b) is different microreactors with side streams. Figure 2.9-(c) is the schematic image of the flows in a microreactor with 10 sub-side channels. All the mixing points are located at a cold temperature regime since most of the injected materials to be injected is thermally unstable. The main channel length was elongated after each injection to make the residence times even after each injection.

We determine a desired flow distribution based on synthesis strategy. For example, we can inject a CdSe core nanoparticle solution at the main channel in figure 2.9-(a), a cadmium oleate solution at side-stream 1, and a tri-n-octylphosphine sulfide solution at side-stream 2 in order to synthesize CdSe / CdS core-shell nanocrystals. We can decide to flow the main stream with a flow rate of 20 μl / min, and each side stream with a flow rate of 12 μl / min. Each of the side stream (12 μl / min) is divided into three sub-side streams with flow rates of 3, 4, and 5 μl / min.

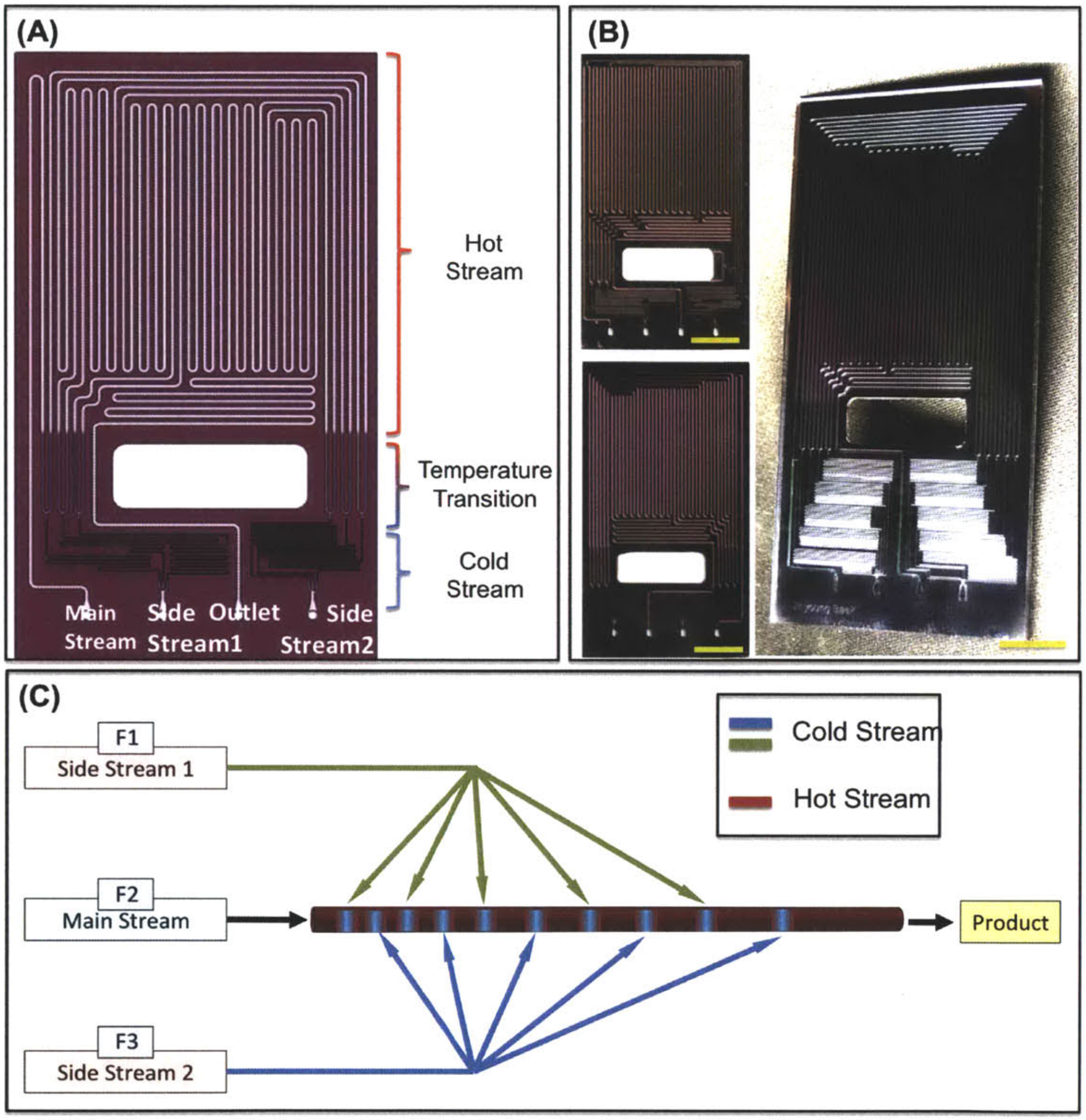

Figure 2.9: (A) Each microreactor is consisting of streams with different temperature, pressure, flowrates. (B) Examples of the microreactors requiring precise flow calculation. (C) Simplified scheme of the flows in a microreactor.

After deciding flowrates, we also can roughly decide and estimate residence times after each sub-side injection by drawing the main channel on the reaction zone of a reactor. Typically, it is desired to maximize reactor volume for the shell formation microreactor in order to have a long overall residence time and to maintain even lower concentration of the additionally injecting materials. However, the limited area of the microreactor sometimes prevents design of an ideal length (residence time) of the each section in the main channel. In such cases, it is important to understand the chemistry in order to select the best flow distributions and the residence time for each section of the main channel.

It is better to locate pressure-drop channels in the cold part of a microreactor. Side-channels described in figure 2.9 require pressure drop channels to control flow distribution. Considering that the most efficient design of a microreactor is maximizing channel volumes in reaction zones, pressure-drop channels need to be located at the cold regime of a reactor to have high flow resist with short channel lengths. This also helps to prevent potential channel clogging in the pressured-drop channel caused by thermal decomposition of injecting materials. The dimension of the pressure-drop channels is much smaller than the main channel, a width of 80 μm and a depth of 100 μm to have at least two orders of magnitude higher flowresist than the main channel with a short length. This small dimension provides high flow resistance with small area on the microreactor, allowing for larger reaction volume.

In order to calculate the pressure drop in a channel, we used a solution of Navier-Stokes equation. Figure 2.10 is a description of a flow in a parallel-plate channel. The wall spacing is 2H and the mean velocity is U. Assuming that z direction is infinitely large. This approach has been introduced in many fluid mechanics textbooks.[61]

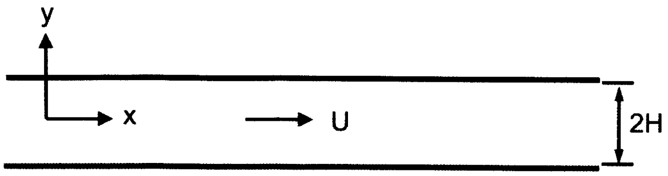

Figure 2.10: Flow in a parallel-plate channel

Navier-Stokes equation is written as Eq. 2.1. μ is the viscosity and ϱ is the density of a fluid.

$$\rho\left(\frac{\partial\vec{v}}{\partial t}+\vec{v}\cdot\nabla\vec{v}\right)=-\nabla\mathbb{P}+\mu\nabla^2\vec{v} \qquad \textbf{Eq. 2.1}$$

Here, $v_x = v_x(y)$ only, and $v_y = v_z = 0$. This indicates that $\mathbb{P} = \mathbb{P}(x,t)$ only. At steady-state with fully developed flow, this equation can be simplified to Eq. 2.2.

$$\frac{d^2v_x}{dy^2}=\frac{1}{\mu}\frac{dp}{dx} \qquad \textbf{Eq. 2.2}$$

By applying a boundary condition that $v_x(\pm H) = 0$, we can calculate volumetric flow rate q (Eq. 2.3).

$$q=-\frac{2H^3}{3\mu}\frac{dp}{dx} \qquad \textbf{Eq. 2.3}$$

However, this calculation is not considering any edge effect of a flow in rectangular duct. As reported, some edge effect can be also considered in rectangular duct flow (figure 2.11).[61]

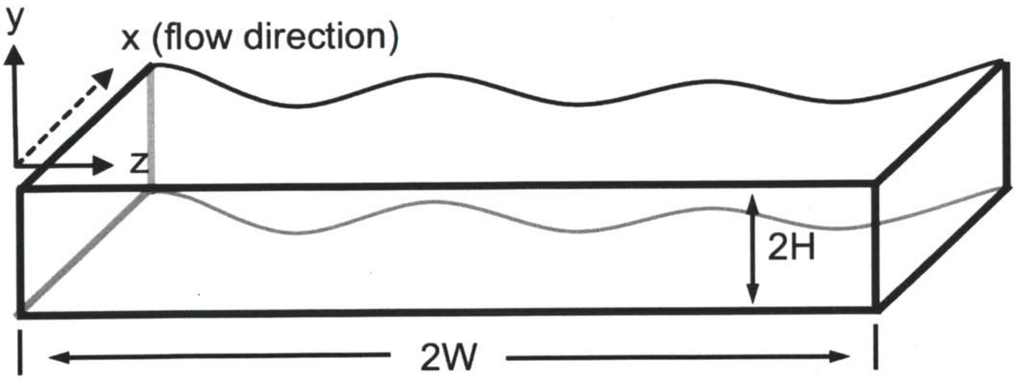

Figure 2.11: Flow in a rectangular channel

Now $v_x = v_x(y,z)$. This system cam be scaled as Eq.2.4.

$$Y \equiv \frac{y}{H}, \quad Z \equiv \frac{z}{H}, \quad \Theta \equiv \frac{v_x}{U} = \frac{3\mu v_x}{H^2(-\frac{dp}{dx})} \qquad \textbf{Eq. 2.4}$$

Here, U is the mean velocity without considering any edge effect. When W >> H, we can assume that edge effect is affected only by a near wall. Therefore, the non-dimensionalized equations and boundary conditions are Eq. 2.5.

$$\frac{\partial^2\Theta}{\partial Y^2} + \frac{\partial^2\Theta}{\partial Z^2} = -3, \qquad \textbf{Eq. 2.5}$$

$$\Theta(\mathrm{Y}, 0) = 0, \quad \frac{\partial\Theta}{\partial Y}(0, Z) = 0, \quad \Theta(Y, \infty) = finite, \quad \Theta(1, Z) = 0$$

By applying the boundary conditions, and solving the Eq. 2.5 by using the finite Fourier transform, we can obtain $\Theta(Y, Z)$ shown in Eq. 2.6.

$$\Theta(Y, Z) = \frac{3}{2}(1 - Y^2) - 6\sum_{n=0}^{\infty} \frac{(-1)^n}{\lambda_n^3} e^{-\lambda_n Z} \cos\lambda_n Y \qquad \textbf{Eq. 2.6}$$

Based on Eq. 2.6, we can neglect edge effect when W ≥ 2H. However, the dimension of typical microreactors is H < W < 2H. Furthermore, we cannot apply the assumption of W >> H in microreactor channel.

Berker (1963) reviewed the exact solution of the Navier-Stokes equation for a flow in a rectangular duct with a finite channel width and depth.[62] The scheme of the duct is same as figure 2.11, but this time the length of the channel width and depth (W and H, respectably) not much different. Eq. 2.7 and Eq. 2.8 show the velocity profile, $u(y, z)$, and the volume flowrate, Q.

$$u(y, z) = \frac{16W^2}{\mu\pi^3}(-\frac{dp}{dx}) \sum_{i=1,3,5,\ldots}^{\infty} (-1)^{(i-1)/2} \left[1 - \frac{\cosh(\frac{i\pi z}{2W})}{\cosh(\frac{i\pi H}{2W})}\right] \times \frac{\cos(\frac{i\pi y}{2W})}{i^3} \qquad \textbf{Eq. 2.7}$$

$$Q = \frac{4HW^3}{3\mu}\left(-\frac{dp}{dx}\right)\left(1 - \frac{192W}{\pi^5 H}\sum_{i=1,3,5,\ldots}^{\infty}\frac{\tanh\frac{i\pi H}{2W}}{i^5}\right) \qquad \textbf{Eq. 2.8}$$

Here, the volume flowrate is a function of pressure drop, $(-\frac{dp}{dx})$. Therefore, we can simplify this equation as Eq. 2.9 using a flow resistance R.

$$\left(-\frac{dp}{dx}\right) = Q(\rho(T)) \times R(W, H, \mu(T)) \qquad \textbf{Eq. 2.9}$$

The volume flowrate is a function of solvent density, and solvent density is changing with temperature change. Channel resist (R) includes viscosity term, and this is also a function of temperature.

Properties of commonly used solvents such as hexane, octane, dodecane, or toluene can be obtainable from NIST thermodynamic database.[63] Figure 2.12 is an example. This shows density and viscosity changes as temperature at 65 bar. By using this database, the desired channel dimensions can be computed with MATLAB.

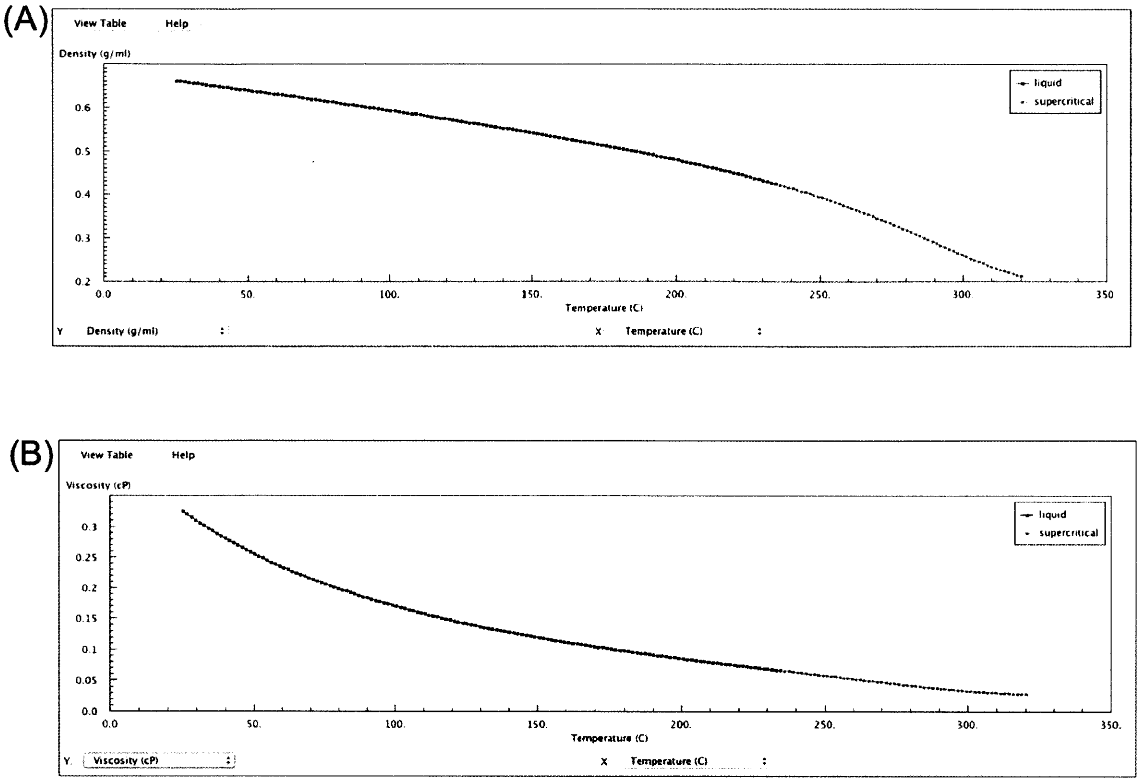

Figure 2.12: (A) density and (B) viscosity of hexane at different temperatures and a pressure of 65 bar.

The main channel also passes in between hot zone and cold zone in a reactor. Since the channel lengths this regime is short compared to the entire main channel length (approximately 1.5% of the total main channel length), we used averaged viscosity value for these sections. The temperature dependent viscosity data in the NIST database was fit to an exponential model, Eq. 2.10.

$$\mu(T) = \mu_0 e^{-bT} \qquad \textbf{Eq. 2.10}$$

With this equation, we averaged the viscosity, and used the value for the flow resist calculation of temperature transition zone.

Figure 2.13 is an example of a mask drawing of a microreactor with 10 sub-side streams based on these calculations. The width of the microreactor is 4.5 cm and the height is 9.5 cm. All the masks of different reactor designs used in the thesis are in Appendix D.

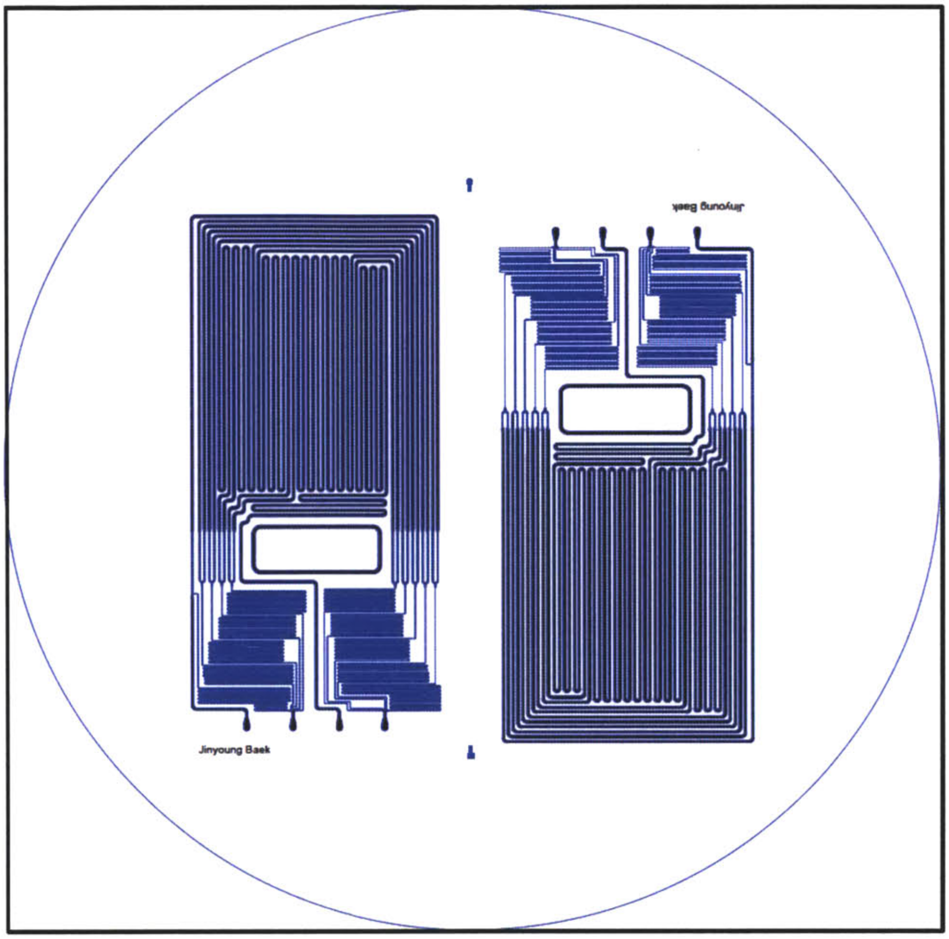

Figure 2.13: Example of a microreactor drawn on a 6” silicon wafer.

2.3.4. Theoretical flow distribution (Sensitivity analysis)

Once the design and fabrication of the microreactor has been completed, the best flowrates and temperatures for an optimal reaction condition can be determined. As explained in Chapter 2, the sub-side channels (pressure drop channel) need to have very high flow resistance compared to the main channel in order to make the desired flow distribution for wide range of operational conditions. Therefore, the pressure drop channel in a microreactor has 400 – 600 times larger flow resistance than the main channel flow resistance. In order to investigate the flow distribution change at different temperature and flow rates, we performed sensitivity analysis (table 2.1).

Table 2.1: Flow distributions at different reaction zone temperatures assuming that the cold part of the reactor is maintained at 80 °C. The main flow is 30 µl / min, and each side stream is 10 µl / min.

		Side Injection 1 (total: 100%)					Side Injection 2 (total: 100%)				
Cold Temp.	Hot Temp.	S1	S2	S3	S4	S5	S6	S7	S8	S9	S10
80	280	18.3%	19.1%	19.9%	20.8%	21.9%	18.3%	19.0%	19.6%	20.9%	22.2%
80	300	18.4%	19.2%	19.9%	20.8%	21.8%	18.4%	19.1%	19.6%	20.8%	22.1%
80	320	18.4%	19.2%	19.9%	20.7%	21.8%	18.5%	19.1%	19.6%	20.8%	22.0%

By calculating the flow distribution changes when the reaction zone temperature changed. This analysis was needed since the reaction temperature was often changed during synthesis. We fixed the main channel flowrate at 30 µl / min and each side flow rate at 10 µl / min. The calculation showed that the flow distribution was not significantly effected by the change of the reaction temperature. A reaction temperature change in 40 °C gave less than 0.5 % difference in flow distribution.

We also investigated the effect of the cooling zone temperature (table 2.2). In real microreactor operation, it is very difficult to control the cooling zone temperature precisely since the temperature is always coupled with the reaction zone temperature. With preliminary test experiments, we found the cooling zone temperature was maintained around 80 °C when the hot reaction zone temperature was 300 °C. Based on this temperature as a reference, we investigated the effect of the cooling zone temperatures. We found that the cooling zone temperature had more impact on changing flow distributions than the hot reaction zone temperature because the flow resistance in the cooling zone was much higher than the reaction zone. Nevertheless, the maximum difference in flow distribution change was less than 2.3 % of the desired distribution, although the cooling zone temperature was changed over 40 °C.

Table 2.2: Flow distributions at different cooling zone temperatures. Reaction zone is maintained at 300 °C. The main flow is 30 μl / min, and each side stream is 10 μl / min.

		Side Injection 1 (total: 100%)					Side Injection 2 (total: 100%)				
Cold Temp.	Hot Temp.	S1	S2	S3	S4	S5	S6	S7	S8	S9	S10
80	300	18.4%	19.2%	19.9%	20.8%	21.8%	18.4%	19.1%	19.6%	20.8%	22.1%
90	300	18.3%	19.1%	19.9%	20.8%	21.9%	18.3%	19.0%	19.6%	20.9%	22.2%
100	300	18.2%	19.1%	19.9%	20.9%	22.1%	18.2%	18.9%	19.6%	20.9%	22.3%
120	300	18.0%	18.9%	19.8%	21.0%	22.3%	18.0%	18.8%	19.6%	21.0%	22.6%

We also investigated the effect of injection amounts on the flow distribution in the microreactor (table 2.3). The cooling temperature was set to 80 °C, and the hot reaction zone temperature was set to 300 °C. We changed the flow rates of the main channel and each side channel. As expected, the flow distributions of the case of 30 / 30 μl / min (main flow rate / each side flow rate) and 15 / 15 μl / min are similar.

Table 2.3: Flow distributions with different injection flowrates. The cooling zone is maintained at 80 °C and the reaction zone is maintained at 300 °C.

		Side Injection 1 (total: 100%)					Side Injection 2 (total: 100%)				
Main flow (μl)	Each side flow (μl)	S1	S2	S3	S4	S5	S6	S7	S8	S9	S10
30	5	16.7%	18.3%	19.9%	21.6%	23.6%	16.7%	18.2%	19.6%	21.7%	23.9%
30	10	18.4%	19.2%	19.9%	20.8%	21.8%	18.4%	19.1%	19.6%	20.8%	22.1%
30	15	18.9%	19.4%	19.9%	20.5%	21.3%	19.0%	19.3%	19.7%	20.5%	21.5%
30	20	19.2%	19.6%	19.9%	20.3%	21.0%	19.2%	19.5%	19.7%	20.4%	21.2%
30	30	19.5%	19.7%	19.9%	20.2%	20.7%	19.5%	19.6%	19.7%	20.3%	20.9%
30	50	19.8%	19.8%	19.9%	20.1%	20.4%	19.8%	19.7%	19.7%	20.1%	20.7%
15	15	19.5%	19.7%	19.9%	20.2%	20.7%	19.5%	19.6%	19.7%	20.3%	20.9%

When a flowrate of each side stream was much less than the main flowrate (the main flow: 30 μl / min and the side flow: 5 μl / min), the flow distribution changed approximately up to 18 %. However, in this case, the absolute amount of additional injection is very small compared to the main channel flow; the 18 % change could not be significant.

2.3.5. Qualitative flow distribution characterization

In order to confirm that each of the injected flow at a side channel was divided into the sub-side channels, We connected microreactor on to a Teflon connector, and flowed a CdSe quantum dot solution in hexane with a flowrate of 30 µl / min at the main channel (Figure 2.14). We also injected two additional side streams (pure hexane), each of which flowrate was 10 µl / min. We were able to observe emission gradient from the quantum dots, indicating that side channel flow is well distributed. However, quantitative analysis of the flow distribution could also be very interesting.

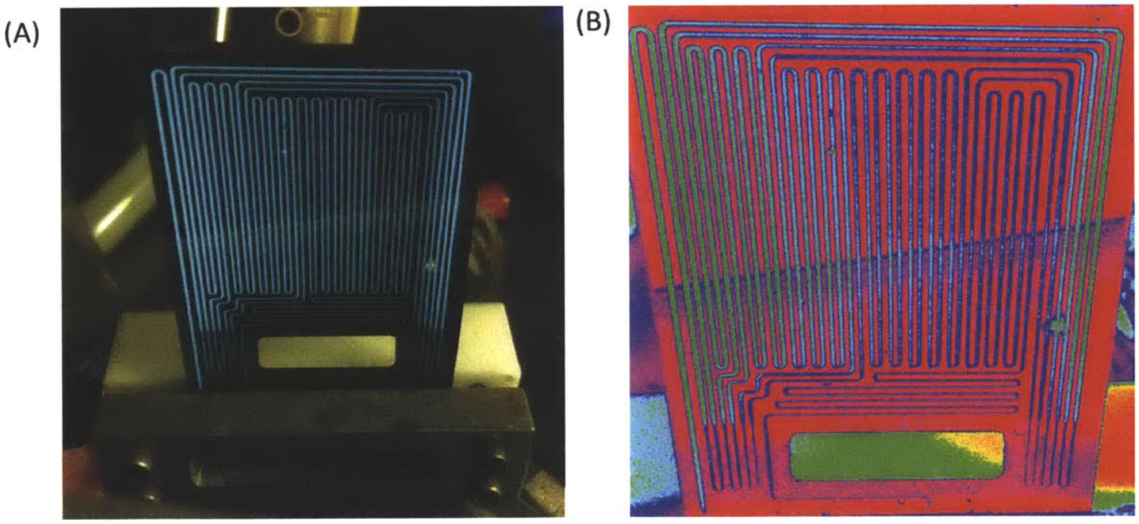

Figure 2.14: Flow distribution inside of a microreactor with two additional side streams. The main stream flowrate was 30 µl / min and the flow rate of the each of the side stream was 10 µl / min. We can observe (A) emission gradient by quantum dot dilution. (B) is processed image for the better understanding of the flows inside of a microreactor. Based on the emission intensity, the color changes from yellow to blue.

2.4. Design of the heating block

The heating block design is an important component in controlling temperature of a microreactor. In order to maintain a constant temperature over all the microreactor areas, the block needs to have a width of 5 cm and a height of 5 cm. However, quantitatively, it is not clear how thick the heating block need to be, as well as where the heating cartridges need to locate. Since a microreactor is usually located in a hood, either natural convection or forced convection, or both of them, is cooling down the heating block. Therefore at a steady state, the heating block is maintained at a controlled temperature by balancing electrical heating (by heating cartridges) with convectional heating loss. A previous study[64] did not include this factor. In order to design a better heating block, we ran COMSOL Multiphysics simulations.

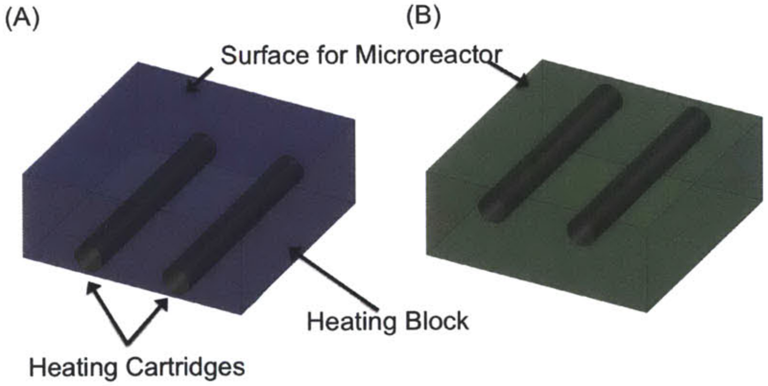

Figure 2.15: Two different heating block designs. A heating block is consisting of aluminum body, and heating cartridge. Heating cartridge could locate (A) far from or (B) close to the surface contacting to microreactor. This block has a dimension of 5 cm x 5 cm x 2 cm (width x height x depth).

Figure 2.15 is a cartoon describing two different types of heating block. Heating cartridge could locate far from (figure 2.15-(a)) or close to (figure 2.15-(b)) the surface contacting to microreactor. In our Multiphysics simulation, we controlled convectional heat transfer rate on the aluminum surface, and observed the temperature profile on the surface contacting to a microreactor at a steady state. The boundary condition of the surface for microreactor was set to adiabatic condition, and all the other surfaces had a constant convectional heat transfer coefficient h (W / m^{2}K). This coefficient was changed from 5 W/m^{2}K to 200 W/m^{2}K, corresponding to a natural convection and an extreme forced convection respectively. We assume that the inserted heating cartridges had a constant heat flux. The dimension of the heating block was set to 5 cm x 5 cm (width x height), and 2.5 cm in thickness.

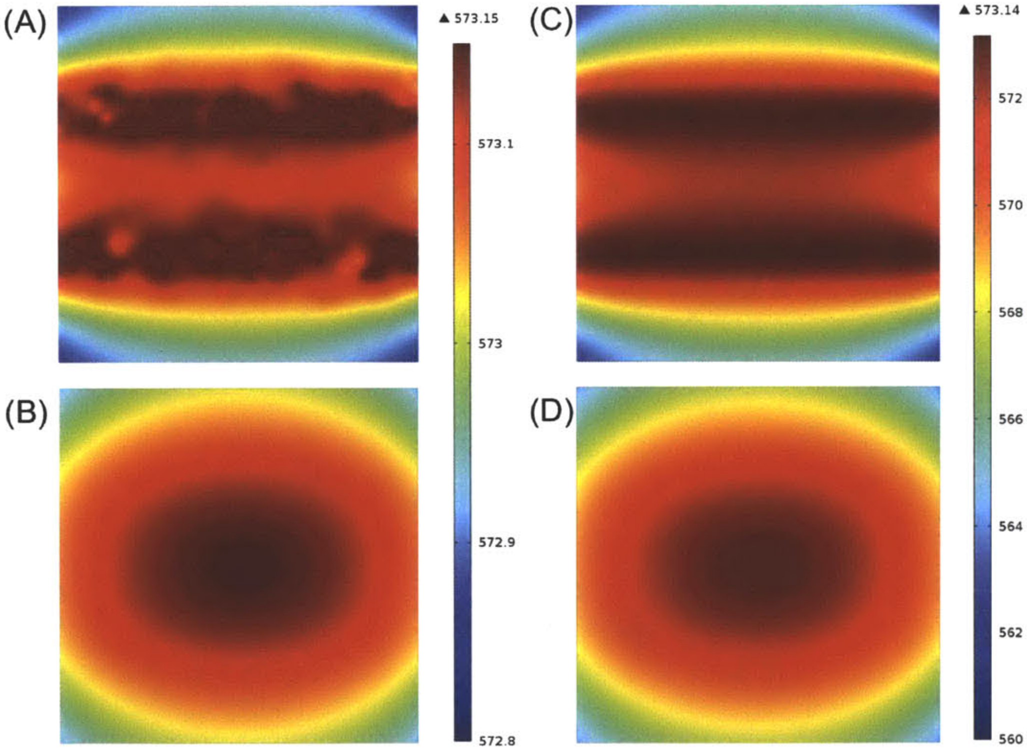

Figure 2.16: Temperature profile on the heating block surface. (A) and (C) are when heating cartridges locate close to the surface. (B) and (D) are when heating cartridges locate far from the surface. (A) and (B) are when the convective heat transfer coefficient is 5 W / m^{2}K. (C) and (D) are when the coefficient is 200 W / m^{2}K.

Figure 2.16 shows the temperature profile of the heating block surface when convective heat transfer is occurring. We tested for two different heating block designs shown in figure 2.15. Figure 2.16-(a) is when the heating block is cooled by natural convection, and the heating cartridges are located near the surface. Figure 2.16-(b) is when the heating block is cooled by forced convection, and the heating cartridges are closed to the surface. Figure 2.16-(c) is when natural convection is cooling the reactor, and the heating cartridges are located far from the surface. Figure 2.16-(d) is forced convection is around the microreactor, and the heating cartridges are located far from the surface.

As the heating cartridge located far from the surface (figure 2.16-(b,d)), the temperature profile on the surface was more uniform regardless the type of the convectional cooling. As expected, when the heating block is affected by forced convectional cooling, the temperature variation on the surface is much larger. Natural convectional cooling only gave less than 0.5 °C difference between center and edge. However, forced convection gave up to approximately 12 °C difference.

In order to further reduce the temperature variation on the surface when the force convection exists around the microreactor, we can put copper plate in between the heating block and a microreactor. Copper is a good material having a good heat conductance. However, copper has very low specific heat (0.39 kJ / kg K) compared to aluminum (0.91 kJ / kg K). Considering that the heating block needs to have reasonable heat capacity to maintain temperature without much fluctuation and machining copper is not easy, we can just put a copper plate in between a microreactor and the heating block. Additionally, a graphite sheet (0.8 mm thick, McMaster Carr.) was used to ensure good thermal contact.

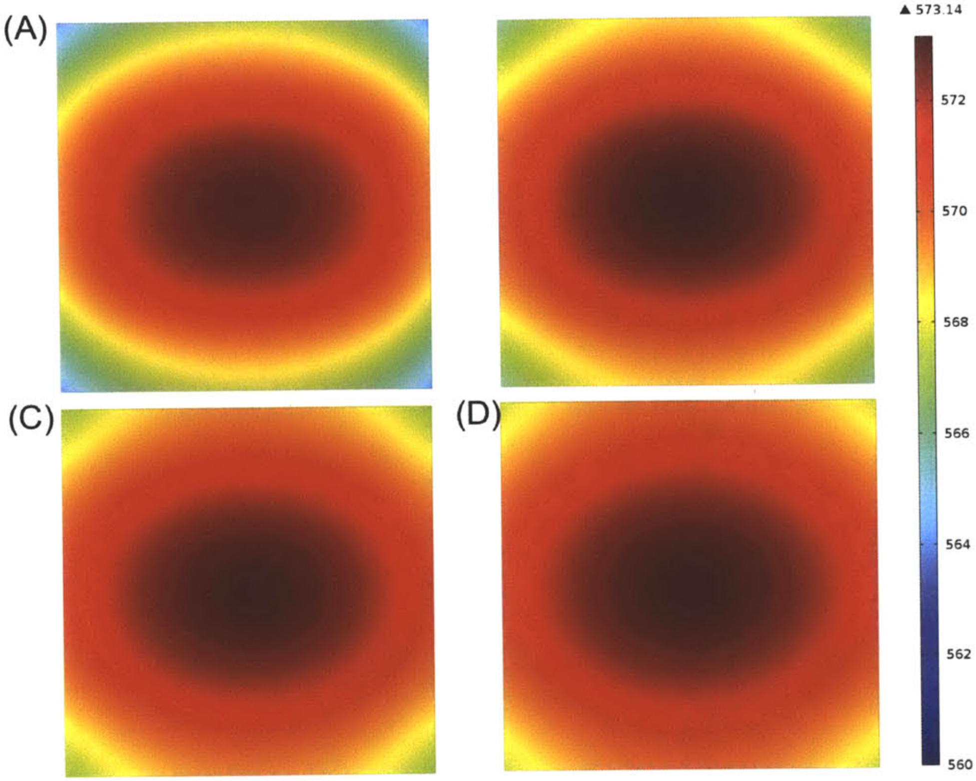

Figure 2.17: Temperature profile on the heating block surface with different copper plate thickness. As the worst case, we assumed that the heating block is affected by forced convection. (A) A cooper plate in between the heating block and microreactor. (B) 1 mm, (C) 2.5 mm, and (D) 4 mm copper plate was inserted.

Figure 2.17 is the temperature profile on the surface when copper plates with different thickness were inserted in between a microreactor and the heating block. We assumed that the heating block is cooled by forced convection, which is the worst case. As we increase the thickness of the copper place, we were able to obtain more uniform temperature profile on the surface.

By running these simple simulations, we were able to machine a better design of a heating block. We located the heating cartridge far from the surface, and inserted 4 mm copper plate in between a microreactor and the heating block. And, during microreactor system operation, in order to reduce forced convectional cooling, we tried to reduce the airflow around a microreactor in a chemical hood by changing the location of the front door of the hood.

2.5. Modification of fabrication process

Since the sequential injection device has long and narrow channels with high aspect ratio, it is very difficult to fabricate the device with the methods previously used.[23] In order to fabricate a device of exquisite workmanship, we decided to use a hard mask rather than soft mask. Based on previous methods, we coated 15 – 20 μm of polymer photoresist on the top of the 500 nm thermally grown oxide layer. However, using a thick photoresist always resulted in large variations in channel widths, and it was very difficult to develop a thick photoresist with small patterns without any defects. Furthermore, it was very difficult to obtain a uniform and thick photoresist coating on a wafer. The error in the channel width was typically more than 10 μm, and sometimes more than 15 μm. This error was not acceptable. With DCVD process (Company: Applied Materials), we were able to put 4 μm thick silicon oxide on the top of the 500 nm silicon oxide layer. Since the maximum available thickness of one oxide layer deposition process is 2 μm, one wafer needs to be processed twice, following a Piranha process (a micture of 3:1 concentrated sulfuric acid to 30% hydrogen peroxide solution, 10 minutes process time) to clean the wafer surface.

After the DCVD process, only less than 1 μm thin photoresist is enough for patterning, followed by 3 seconds of UV exposal and 1 minute development. This is very easy and provides an almost perfect pattern development. However, the wet etching process (BOE, Buffered Oxide Etching to remove silicon oxide) could cause errors in channel width since the etching direction is isotropic. However, the maximum potential error is less than 8 μm, which is less than the error in using thick photoresist. Nevertheless, this error is somewhat controllable. This means, once we design a photomask with 6-8 μm narrower channel dimensions than ideal, we can decrease the error. Ideally, dry etching (isotropic etching) with AME5000 (Model number: P5000) is better than the BOE wet etching process.

Figure 2.18 shows a schematic of the fabrication process, reflecting the process modification explained before. Another minor tip is that we can use a protective tape (commonly called as a blue-tape) on the backside of the silicon wafer while wet etching (BOE) process on the front side. This prevents from stripping of the silicon oxide. Since the thermally grown 0.5 μm of the silicon oxide is a good hard mask, we can use only 3-4 μm thickness of photoresist instead of using a 10 μm thick polymer photoresist. This also allows for better patterning of the backside of the reactor, and makes it easier to fabricate.

In order to control the channel depth, we used a Kapton tape. The desired etching depth of the pressure drop channel was 100 μm, and the depth of the main channel was 430-450 μm. First we etched 100 μm, and put a Kapton tape only on the pressure drop channels. Then, the main channel was etched 330 - 350 μm more. The variation of the channel depth in the pressure drop channels was approximately less than 2.5 %, but that in the main channel was up to 4 %. Typically, the etching rate at the reactor center was slower than the other part owing to the wide channels (main channels) with low aspect ratio. However, the 4 % variation in the main channel would not give a significant effect on the flow distribution, since the theoretical pressure drop at the main channel is much less than the side channels (pressure drop channels). Appendix E contains the detailed procedures shown in figure 2.18.

This modified fabrication procedure enables fabrication of large-size microreactors without any defects, and can be also applied to fabrication of a 6-inch wafer sized reactors with small (< 80 μm) microchannels.

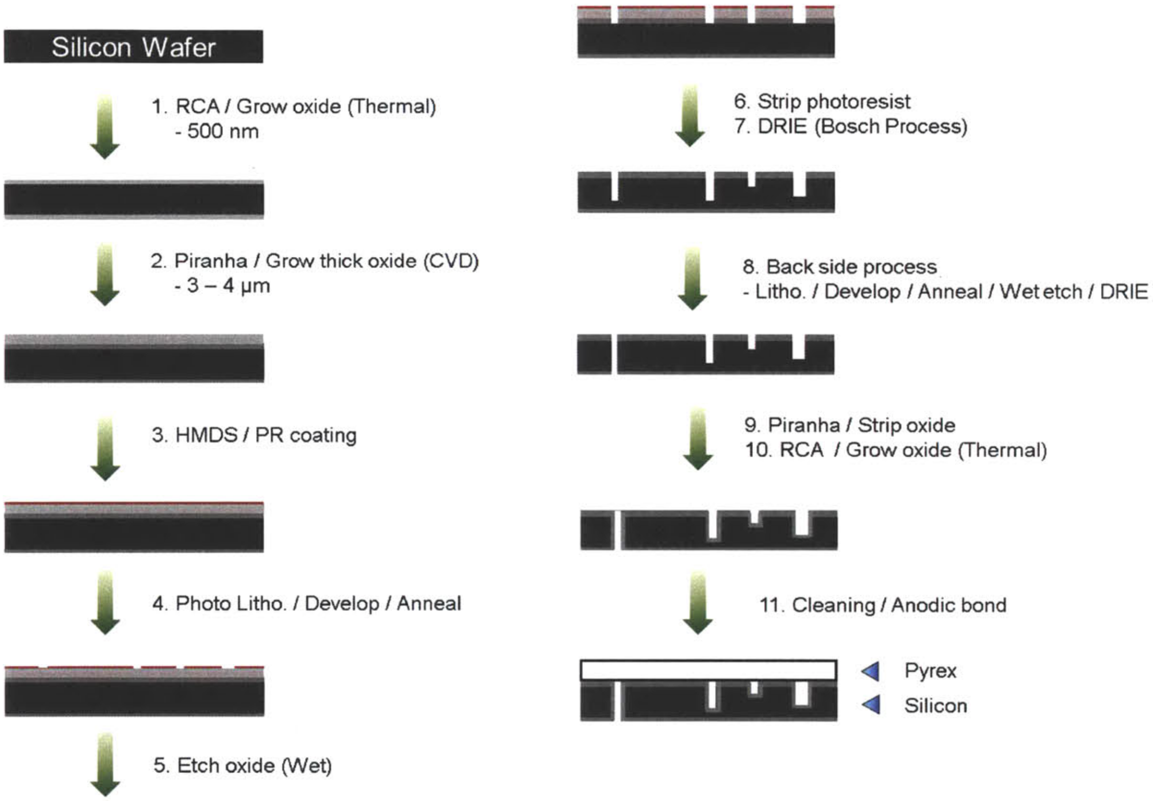

Figure 2.18: Step-by-step description of the fabrication process. 4.5 µm of silicon oxide was used as a hard mask. This allows for precise development of the narrow channel widths of several ten micrometers. This hard mask method also enables fabrication of wide area with fewer defects: larger microreactor with small dimensions.

Chapter 3

Multi-Step Indium Phosphide Synthesis at High-Pressure and High-temperature

3.1. Introduction

InP nanocrystals[17, 65-66] are of significant interest for use in optoelectronic devices, specifically as a replacement for CdSe nanocrystals in commercial applications. However, the current mechanistic understanding and synthetic procedures for InP nanocrystals has not yet reached the same level of sophistication as for CdSe nanocrystal synthesis.[25, 67-73] Although it is reported that the growth mechanism of InP nanocrystals could be different from CdSe nanocrystal growth[65], important parameters for InP nanocrystal growth remain to be studied. Microreactors[4, 7] could be one approach to systematic studies of InP nanocrystal growth, but the limited solubility of indium precursors in organic solvents at room temperature is very challenging.

In this work, we build on previous InP nanocrystal synthetic[17] and mechanistic work[65] in order to probe the experimental parameters involved in InP nanocrystal syntheses using a truly continuous three stage microfluidic reactor to precisely tune reaction conditions in the mixing, aging, and sequential growth regimes. We find that the growth of InP nanocrystals is dominated by the aging regime, which is consistent with a model of InP nanocrystal growth where nanocrystal growth is dominated by non-molecular processes such as coalescence from non-molecular InP species and inter-particle ripening processes.[65] The InP growth model is in contrast to the molecular based growth of nanocrystals as observed in CdSe and PbSe nanocrystals.[25, 67-70] We observe that the size of InP nanocrystals is predominantly dependent on the concentration of free fatty acid in solution and the aging temperature. Other experimental parameters such as injection temperature and particle concentration do not appear to significantly affect InP nanocrystal size or size distributions. In addition, we probe the ability to grow larger InP nanocrystals through the sequential injection of precursors in the third stage of the microfluidic reactor.

3.2. Indium myristate ($In(MA)_3$) preparation

One of the challenges in flow synthesis of the III-V semiconductor nanocrystals is limited metal precursor solubility at room temperature. Most of the well-known metal carboxylate precursors including cadmium oleate or zinc oleate are soluble at elevated temperatures above 100 °C in various organic solvents such as hexadecane or 1-octadecene (1-ODE), which are commonly used for nanoparticle synthesis. However, those metal carboxylates have limited solubility at room temperature. In most batch synthesis, the reaction temperatures are above 100 °C, and therefore the solubility is not a problem. However, in order to flow metal carboxylates at room temperature, it is critical to develop a method to dissolve those precursors without compensating the quality of the resulting nanocrystal. Alternatively, it is also possible to find or synthesize metal precursors soluble in organic solvents; trimethyl indium is an example. However, it was reported that the quality of the resulting nanocrystal was much worse than conventional metal carboxylate precursors.[18]

Metal carboxylate precursors are soluble in most organic solvents at room temperature by aid of amines. Cadmium oleate or zinc oleate is soluble in 1-ODE containing oleylamines or octylamines. 0.3 – 0.5 vol% amines are required to prepare 100 mM cadmium oleate or zinc oleate. However, since the solubility decreases as the number of the carbons of solvents decreases, around 1 – 1.5 vol% of amines are required in order to prepare the same concentration of those metal precursor solutions. However, amines help oxidation of metal carboxylates. This oxidation occurs at lower temperature in the group XIII metal carboxylates than in the group XII metal carboxylates. Therefore, amines need to be avoided to obtain high quality III-V nanocrystal synthesis.

We have developed a method to solubilize indium myristate ($In(MA)_3$) precursor into conventional organic solvents without amines. As one of the group XIII metal precursors, $In(MA)_3$ has limited solubility in non-polar organic solvents. We found 80 mM $In(MA)_3$ solution in octane could be prepared by adding 15 vol% of tri-n-octylphosphine (TOP) into non-polar organic solvents such as octane. This preparation method enabled to flow $In(MA)_3$ solution at room temperature. TOP did not help to oxidize $In(MA)_3$ at a temperature as high as 380 °C, although amines helped to oxidize $In(MA)_3$ at a temperature as low as 180 °C. However, since TOP was known as a coordinating solvent, we investigated effects of tri-n-octylphosphine amount in a solvent on the quality of indium phosphide nanocrystal products.

Figure 3.1 shows the absorption spectra of InP nanocrystals synthesized using two different solvent mixtures: octane with 10 vol % TOP and octane with 40 vol% TOP. We adjusted TOP amount in a solution. 10 vol % TOP is the minimum amount to prepare 100 mM $In(MA)_3$ in octane. We also prepared a solution containing 40 vol% of tri-n-octylphosphine, 3 times more TOP than the minimal amount. With a two-step microfluidic system consisting of mixing and aging reactors, we synthesized InP nanocrystals at an identical condition: mixing at 150 °C, aging at 320 °C. The system pressure was maintained at 900 psi, and the total residence time was 3 minutes. We found the first absorption spectrum of the InP nanocrsytals became sharper as the TOP amount in the solvent was lower. However, the quality of the resulting InP nanocrystals with 10 vol% TOP using microfluidic system was the same as or better than the reported.[17-18, 66, 74] The details of the microfluidic synthesis of the InP nanocrystals will be described in Chapter 3.

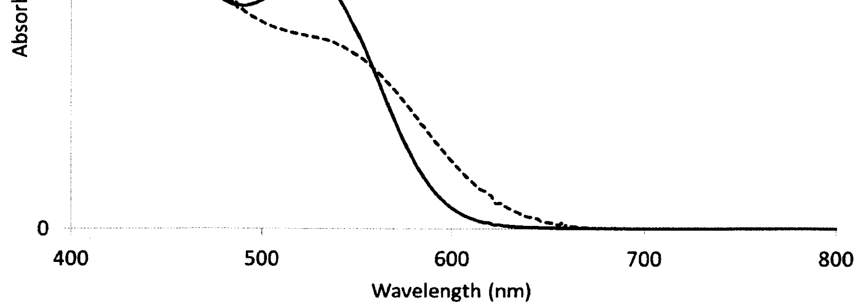

Figure 3.1: Absorbance of the InP nanocrystals synthesized in octane with different tri-n-octylphosphine concentrations.

Since the amount of TOP in $In(MA)_3$ solution affects sharpness of the first absorption spectra, we compared the quality of InP nanocrystals in 10 vol% TOP with those without TOP, both of which are synthesized using microfluidic system. We developed a heating jacket that heats up stainless steel syringes at elevated temperature (Figure 3.2). We heated up $In(MA)_3$ solution in octane to 80 °C in a glove box, and then transferred the solution into a stainless steel syringe. The syringe was immediately taken out from the glove box and covered with this heating jacket maintained at 80 °C. This syringe was mounted on a syringe pump, and connected to a PEEK tube covered with insulator. The solution was initially flowed 600 μl / min for 5 minute to heat up connectors and tubes without causing any precipitation of $In(MA)_3$ due to the limited solubility in organic solvent. With this device, we were able to observe a little sharper absorption spectra compared to when we used 10 vol% TOP in the solvent. However, qualitatively, the sharpness improvement was not significant. Therefore, considering the difficulty in solution preparations and system operations using this heat exchanger, we decided to use 10 vol % tri-n-octylphosphine solution in octane as a solvent for InP synthesis.

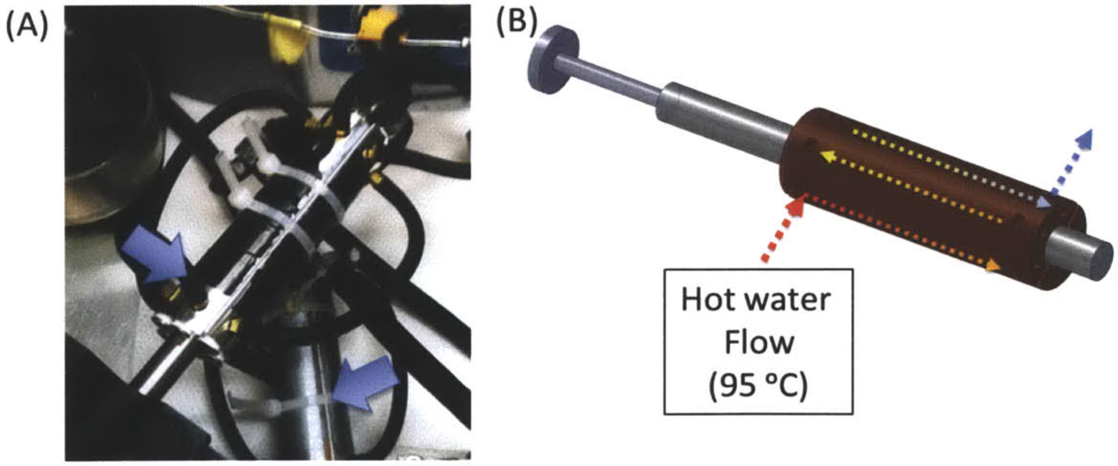

Figure 3.2: Heat exchangers to maintain hot temperature in a stainless steel syringe. (A) A picture of the two heat exchangers covering syringes. (B) A cartoon of the heating water flow. 95 °C water flows inside of the heat changers.

3.3. Methods

3.3.1. Microreactor fabrication

Silicon-based microreactors were prepared as previously reported. Microreactors were designed from flow rate and pressure drop calculations with Matlab R2009a. Three syringe pumps (Harvard apparatus, PHD 22/2000 Hpsi, PHD Ultra Hpsi programmable, and PHD Ultra) were used for solution injections. All connections, tubes, and devices were made of type-316 stainless steel, and heating cartridges were made of multipurpose aluminum.

3.3.2. Preparation of precursor solutions

Octane (Sigma, anhydrous, 99%), Tri-n-octylphosphine (Strem, 97% min.), and all reaction solutions were dried with 4 Å molecular sieves prior to use. $(TMS)_3P$ (Strem) was used without purification. In(MA)3 was prepared as previously reported. The isolated $In(MA)_3$ solid was solubilized in octane solution containing 10 vol% Tri-n-octylphosphine.

3.3.3. Growth via sequential injections

Initially, InP nanocrystals were synthesized from 50 mM $In(MA)_3$ and 25 mM $(TMS)_3P$ with a 30 μl / min flowrate at 320 °C aging temperature. Due to the enhanced mixing in supercritical octane, only brief residence times were necessary between alternating injections of 80 mM of $In(MA)_3$ and 50 mM $(TMS)_3P$ (in total six injections).

The amount of the additional In and P precursors that were added was controlled by tuning the injection flowrates from 5-35 μl / min, corresponding to a ratio of additional $(TMS)_3P$ to initial $(TMS)_3P$ ranging from 0.3-2.0. The total residence time at the sequential injection reactor varied from 1.5 minutes (for 30 μl / min additional $In(MA)_3$ and $(TMS)_3P$ flows), providing a 15 second residence time per injection, and 4 minutes (for 5 μl / min additional flows), providing a 40 second residence time per injection. The temperature at the additional injection points was 80 °C, and for the aging process was 320 °C.

3.3.4. Characterization

Absorbances were obtained by diluted InP nanocrystal solution in octane, prior to measure with Hewlett Packard 8452 diode-array spectrometer. TEM images were taken with JEOL 2010 high-resolution transmission electron microscope, and XRD data were obtained with Rigaku H3R.

3.4. Results

3.4.1. Development of multi-stage microfluidic system

Figure 3.3 illustrates our truly continuous 3-stage silicon-based microfluidic system consisting of mixing, aging, and sequential injection stages operating at a pressure of 65 bar, without incorporating any manual batch manipulation between synthesis steps.[72] We have separated each stage in order to independently probe mixing and aging processes. The first two stages of the reactor were utilized for the systematic study of InP nanocrystal formation (Figure 3.3-a, b). The mixing reactor was maintained at a uniform temperature in order to investigate the effect of different mixing temperatures. Alternatively, the first reaction stage can be heated to create a temperature gradient (Figure 3.4) in order to rapidly obtain highly crystalline InP nanocrystals with relatively narrow size distributions. The second (aging) stage of the reactor was operated at temperatures ranging from 200 - 340 °C in order to study the effect of aging temperature. In the third stage of the system, a sequential injection reactor (Figure 3.3-c) was used to supply more molecular precursors for the further growth of InP nanocrystals. In the case of most InP nanocrystal syntheses, both the aging and sequential growth reactors were maintained at 320 °C in order to utilize supercritical octane (T_c = 296.17 °C and P_c = 2.50 MPa). Octane was selected as the solvent in order to provide excellent mixing, fast diffusivity, and sufficient density for the solubilization of all reagents.

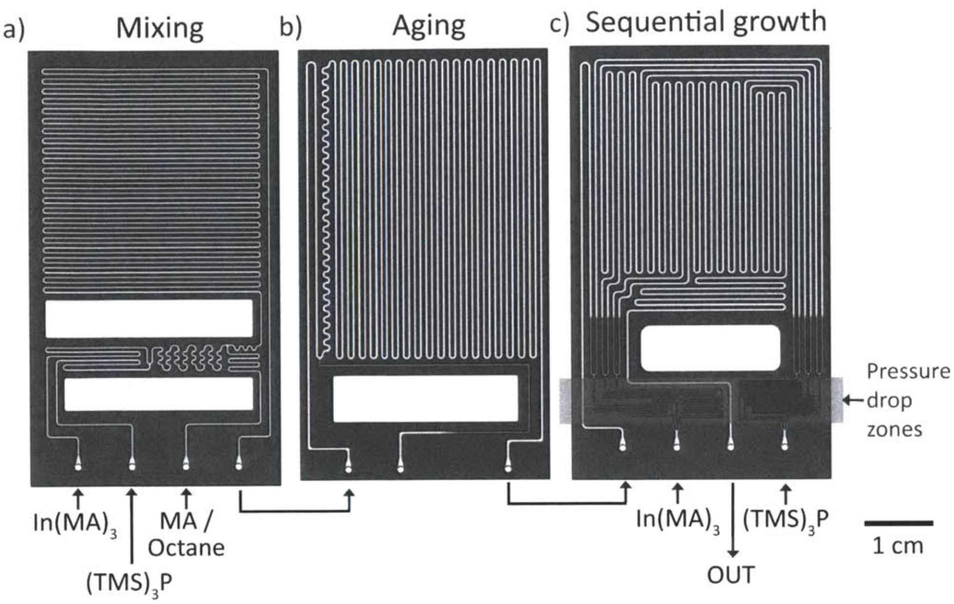

Figure 3.3: Three stage high temperature and high pressure microfludic system with (a) a mixing stage, (b) an aging stage, and (c) a sequential injection microreactor with 6 additional injection channels. The channel widths and depths range from 80-400 μm. The sequential injection microreactor includes pressure drop zones with high flow resistance in order to obtain uniformly distributed injections and to prevent any back flow.

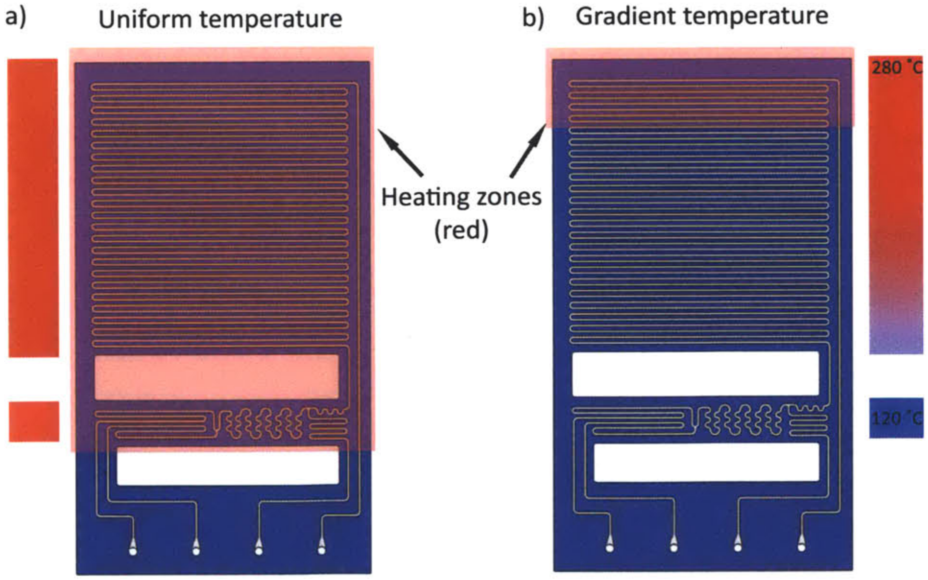

Figure 3.4: Uniform temperature and b) gradient temperature mixing microreactors. Uniform temperature microreactors were used to investigate temperature effect on mixing and aging process, and gradient temperature microreactors were used for all the other experiments. Red zone on each reactor was heated directly by temperature controlled heating block.

3.4.2. Temperature and concentration effects on InP nanocrystal growth

Utilizing a two-stage microfluidic reactor (figure 3.3-a, b), we were able to systematically investigate the effect of different mixing and aging conditions, it should be noted that this separation of reaction conditions is not obtainable in a traditional bench top set-up. Indium myristate ($In(MA)_3$) in octane was mixed with a 2:1 ratio (figure 3.5) with tris(trimethylsilyl) phosphine ($(TMS)_3P$) at various temperatures in the first 'mixing' reactor stage for 2 minutes, followed by aging at different reaction temperatures for 1.5 minutes in the second 'aging' reactor stage. We were not able to observe a significant change in InP nanocrystal size or size distributions using a range of different mixing temperatures, with a constant aging temperature of 320 °C (figure 3.6-a). However, we observed an increasingly prominent first absorption feature at higher aging temperatures (figure 3.6-b).

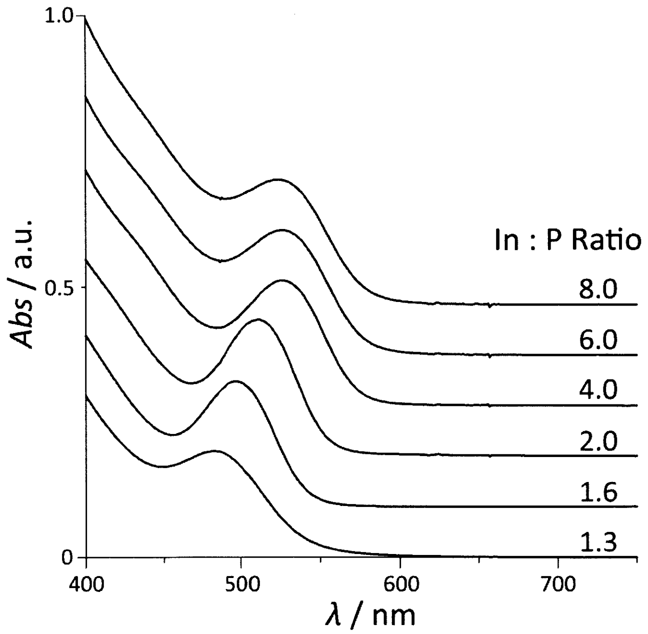

Figure 3.5: Absorption spectra of InP nanocrystals for different $In(MA)_3$ to $(TMS)_3P$ ratios. We also investigated effect of amount ratio between $In(MA)_3$ and $(TMS)_3P$. As the ratio increased, the particle size was larger. The ratio 2 showed the best size distribution. We have kept the ratio to 2, since this ratio showed the best size distribution.

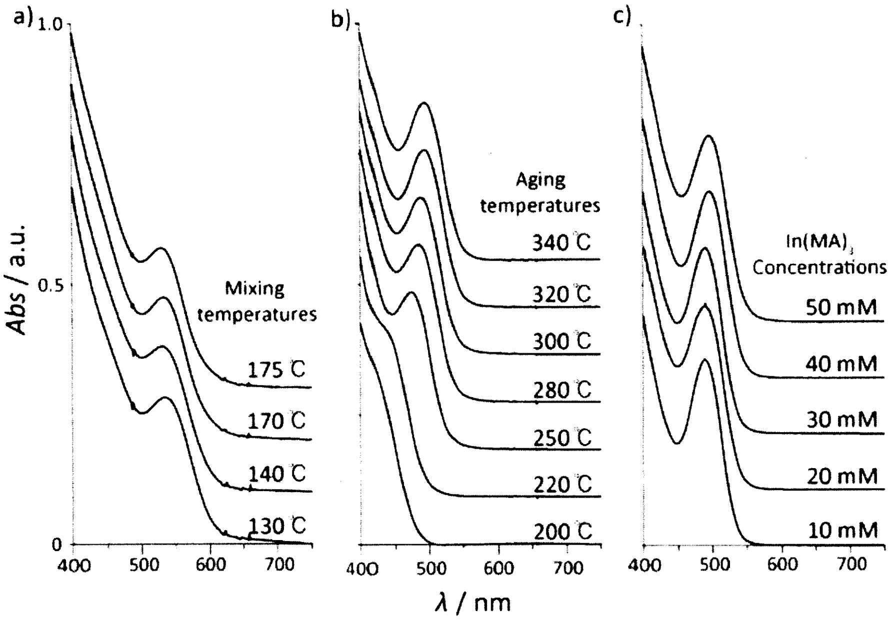

Figure 3.6: Absorption spectra of InP nanocrystals obtained at a variety of mixing and aging conditions. Micofluidic reactor operating with 40 mM In(MA)$_3$ and 20 mM (TMS)$_3$P at a) different mixing temperatures followed by aging at a constant temperature of 320 °C and b) constant mixing temperature at 150 °C followed by aging at different temperatures. c) Absorption spectra with different In(MA)$_3$ concentrations using temperature gradient in the first reactor stage and a 4 minutes residence time with a temperature of 320 °C in the second reactor stage.

The growth of InP nanocrystals appears to be largely independent of a traditional 'nucleation' process as the InP molecular precursors are rapidly depleted regardless of temperature.[65] These results are in stark contrast to the traditional models for monodisperse colloidal growth observed in the CdSe nanocrystal nucleation and growth.[70-71] In the absence of amines or other inhibiting reagents, the molecular phosphorus precursors are immediately depleted during mixing, independent of mixing temperature. The temperature dependence of the aging process can be rationalized as the growth of InP nanocrystals being dominated by non-molecular processes that are enhanced at higher temperatures. The non-molecular growth of InP nanocrystals could be the cause of non-spherical InP nanocrystals, in comparison to CdSe or PbSe nanocrystals grown from molecular species. The coalescence of non-molecular InP species may occur similarly to the recently reported coalescence growth model for gold nanoparticles.[75]

We investigated the effect of In(MA)$_3$ concentration on particle size and size distributions (figure 3.7-c), and found the synthesis to be largely independent of precursor or particle concentration. The independence of nanocrystal size on precursor concentration is in contrast with the behaviour of II-VI CdSe nanocrystals.[10]

3.4.3. Effect of excess fatty acid on particle size

We sought to investigate the role of free fatty acids on particle size. As this work and previous works indicates that InP nanocrystal growth is dominated by non-molecular processes, the introduction of free fatty acids could enhance inter-particle ripening processes by etching processes.[76] $In(MA)_3$ and $(TMS)_3P$ were mixed in a 2:1 ratio at 120 °C prior to the injection of excess myristic acid.

Free myristic acid was added following the depletion of molecular In and P precursors to ensure we probed the activity of carboxylic acids on inter-particle ripening processes, and not promoting molecular side reactions of carboxylic acids with the molecular P precursor.[18] The aging stage was kept at a constant temperature of 320 °C, with a constant residence time of 2.7 minutes.

Figure 3.7-a demonstrates that in the absence of free myristic acid (MA:In ratio of 3.0) the first absorption feature was located at 495 nm, corresponding to the formation of InP nanocrystals of approximately 2 nm in diameter.[77] With an increasing ratio of myristic acid to indium the first absorption feature shifted to longer wavelengths of up to 650 nm, corresponding to InP nanocrystals of 4.3 nm in diameter. The wide angle x-ray scattering (WAXS) confirmed a zinc blende InP structure, and Scherrer analysis of the peak shapes corresponded to the appropriate InP nanocrystal crystalline coherence lengths. In addition, the InP nanocrystal size and shape was probed by transmission electron microscopy (TEM), and further corroborated our assignment of size and structure to the InP nanocrystals (Figure 3.7-b, c and 3.8).

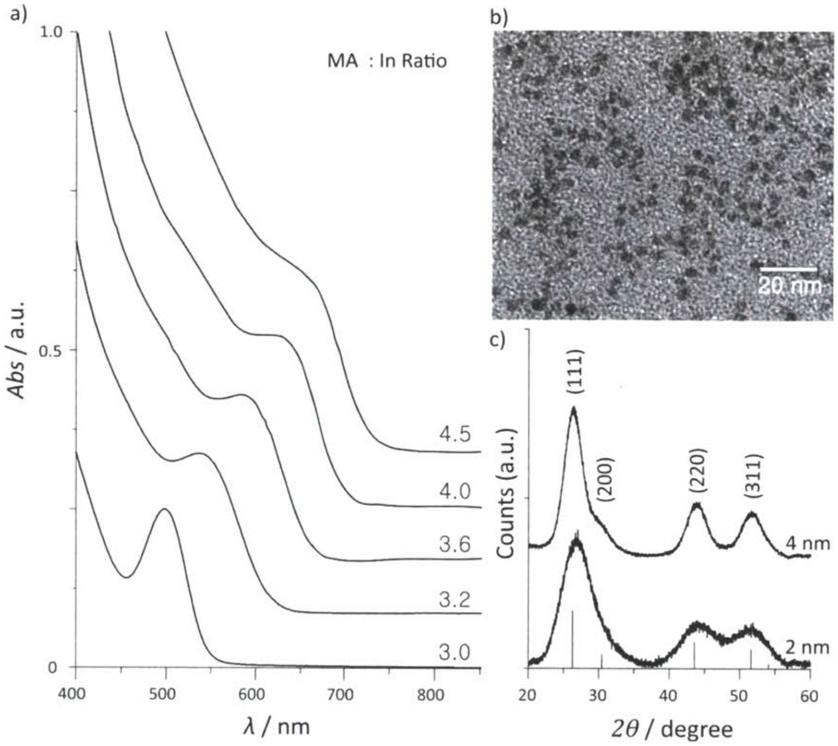

Figure 3.7: a) Absorption spectra of InP nanocrystals synthesized with various myristic acid to indium ratios. b) TEM image of 4 nm InP nanocrystals, and c) WAXS patterns of 2 nm and 4 nm diameter InP nanocrystals.

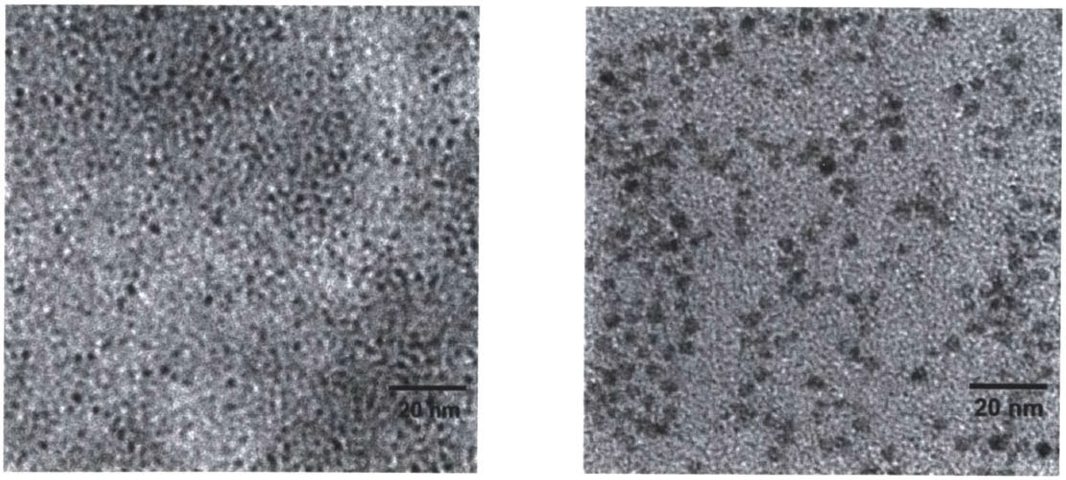

Figure 3.8: TEM images of two different sized InP nanocrystals synthesized without free myristic acid (size: ~ 2 nm, left) and with free myristic acid (MA : In = 4, size : ~ 4 nm, right)

The addition of excess myristic acid was found to be the dominant experimental parameter in the control of InP nanocrystal size. The excess myristic acid may promote the dissolution of active non-molecular InP species, such as monomers or small clusters, from the InP nanocrystal surface. The introduction of free fatty acids could enhance inter-particle ripening processes by etching process since carboxylic acids have strong binding on InP nanocrystal surface other than phosphines or amines. The active InP species can subsequently act as a source of precursors for the growth of InP nanocrystals in a classical ripening process.[56] However, other non-molecular processes such as the coalescence of particles may also contribute to the growth process. The dramatic effect of free myrstic acid on particle size is consistent with an inter-particle ripening model for InP nanocrystal growth.

3.4.4. InP nanocrystal growth via sequential injections

Another route to the synthesis of larger InP nanocrystals is the subsequent injection of additional molecular precursors (figure 3.9). As the molecular phosphorus precursors are immediately depleted following mixing, additional injections can be a source of In or P precursors.[66] By using a method analogous to the SILAR method of over-coating nanocrystals, we alternatively supply additional monomers of $(TMS)_3P$ and $In(MA)_3$ via six injection ports. In these reaction schemes, we utilized a continuous 3-stage microfluidic system that utilizes the third reactor stage for sequential injections (figure 3-c) following the mixing and aging stages. InP nanocrystals of approximately 2 nm in diameter were produced in the first two reaction stages, and this solution then directly injected to the third sequential injection microreactor for further growth. $In(MA)_3$ and $(TMS)_3P$ were injected via six alternating sub-injections. The flow resistance of each of the side injections was made to be one order higher than the resistance of the main channel by narrowing the channel widths to 80 μm and elongating the channel lengths in order to obtain uniformly distributed injections and to prevent any back flows. The flow resistances were calculated with a series solution of Navier-Stokes equation for rectangular channel dimensions.

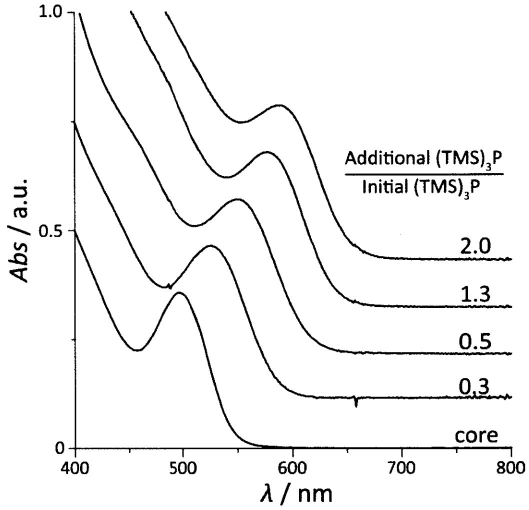

Figure 3.9: Absorption spectra of InP nanocrystals for various injection flow rates of In(MA)$_3$ and (TMS)$_3$P in the sequential injection stage of the microreactor. The InP nanocrystals were synthesized using a temperature gradient in the mixing stage followed by aging at 320 °C in the aging stage. Spectra are offset for clarity; absorbance is valid for the lower spectrum.

This continuous sequential injection process resulted in a growth of the first absorption peak from 495 nm to 595 nm corresponding to a size increase from 2 to 3.2 nm while maintaining a homogeneous size distribution. The growth of InP nanocrystals, through the method of sequential injection, allows for precise control over the growth of larger InP nanocrystals with size distributions as narrow, or narrower, than the InP nanocrystals grown via the ripening process.

3.4.5. InP nanocrystal growth from TMG$_3$P as a phosphorus source

We also synthesized InP nanocrystals with tristrimethylgermyl phosphine ((TMG)$_3$P) instead of (TMS)$_3$P (figure 3.10). The behaviour of the growth was similar to the growth from (TMS)$_3$P. The mixing temperature was not significant. However, we were able to obtain sharper peak with lower mixing temperature although the peak location stayed at the same position. As we increased the aging temperature, we were able to observe sharper first absorption peak. However, the first absorption peak shifted to blue as the aging temperature increased. This could be due to the stronger bonding strength between germane and phosphorus than the strength between silane and phosphorus. This bonding difference could effect on reactivity of the monomers as well as particle or nuclei stability after reacting with $In(MA)_3$.

3.5. Summary

In summary, we have developed a continuous three stage microfluidic system that separates the mixing, aging, and subsequent injection stages of InP nanocrystal synthesis. The microfluidic system operates at high temperature and high pressure enabling the use of solvents such as octane operating in the supercritical regime for high diffusivity resulting in the production of high quality InP nanocrystals in as little as 2 minutes. We have found that the synthesis of InP nanocrystals is largely independent of many experimental parameters that are significant in II-VI CdSe nanocrystal syntheses, such as mixing temperature and reagent concentrations. The dominant experimental parameter in the synthesis of InP nanocrystals is the concentration of free myristic acid in solution, which significantly contributes to the degree of inter-particle ripening processes. We speculate InP nanocrystal growth is dominated by non-molecular processes such as the coalescence of particles and inter-particle ripening. This work will help in the design of future III-V nanocrystal syntheses, as reagents that promote inter-particle ripening process may provide a means to control the size and shape of InP nanocrystals. The further development of microfluidic systems for the synthesis of III-V nanocrystals may provide a route to synthesize III-V nanocrystals with precise control of nanocrystal size and size distributions.

Chapter 4

Indium Arsenide Synthesis in Microfluidics

4.1. Introduction

Synthesis of semiconductor nanocrystals (quantum dots)[15, 26, 34, 78] has advanced in recent years as the tunable properties resulted from carrier confinements in three dimensions. The shift of the band gap to higher energy as the size of the nanocrystals become smaller is an example. These semiconductor nanocrystals are applicable to optical or electronic devices such as lasers, diodes, solar cells or bio-imaging.[28, 79-82] For those practical applications, synthesis of monodisperse nanocrystals is very important. In order to obtain such monodisperse nanocrystals, size focusing[15, 83-84] behaviour has been investigated on the growth of semiconductor nanocrystals such as CdSe, CdS, PbSe or PbS for the past decades. However those studies on the focusing of the nanocrystal size distribution have been done mostly on the II-VI group semiconductor nanocrystals.[70, 84]

InAs nanocrystals are a small band gap (0.354 eV, 300K) III-V semiconductor material that shows superior electronic and optoelectronic properties for near-infra-red (NIR) applications.[80] The band gap of InAs nanocrystals has been known to be ideal for NIR applications compared to any other semiconductor nanocrystals. However, synthesis of III-V semiconductor nanocrystals has been challenging due to synthetsis difficulties.[33] With the increasing interest, recently some groups have worked on the investigation of InAs synthesis in batch.[13-14, 16, 33, 66, 80, 83, 85-93] Previously, we developed a three-stage microfluidic system for the synthesis of indium phosphide (InP) nanocrystals, and we found important growth parameters.[9] The chemistry and synthetic method of the synthesis of InAs nanocrystals could be similar to the case of InP synthesis, owing the similar group-V monomer chemistry and precursor conversion being rapid for InP and InAs synthesis.[83] Systematic studies of the growth of InAs nanocrystals and identifying important growth factors could lead to increased understanding of III-V nanocrystal synthesis.

Traditionally, semiconductor nanocrystals are prepared by batch processes.[26, 94] In most III-V nanocrystal synthesis, the group-V precursors are injected into a heated flask containing a mixture of group-III precursors, solvents, and surfactants.[13-14, 33, 83] However, it is very difficult to control a series of manual processes including injection and preparation of precursor solution with precise concentration. Considering that the material ratios between anionic and cationic materials are important in the particle growth of the both II-VI and III-V materials,[9, 12] those difficulties limit the practicality of systematic study of nanocrystal growth in batch mode. Furthermore, temperature and concentration fluctuations after the injection process, as well as the quenching process after the reaction are very difficult to control precisely. Continuous-flow systems operating at steady-state offers to better control and reproducibility, which is critical in nanocrystal production and enables precisely controlled systematic study of nanocrystal synthesis.[5, 8-9] This advantage is especially important in studies of nanocrystal growth incorporating a very fast monomer reaction such as InAs or InP nanocrystal synthesis.

A high-pressure and high-temperature microfluidic system provides an increased parameter space by enabling the usage of solvents, precursors, and ligands not accessible in traditional batch system. The use of solvent in supercritical phase[21] offers high diffusivity and improved mixing, as well as allows for better ability to solubilize compounds than typical solvents employed in batch system. In addition to the above mentioned advantages of microfluidic systems such as excellent reproducibility,[19] multi-step microfluidic systems allow for even better a step-by-step control over reaction parameters. Moreover, in-situ monitoring device such as in-line UV-Vis connected to the multi-step system allows for fast screening of reaction parameters.[4, 9]

We were able to obtain InAs nanocrystals with controlled sizes with narrow size distributions. We found the mixing temperature was not significant in the synthesis of InAs nanocrystals, and aging temperature was very important in InAs growth. This behavior is similar to the growth of InP nanocrystals. However, we also observed that InAs nanocrystals grow further as the aging temperature increases, and the photoluminescence spectra became wider indicating that the size distribution was broader. Different from InP nanocrystals growth, we also found that InAs nanocrystal growth was not significantly affected by excess fatty acid. By utilizing temperature gradient microreactor, we were also able to synthesize InAs nanocrystals in as short as 30 seconds or less.

4.2. Methods

4.2.1. Multi-stage microfluidic system

In order to investigate InAs nanocrystal growth, we used a two-step microfluidic system consisting of mixing and aging microreactors.[9] Details of the system were described in Chapter 3. This microfluidic system enabled precise tuning of important synthetic parameters for the synthesis of InAs nanocrystal to study of the growth mechanism systematically.

4.2.2. Preparation of precursor solutions

Indium myristate ($In(MA)_3$) and tristrimethylsilyl arsine (TMS_3As) was used as the precursors. $In(MA)_3$ was dissolved in octane containing 10 vol% tri-n-octylphosphine, and TMS_3As was dissolved in pure octane. Each concentration of those two materials was 30 mM.

4.2.3. System operation

The operations of the experiment were similar to those described in Chapter 3. $In(MA)_3$ solution was mixed with a 2:1 ratio with TMS_3As at the mixing stage. The mixing temperatures were changed from 110 °C to 210 °C, and the residence time at the mixing stage was 2 minutes. The solution was continuously transferred to the next aging stage maintained at 300 °C, and remained in the reactor for 1.5 minutes.

4.3. Results

4.3.1. Effect of temperatures at the mixing and aging stages

We were not able to observe significant effect of the mixing temperatures on the size of InAs nanocrystals (figure 4.1). This could be because the reaction between $In(MA)_3$ and TMS_3As above 110 °C was fast enough, so that the molecular monomer precursors were immediately depleted,[83] and the particle growth was solely by inter-particle process which was also observed from InP growth.[9, 65] The photoluminescence spectrum of the InAs nanocrystals showed red-shift as the mixing temperature increases (figure 4.2). This indicates that the tiny InAs nanocrystals start to grow via inter-particle processes[56, 84] as low as 110 °C. However, the amount of the peak shift between 110 °C and 210 °C mixing temperatures was not significant (less than 10 nm) compared to the entire tunable emission ranges of InAs nanocrystals.

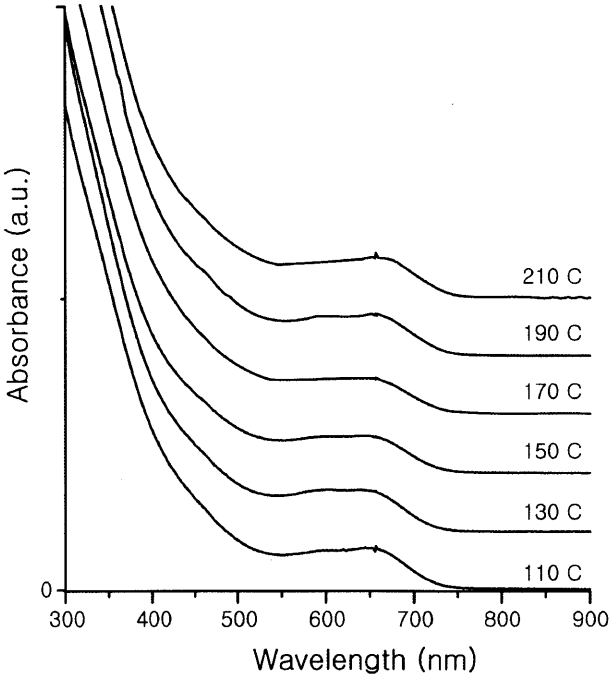

Figure 4.1: The effect of mixing temperatures: absorbance spectra of InAs nanocrystals synthesized with two-step microreator system: mixing and aging reactors. Mixing temperature was controlled from 110 °C to 210 °C, and aging temperature was maintained at 300 °C.

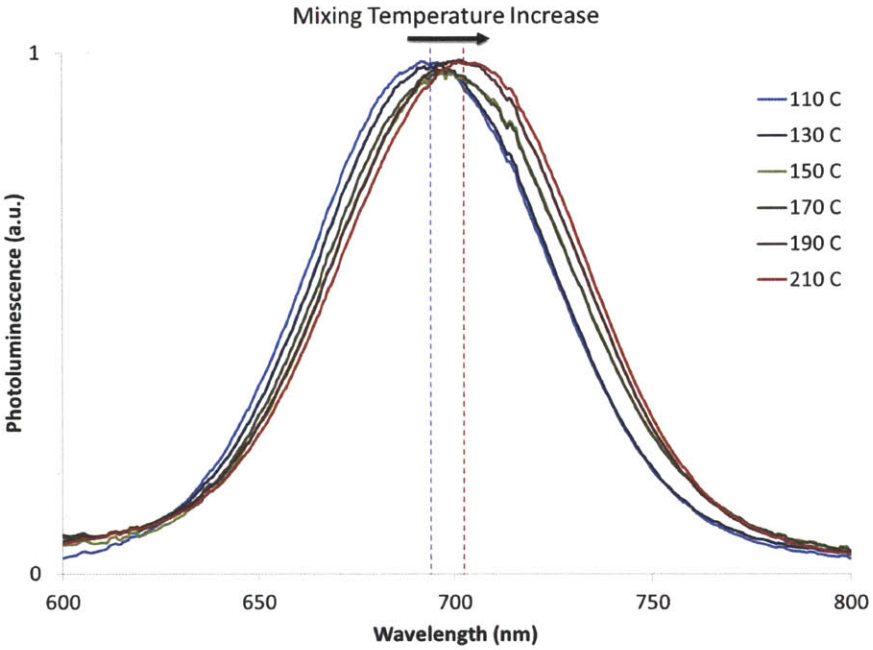

Figure 4.2: Photoluminescence spectra of InAs nanocrystals synthesized at different mixing temperatures. As the mixing temperature increases, the peak shifts to the red. However, the degree of the shift is not significant (< 10 nm).

Next, we fixed mixing temperature at 150 °C and controlled the aging temperature from 150 °C to 330 °C (figure 4.3). The first absorption feature shifted significantly to red as the aging temperature increased (figure 4.3-a). This indicates that the growth of InAs could follow inter-particle processes, different from II-V or II-VI quantum dot growth from low reactive monomer precursors. Rather, InAs growth could follow a similar growth mechanisms to InP growth as reported in Chapter 3. Within a short residence time (2 minutes) at the aging stage, well defined first absorption features started to be observed above 200 °C. At this temperature, the absorption peaks originating from the magic-sized nanoclusters, located at 420 and 460 nm, disappeared.[83] This indicates that the rate of the inter-particle process at 200 °C is fast enough to obtain monodisperse InAs within 2 minutes.

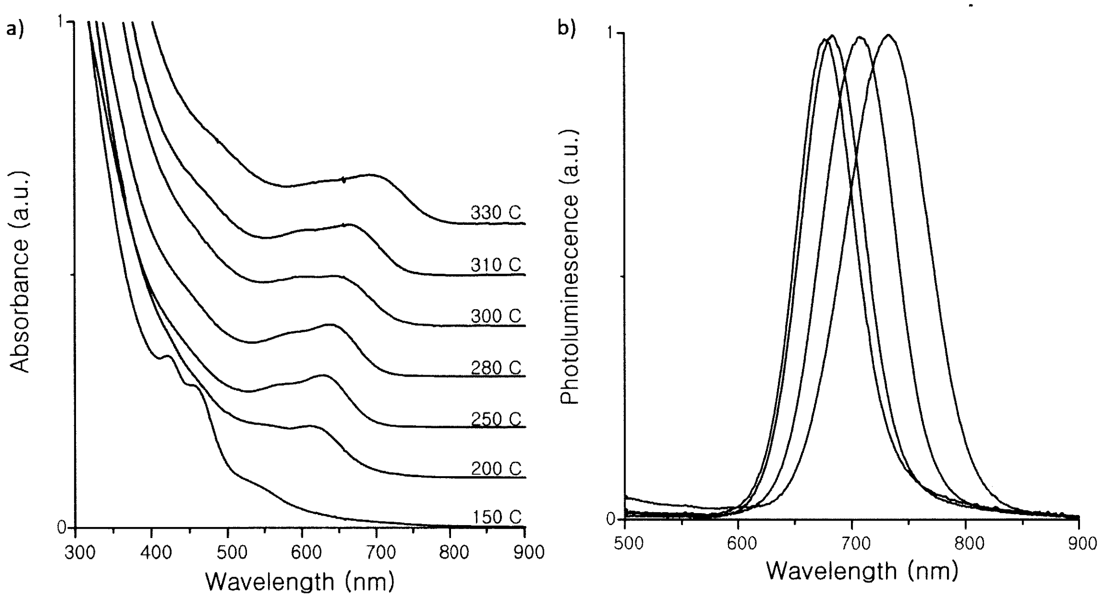

Figure 4.3: a) Absorbance and b) photoluminescence spectra of InAs nanocrystals. The mixing temperature was fixed at 150 °C and the aging temperatures were changed. As the aging temperature increases, the first absorption peaks and the photoluminescence peaks shift to red indicating larger InAs nanocrysal sizes. b) The aging temperatures of the emission spectra are 280 °C, 300 °C, 310 °C, and 330 °C from the left to right.

We were able to tune the emissions simply by changing the aging temperatures (figure 4.2-b). The resulting emissions from the InAs QDs ranged from 650 to 780 with narrow FWHMs that are optimal, especially for bio-imaging applications. Although the location of the first absorption feature of the InAs nanocrystals synthesized at lower than 250 °C was not much different from the nanocrystals at above 280 °C, the intensity of the photoluminescence of the InAs nanocrystals synthesized at low temperature was much weaker than the others (QY is less than 1%). The FWHMs of the emissions were as narrow as 54 nm (aging temperature at 280 °C). However, the FWHMs also broadened as the aging temperature increases. The photoluminescence peak shape became asymmetric at high aging temperature. This photoluminescence peak broadening, and shape change at high temperatures could also be indicative of inter-particle growth, and suggests that thermal growth by a high-temperature ripening process[56] would not a good strategy to obtain nomodisperse InAs nanocrystal.

As we observed, InAs nanocrystals can grow further when the aging temperature is increased from 300 °C to 330 °C. However, by comparing the InAs nanocrystal growth with the reported InP growth, it is reported that InP is not growing much above 300 °C. The first absorption spectrum stays at the same position even at an aging temperature between 300 °C and 340 °C at least within a residence time of 1.5 minutes.[9] Considering that all the monomers in the solutions were depleted, and particles were growing solely my inter-particle processes, we speculate that this could be related to the lower melting point of InAs (942 °C) than InP (1062 °C) or bonding strength difference between trimetylsilyl (TMS) group and arsenic from between TMS and phosphorus. However, the thermally driven growth behavior of InAs needs further investigation.

4.3.2. Fast InAs nanocrystal synthesis with temperature gradient microreactor

Since the mixing temperature for the InAs synthesis is less important than aging temperature, and the nanocrystal growth is dominated by inter-particle process, which is similar to the InP synthesis, a single microreactor with temperature gradient has been used for the synthesis.[9] We successfully synthesized InAs nanocrystals in a short residence time (as short as 40 seconds) without any clogging or deposition in the microreactor. The emissions were tunable from 655 nm to 672 nm simply by changing the residence time from 40 seconds to 2 minutes. The FWHM of the emissions were as narrow as 53 nm (figure 4.4).

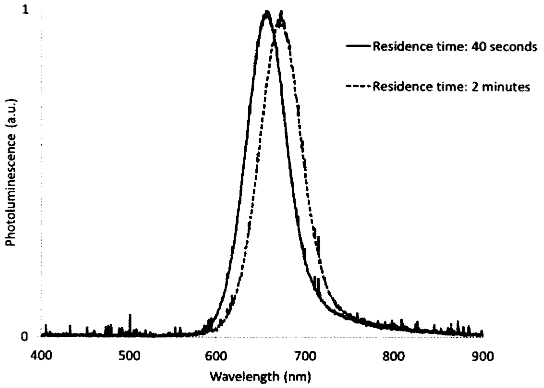

Figure 4.4: Photoluminescence spectra of InAs nanocrystals synthesized using single microreator with gradient temperature (maximum temperature: 280 °C). InAs nanocrystals were synthesized in a short residence time (40 seconds).

4.3.3. Effect of excess fatty acid on InAs nanocrystal growth

We also investigated the effect of the excess carboxylic acid on the particle size and size distribution. With a two-stage microfluidic system, we controlled the additional fatty acid, oleic acid (OA) amount. The OA was dissolved in octane prior to the injection. The excess oleic acid was mixed with $In(MA)_3$ first, and then mixed with TMS_3As at the mixing stage. The mixing stage operated at 150 °C and the aging stage at 300 °C. The total residence time of the InAs control sample in figure 4.5 was at 3 minutes, and as we increase the amount of OA amount, the residence time decreased to 2 minutes. However, as we increase the flowrate of OA solution, we were not able to find any significant effect of excess fatty acid that observed from InP growth (figure 4.5).[9,66] We only were able to observe a little blue shift, potentially caused by the shorter residence time owing to the additional flow injection.

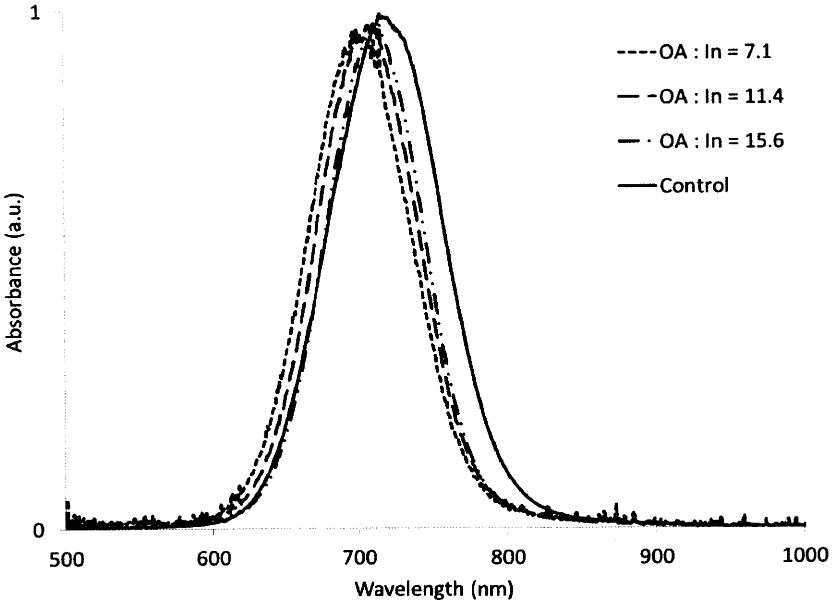

Figure 4.5: Photoluminescence spectra of InAs nanocrystals with different oleic acid concentration.

4.3.4. Growth via sequential monomer injections

Since the InAs growth is an inter-particle process that was unaffected by excess fatty acid, we were unable to tune particle size by surfactant chemistry. Instead we synthesized larger InAs nanocrystals by injecting more monomer precursors into the system. A sequential injection microreactor[9] is a great tool for the larger particle growth in a short time. Using a three-stage microfluidic system, we were able to grow InAs particles further (figure 4.6). Small InAs nanocrystals were synthesized using a two-stage system. Each concentration of the $In(MA)_3$ and TMS_3As solution in octane was 30 mM. The mixing temperature was maintained at 150 °C and the temperature at aging stage was at 320 °C. 50 mM of $In(MA)_3$ and 30 mM of TMS_3As were injected at the third sequential injection microreactor. The first absorption spectra shifted from 675 nm to 755 nm, indicating that the particle sizes were grew from 1.5 nm to 1.9 nm in diameter within 2.5 minutes.

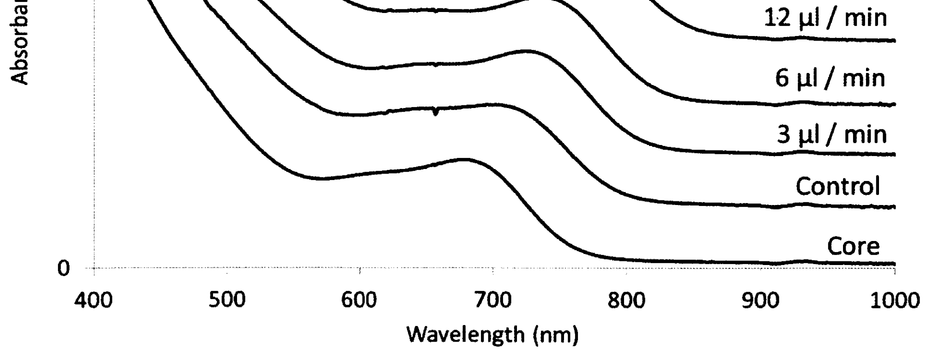

Figure 4.6: InAs nanocrystal growth by sequential injection microreactor. InAs core was synthesized in a two-stage microfluidic system, and the core was continuously flowed to the third stage, sequential injection microreactor. The temperature was maintained at 320 °C.

4.4. Summary

In summary, we investigated temperature effects on InAs nanocrystal growth, and found the aging temperature was more significant. Although this temperature dependency on the nanocrystal growth is similar to those on the growth of InP nanocrystals, InAs nanocrystals continue to grow larger at higher aging temperature above 300 °C, which is not observed in InP growth. Furthermore, different from the reported InP growth, InAs nanocrystal growth did not show any dependency on excess fatty acid. These growth differences could be owing to the material property difference between InAs or InP. By utilizing sequential injection microreactor, we were able to grow InAs nanocrystals from 1.5 nm to 1.9 nm in diameter.

Chapter 5

InP / ZnS Core-Shell Structured Nanocrystal Synthesis

5.1. Introduction

Colloidal semiconductor nanocrystals (quantum dots) have been of interest due to their tunable optical and electronic properties. These properties come from the quantum confinement with their applications in bio imaging, lasers, and photovoltaic devices.[45, 49-50, 95-96] So far, quantum dot research has mostly focused on II-VI group materials such as CdSe, CdTe, PbSe or PbS due to their ease of synthesis. However, those quantum dots (QDs) have intrinsic toxicity, and therefore their applications are limited. Indium phosphide (InP) QDs is becoming scientifically and commercially important as a replacement for CdSe because of their low environmental toxicity and visible to near infrared tunable emissions. Unfortunately, the photoluminescence (PL) quantum yield of the bare InP QDs is quite low (typically less than 1%) due to non-radiative energy loss on the surface. Passivation of the InP core with higher band gap materials such as ZnSe, ZnS or ZnSeS to form type-I core-shell structures enhances the PL quantum yield,[27, 34-36, 41, 97] enabling InP QDs to be used in practical applications in electronics or life sciences with or without ligand exchange on the QD surface.

Unfortunately, the synthesis of large quantities of structured QDs with uniform and desired properties faces synthesis challenges. QDs are commonly synthesized in batch, and the properties vary batch to batch. Furthermore, scale-up of the synthesis has also been challenging due to limited mixing and temperature control.[26, 37-38, 60, 98] Continuous synthesis could be a solution for well controlled or on-demand production with uniform and excellent material properties.[10, 72, 99-100] However, continuous synthesis of structured QDs such as core-shell structure has not been frequently reported.[72] This is because maintaining low concentrations of the shell materials in a continuous process has been greatly challenging, which is critical in most core-shell structured QD synthesis to suppress undesired secondary nucleation.

A multi-step continuous microfluidic system allows for the precise control over reaction conditions,[9, 19] enabling efficient investigation of reaction parameters in chemical synthesis, and controlled synthesis of multi-structured nanomaterials such as core-shell quantum dots.[72] Since microreactors have a high surface to volume ratio, these provide great reproducibility as a result of accurate control of heat and mass transfer.[3, 7] Silicon-Pyrex microreactors allow for the use of high pressure and high temperature up to about 300 bar and 450 °C as well as providing great chemical resistance (as a glass-like material) and optical access to the reaction media.[23] High temperature and high pressure operating conditions open up selection of chemicals such as solvents, ligands or precursors that cannot easily be used in batch,[8, 25-26] offering increased reaction space of synthetic conditions. For example, the utilization of supercritical conditions in quantum dot synthesis narrows the size distribution of nanocrystals by offering homogeneous reaction conditions.[21] This microflow system can be combined with an in-line monitoring system such as UV-Vis or photoluminescence that allows rapid screening of reaction conditions.[4, 6, 8]

5.2. Methods

5.2.1. Multi-step systems for InP / ZnS core-shell nanocrystal synthesis

We built a continuous synthesis of InP / ZnS core-shell QDs with a multi-step microreactor system operating at high pressure and high temperature without incorporating any manual batch procedures between steps. We designed a special silicon-based microreactor with 10 sub-channels for a ZnS shell formation on an InP core in order to maintain low concentration of the shell materials. We have overcoated an InP core with a ZnS shell using a three-step microreactor system, following a three-step InP core synthesis. We were successfully able to tune emissions from green to near infrared by controlling InP core size. The resulting InP / ZnS core shell QDs showed narrow photoluminescence emissions at different wavelengths. The quantum yields of the resulting core-shell QDs are as high as 40%. This continuous system has also been applied for the synthesis of other structured QDs such as indium phosphide / cadmium sulfide (InP / CdS) and indium arsenide / indium phosphide (InAs / InP) core-shell QDs.

Figure 5.1-(a) shows the continuous multi-step system for the synthesis of InP / ZnS core-shell QDs consisting of mixing, aging, sequential growth, two shell formations, and annealing steps. High quality InP cores with different sizes were synthesized in octane with the first three reactors: mixing, aging and sequential growth microreactors.[9] A ZnS shell was grown on the core with the next three reactors. Gradient temperature[9] was used as the mixing reactor to prevent any side effects such as clogging or deposition in the channels because tristrimethylsilyl phosphine ($(TMS)_3P$) is thermally unstable, and mixing temperature was not significant for InP core synthesis.[9] The reaction temperatures of the reactors were maintained at constant temperatures except for the first mixing microreactor. Octane, as a low-molecular-weight solvent and as a supercritical phase[10, 21, 101] at high temperature (at the second step, aging reactor), provides excellent mixing and low dispersion.

5.2.2. Microreactor fabrication

Preparation of the silicon-based microreactors was conducted as previous reported with some modification.[23] We put 4.5 μm silicon oxide as a hard mask on a silicon wafer with a diameter of 6 inch and a thickness of 800 μm; we grew 0.5 μm silicon oxide on the silicon wafer by wet-oxidation process (MRL industires, Model 718), and 4 μm silicon oxide by dielectric PECVD process (Applied Materials, Centura 5300). Thin positive photoresist with a thickness of 1 μm was spin-coated on the top of the silicon oxide layer. Model MA6 (Karl Suss) was used as a mask-aligner. This process allowed for precise channel development. An in-line UV-Vis measurement device was designed and fabricated in aluminum, type 316 stainless steel and quartz as described in Chapter 2. This in-line device was connected with Ocean Optics DH-2000 deuterium tungsten halogen light source and SD2000 fiber-optics spectrometer. Stainless steel tubes with a inner diameter of 0.02 inch was used for connections between reactors.

Figure 5.1-(b) is the picture of the shell formation microreactor with 10 side channels. The width and depth of main channel are 400 μm and 420 μm and corresponding dimension of the side channels are 80 μm and 100 μm respectively. We used silicon oxide hard-mask in order to fabricate channels precisely. Each side channel has 30 times higher flow resistance than the main channel to prevent any back flows. This high flow resistance also helps to maintain uniform flow distribution when the flowrates of each injection (main, and two side injections) changes.

5.2.3. Preparation of precursor solutions

The solvents, octane (anhydrous, 99 %) and dodecane (anhydrous, 99%) were purchased from Sigma-Aldrich. These solvents were degased by freeze-pump-thaw method and dried with 4 Å molecular sieves. Tri-n-octylphosphine (TOP, 97 % min.) was purchased from Strem and was dried with 4 Å molecular sieves prior to use. $(TMS)_3P$ from Strem and $(TMS)_2S$ from Sigma-Aldrich were used without further purification. Myristic acid (99%), oleic acid (90%), and 1-hexanethiol (95%) were purchased from

Sigma-Aldrich. Zinc acetate ($Zn(ac)_2$, anhydrous, 99.98% metal basis) was obtained from Alfa Aesar and cadmium acetate ($Cd(ac)_2$, anhydrous, 99.9% metal basis) was purchased from Strem. $In(MA)_3$ solution was prepared as previously reported.[102] $Zn(OA)_2$ or $Cd(OA)_2$ was prepared by reacting 1 mmol of $Zn(ac)_2$ or Cd(ac)2, with 2 mmol of oleic acid under vacuum (<70 mTorr) at 140 °C for 2 hours, and dissolved in dodecane containing 15 vol % of TOP in a dry box. Elemental sulfur (S) was obtained from Alfa Aesar, and dissolved into TOP for CdS shell synthesis in order to obatin1.5 M TOP-S. Tristrimethylsilyl arsine (TMS_3As, 99%) was obtained from Nanomeps. Different sizes of InP cores are synthesized as previously reported.[9] $Zn(OA)_2$ and TMS_2S were used for the ZnS shell, Cd(OA) and TOP-S were used for CdS shell, and TMS_3P and $In(MA)_3$ were used for InP shell formation. All the shell materials were diluted to 20 mM in octane containing 20 vol % of TOP.

5.2.4. Characterizations

Absorbances were measured by Hewlett Packard 8452 diode-array spectrometer. All the solutions were diluted in hexane prior to the measurement. Emissions are measured with SD2000 fiber-optics spectrometer. TEM images were obtained with JEOL 200CX transmission electron microscope. XRD data were acquired using Rigaku H3R. Quantum yields are measured by comparing the integrated emission of the QDs in hexane with the emissions of the dyes (RD 580, and 600, 630) in methanol and ethanol. Solutions of QDs and dye were optically matched at the excitation wavelength. Quantum yields (QYs) were calculated from the following expression: $QY_{QDs} = QY_{Dye} \times (\text{Peak Area}_{QDs} / \text{Peak Area}_{Dye}) \times (n_{QDs}\ \text{solvent})^2 / (n_{Dye}\ \text{solvent})^2$.[69]

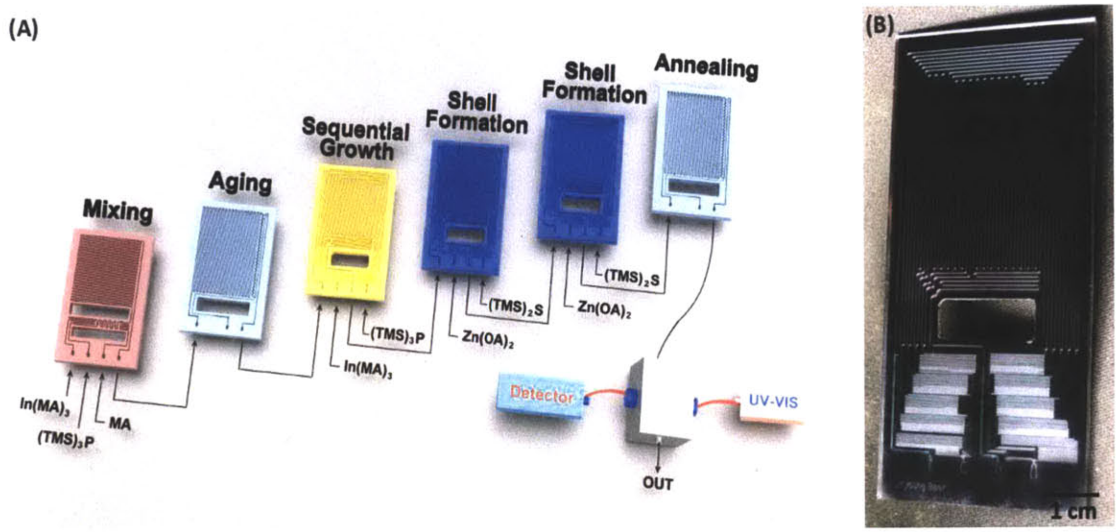

Figure 5.1: (a) The multi-stage microfluidic system for the synthesis of InP / ZnS core-shell QDs operating at 65 bar. The first three-steps (mixing, aging and sequential growth reactors) are for InP core synthesis and the following three-steps (two shell formation reactors and an annealing reactor) are for a ZnS shell synthesis. Each reactor is made of silicon-Pyrex and the channel dimensions are ranging from 80 – 400 μm. The subsequent in-line optical device can also be operated over 80 bar, and enables real-time UV-Vis and photoluminescence measurements, resulting in fast screening of reaction parameters by monitoring of the properties of the products. (b) The picture of the shell formation microreactor consisting of 10 side channels. OA=oleic acid, MA=myristic acid, and TMS=trimethylsilyl.

5.2.5. Size-tuning of InP nanocrystal cores

Size-tuning of the InP core was mostly achieved with the sequential growth microreactor (figure 5.1-(a)). Monodisperse InP cores, which were less than 2 nm in diameter and, therefore, showing the first absorption feature at 510 – 520 nm, were synthesized in the first two steps: mixing and aging reactors. The small InP QDs were grown up to about 3.2 nm in diameter by alternate injections of additional molecular precursors at the third sequential growth microreactor. We followed the previous reported reaction conditions for these core syntheses.[9] In order to synthesize even larger InP core than 3.2 nm in diameter, we added 1 - 2 mol % excess myristic acid (MA) to the the indium precursor at the mixing reactor. The InP cores with various controlled diameters are continuously flowed into the shell formation microreactors without incorporating any manual purification processes.

5.2.6. Shell formation procedure

Zinc oleate ($Zn(OA)_2$) and bis(trimethylsilyl) sulfide ($(TMS)_2S$) were used for a ZnS shell formation. Each $Zn(OA)_2$ and $(TMS)_2S$ solution dissolved in octane containing 20 vol % of tri-n-octylphosphine was sequentially injected into the main reaction stream at the shell formation reactors. In order to maintain a low concentration of the shell materials to prevent undesired ZnS nucleation, we designed a microreactor having 10 sub-channels. Typically, each precursor concentration of the shell material was 20 mM, and the each precursor flow was divided into 5 sub-channels before injected to the main channel. The temperature of the shell formation microreactors was at 250 °C, and the residence times were ranged 6 to 8 minutes depending on InP core flowrates. We typically used two of the shell formation microreactors to maintain even lower concentration of shell precursors. We added an extra reactor for annealing after shell formation. We also have manually designed an in-line optical measurement device that can be operated above 80 bar in order to monitor optical properties such as UV-Vis absorbance and photoluminescence measurements of the QDs as a real-time.

5.3. Results (InP / ZnS core-shell nanocrystals)

5.3.1. Optical characterization

Figure 5.2-(a) is a color photograph showing the spectral range of InP / ZnS QD solutions at 365 nm UV excitation. Each InP / ZnS core-shell QDs are diluted in hexane solutions and placed in quartz cuvettes. As the InP core size increases, the luminescence color changes from green to red. Figure 5.2-(b, c) shows absorption and emission spectra from the four different InP / ZnS core-shell QDs. The PL maxes of InP / ZnS core-shell locate at 554 nm, 599 nm, 630 nm, and 681 nm. The FWHM of the QDs are as low as 175 meV (42 nm) for those emitting at 554nm and 177 meV (56 nm) for the QDs emitting at 630 nm.

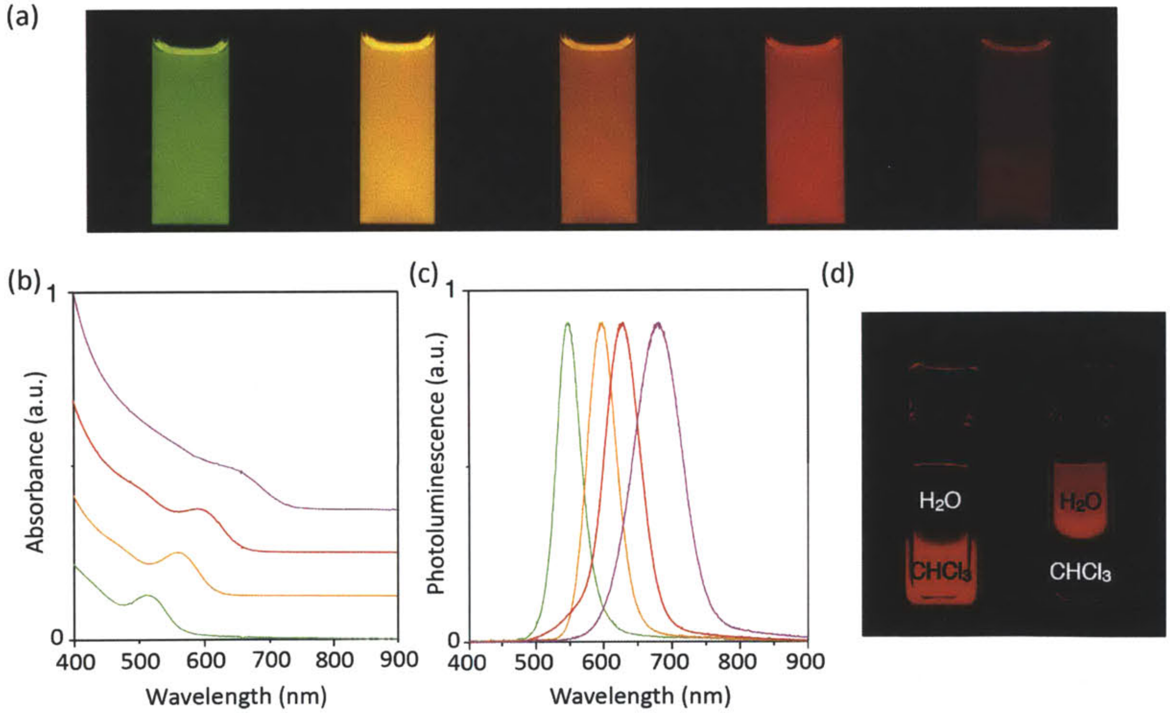

Figure 5.2: (a) Photograph of size series of InP / ZnS QDs in hexane illuminated under 365 nm UV light. Their PL peaks locate at 554, 599, 605, 630, and 681 nm (from left to right). (b) Absorption and (c) normalized emission spectra from the different InP / ZnS QDs. (QDs showing 605 nm emission are not shown in (c, d).) (d) Phase transfer of InP / ZnS QDs from chloroform to water phases after ligand exchange with 3-mercaptopropionic acid: before ligand exchange (left) and after ligand exchange (right). These samples are also illuminated with 365 nm UV light.

These narrow emissions could be attributed to the advantages of the flow synthesis. Previously, it was reported that CdSe QDs synthesized using a microreactor with supercritical hexane showed as narrow as or narrower emissions than synthesized in batch or in flow with single phase or segmented phase.[10] Utilization of the supercritical octane at the aging reactor (the second step) could allow for the narrow size distributions, resulting in the narrow emissions. Size tuning by the sequential injection microreactor (the third step) enabled to tune the size of InP cores without significant broadening of size distribution.

The FWHMs of the NCs emitting longer than 630 nm became broader presumably due to the ripening of the particles. We were able to control the InP core size successfully solely with sequential addition up to 3.2 nm in diameter that corresponded approximately 610 - 630 nm emission without significant size broadening. However, we added 1 to 2 % excess MA to $In(MA)_3$ to synthesize the InP core with a diameter of larger than 3.2 nm due to limited residence time and number of additional injections.
We speculate that the excess MA could promote the ripening of the InP NCs, and broaden the particle size distribution.[9] Adding more sequential growth microreactors to grow larger InP core could be a solution to reduce the FWHMs of long wavelength emissions, but this would require a reactor with large volume (milliliter scale) and with more side channels.

The PL quantum efficiencies of the InP / ZnS core-shell nanocrystals were as high as 40% for 554 nm emitting QDs and 32% for 630 nm emitting QDs after one purification step. We purified InP / ZnS QDs by adding ethanol and acetone, precipitating out by centrifuge, and re-dispersing in hexane. The quantum efficiency decreased as the InP core size increased. This could be because the smaller InP core has higher surface energy that enables better ZnS overcoating. Due to the difficulty of the shell formation on large cores, the PL quantum efficiency of InP / ZnS core-shell QDs emitting at 681 nm was as low as 5%, but we still were able to observe emission peak without any deep-trap emissions from the surface of the QDs. For practical applications such as bio-imaging, the InP / ZnS core-shell QDs were transferred to PBS (phosphate buffered saline) phase after ligand exchange with 3-mercaptopropionic acid, and we were still able to observe photoluminescence after the ligand exchange (Figure 5.2-(d)). This ligand exchange and phase transfer also indicates stable a ZnS shell formation on InP cores.

5.3.2. Characterization with TEM, XRD, and WDS

The sizes of InP / ZnS core-shell QD samples showing different emissions were measured with a transmission electron microscope (TEM) (Figure 5.3-(a,b)). Their first absorption (photoluminescence) features were located at 590 nm (630 nm) and at 657 nm (681 nm), and the estimated core sizes from literature data that correlates the InP sizes with the first absorption peak were 3.1 and 4.5 nm in diameter without considering red-shift of the first absorption peak by the ZnS shell formation.[77, 103] The actual InP core sizes could be smaller than those once the red-shifts were considered. The average sizes of InP / ZnS core-shell QDs from TEM images were 4.1 and 4.9 nm. Wide angle X-ray diffraction (WAXS) showed the zinc blende structure of InP and InP / ZnS core-shell nanocrystals. The small shift of the peaks between InP QDs and InP / ZnS core-shell QDs indexed to the (111), (220), and (311) planes indicates the existence of ZnS shell structures.[103-104]

We also measured the composition of these samples with wavelength dispersive spectroscopy (WDS) after repeated purification steps, and the amount of elements of Zn and S was consistent with the size change after the ZnS shell formation. (Table 5.1). Most of InP / ZnS core-shell QD samples emitting between 554 nm to 630 nm had 1 to 1.5 monolayers of ZnS shell from the size differences and WDS analysis. Unfortunately, we also were able to observe ZnS shells with less than a monolayer from the sample emitting at 691 nm (Figure 3-(b)). This sub-monolayer passivation could explain the relatively low observed PL quantum efficiency. The ZnS shell formation on large InP cores (larger than approximately 3.5 nm) still remains a challenge.

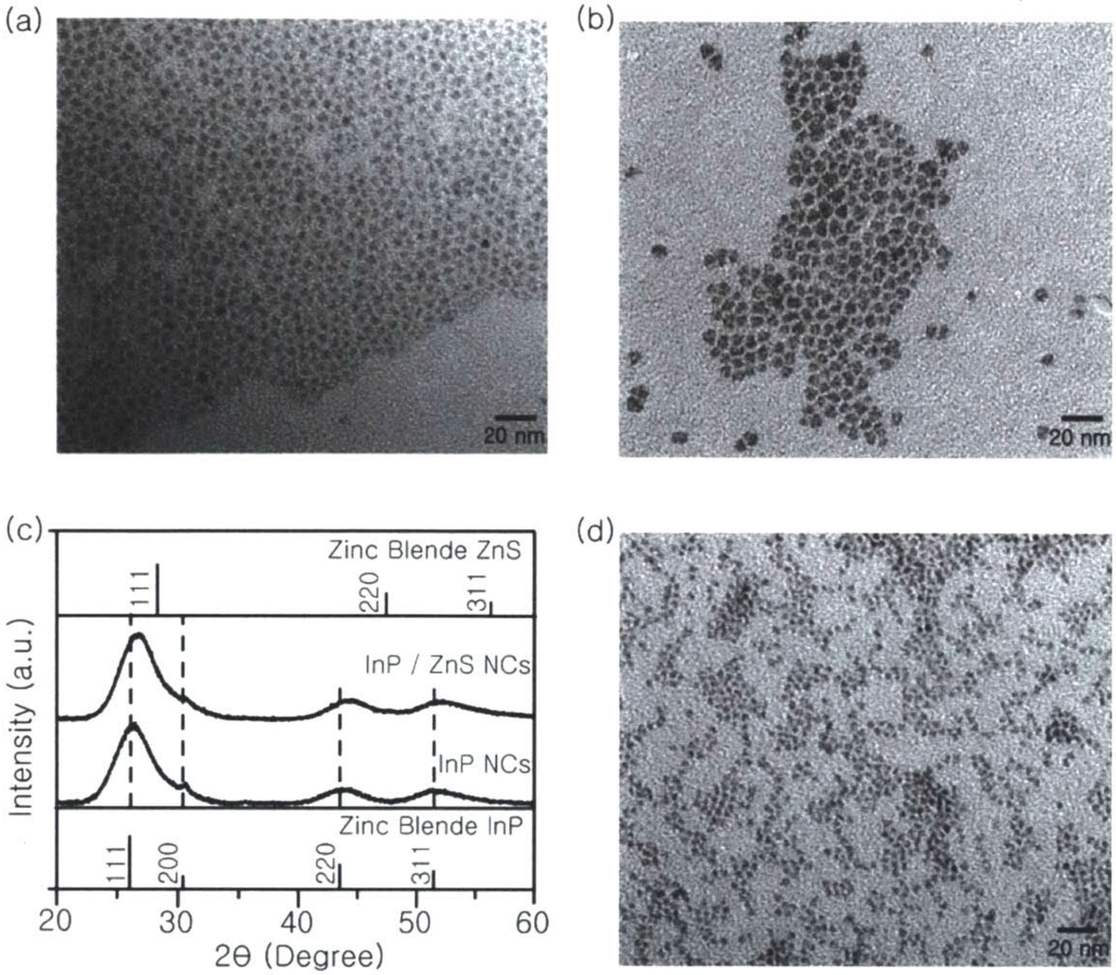

Figure 5.3: TEM images of InP / ZnS core-shell QDs synthesized with Zn(OA)$_2$ and TMS$_2$S emitting (a) at 630 nm and (b) at 681 nm. (c) WAXS of InP core and InP / ZnS core-shell QDs. (d) InP / ZnS core-shell QDs grown with 1-dodecanethiol and 1-hexanethiol instead of TMS$_2$-S.

Table 5.1: Molar compositions of InP / ZnS core-shell nanocrystals showing different emissions.

Photoluminescence Emission Peak (nm)	In (atomic %)	P (atomic %)	Zn (atomic %)	S (atomic %)
554	20.4	16.5	26.5	36.6
599	21.4	18.1	25.6	34.9
605	21.0	18.9	27.5	32.6
630	18.2	17.6	28.0	36.1
681	42.5	39.4	9.3	8.8

5.3.3. ZnS shell formation from thiols as a sulfur source

We also synthesized the ZnS shell also with different sulfur precursors. Alkyl thiols have been used as a sulfur source for metal sulfides synthesis, and thiols with a shorter alkyl chain have been known to be more reactive.[58] We used 1-dodecanethiol and 1-hexanethiol. First, 20 mM of $Zn(OA)_2$ and 1-dodecanethiol were premixed in octane containing 15 vol% TOP, and injected via side channels at the first shell formation microreactor in figure 5.1-(a). 1-dodecanethiol was dried at 95 °C under vacuum (< 100 mTorr) for 2 hours prior to use. Total residence time at the first shell formation microreactor was 3.5 minutes and the temperature was maintained at 270 °C. Next, 20 mM of premixed $Zn(OA)_2$ and 1-hexanethiol solution was injected at the second shell formation microreactor. The residence time was 2.5 minutes, and the reaction temperature was at 330 °C. The solution was continuously flowed to the last annealing reactor typically maintained at 330 °C.

Figure 5.3-(d) is TEM image of the InP / ZnS core-shell QDs grown with thiols, emitting at 558 nm. The average size of the nanocrystals was 3.8 nm in diameter, and the estimated core size was less than 2.3 nm. The photoluminescence quantum efficiency was as high as 35%. However, the FWHM values of the photoluminescence from InP / ZnS synthesized using thiols were slightly broader (about 3 – 10 meV) than the case with TMS_2-S (Figure 5.4), and this could be due to ripening of InP core during shell formation resulting from high shell growth temperature. Although the 1-hexanethiol has lower normal boiling point (150-160 °C) than the shell formation temperature, the high-pressure system allowed for the use of it, and opened up the usage of precursors that are not usable in conventional batch synthesis.

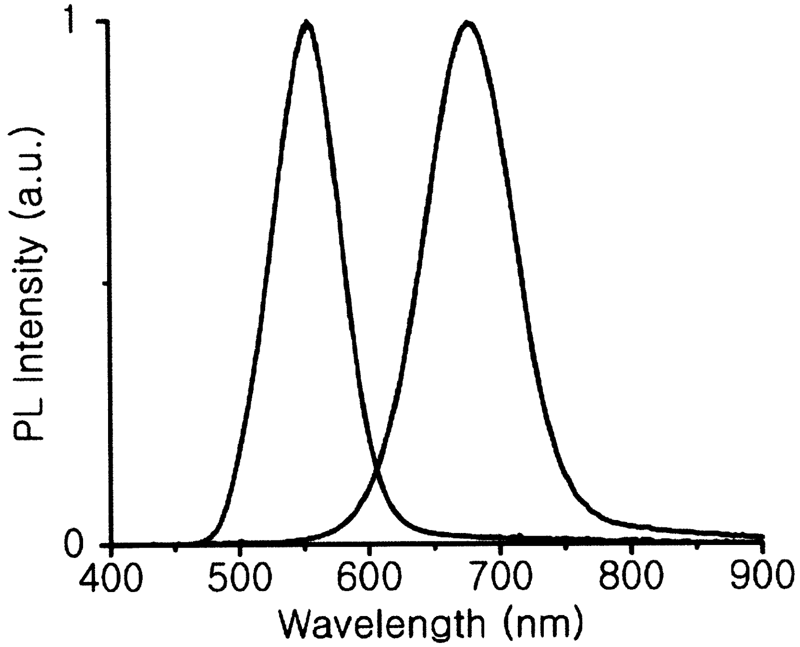

Figure 5.4: Normalized photoluminescence spectra of InP / ZnS core-shell nanocrystals synthesized with thiols.

5.4. Synthesis of InP / ZnSe core-shell QDs

Instead of injecting sulfur monomer precursor for the synthesis of ZnS shell formation, selenium monomer precursor was injected to form a zinc selenide (ZnSe) shell. The three-stage microfluidic system was used to control the core-size (mixing, aging and sequential injection), and following two-stage system (sequential injection and annealing reactor) was used for the ZnSe shell formation. The shell formation temperature was at 280 °C and the residence time was 4 - 4.5 minutes.

Figure 5.5 is the photoluminescence spectra from different InP / ZnSe core-shell nanocrystals. The emissions were tunable from 560 nm to 647 nm. Resulting PL QY were ranging from 35% to 45%, showing 5 – 10 % higher than InP / ZnS core-shell nanocrystals. This higher quantum yield could be owing to the better lattice mismatch between InP core and ZnSe shell (2.7 %) than between InP core and ZnS shell (7.3 %).

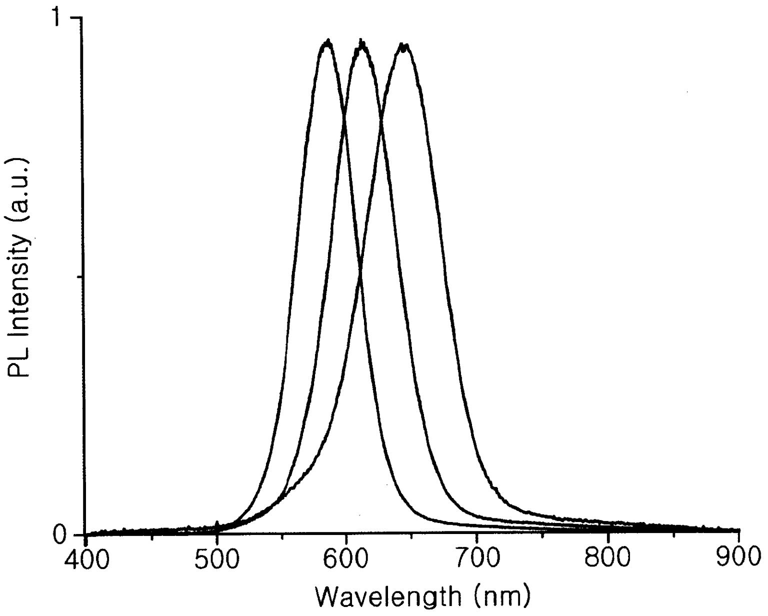

Figure 5.5: Normalized photoluminescence spectra of InP / ZnSe core-shell nanocrystals.

Figure 5.6 is wide-angle X-ray diffraction patterns from InP and InP / ZnSe core-shell QDs. We were able to observe a little shift in the XRD peaks after ZnSe shell formation as well as fade of the InP peak at 30.4 degree. However, the shift of the main peaks was not significant, indicating that the shell thickness is very thin.

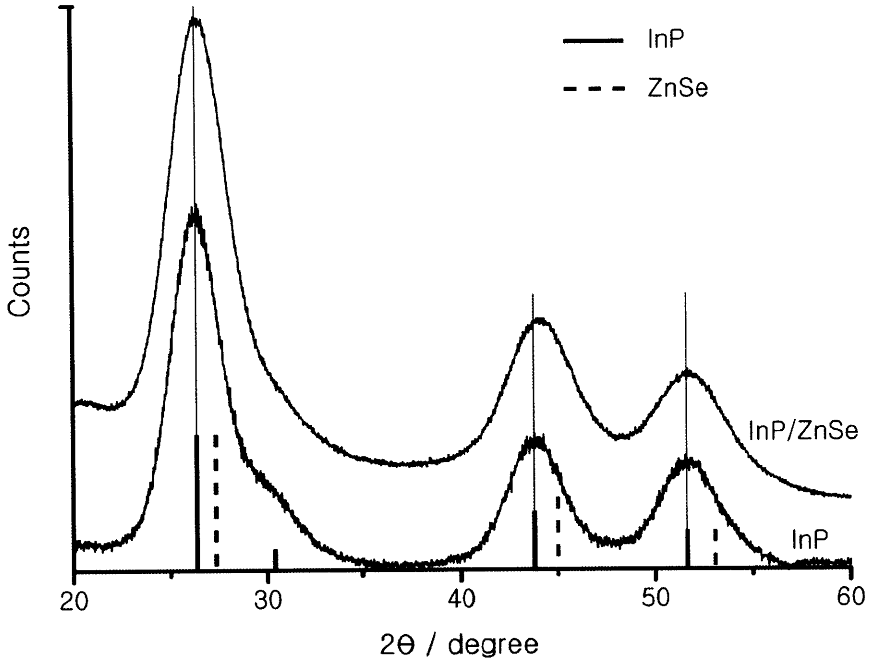

Figure 5.6: WAXS patterns of InP and InP / ZnSe QDs.

Figure 5.7 is TEM images of two different InP / ZnSe core-shell QDs. The sizes of core-shell QDs emitting at 582 nm and 690 nm were 3.2 nm and 4.5 nm in diameter respectively. However, these InP / ZnSe QDs had poorer stability than InP / ZnS QDs. The InP / ZnSe core-shell QDs lost the emissions after ligand exchange with 3-mercaptopropionic acid. Therefore, we would need further investigation on the synthesis of InP / ZnSe QDs in order to make a thicker and more stable ZnSe shell on the InP core, or to understand whether ZnSe would in fact be a suitable shell for protecting the InP core effectively.

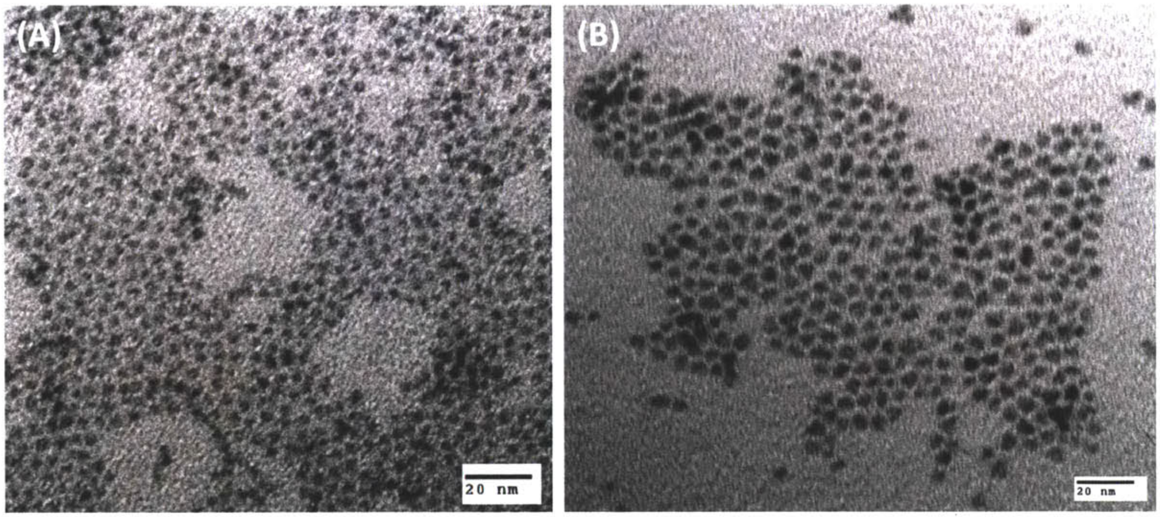

Figure 5.7: TEM images of InP / ZnSe core-shell QDs showing different emissions at (A) 582 nm and (B) 690 nm.

5.5. Application to other structured QDs: InP / CdS and InAs / InP core-shell QDs

The multi-step microfluidic system was also used for other core-shell QD synthesis: indium phosphide / cadmium sulfide (InP / CdS) and indium arsenide / indium phosphide (InAs / InP) core-shell QDs. The multi-stage microfluidic system was also used for another core-shell QD synthesis: indium phosphide / cadmium sulfide (InP / CdS) core-shell QDs.[105] A four-stage system was used: mixing, aging, sequential injection, and annealing. A sequential injection microreactor was used to maintain low concentration of shell precursors, and an annealing reactor was used for the further shell growth. Cadmium oleate ($Cd(OA)_2$) and tri-n-octylphosphine sulfur (TOP-S) were injected into an InP QDs for a CdS shell formation. The amount of TMS_3P used for the InP core synthesis was 0.3 μmol / min (concentration: 30 mM, and flowrate: 10 μl / min), and the amount of each $Cd(OA)_2$ and TMS-S for the shell formation was controlled from 0.2 μmol / min to 1.8 μmol / min. The shell formation temperature was maintained at between 290 °C and 300 °C, and the shell precursors were injected at the sequential injection microreactor. Annealing reactor was maintained at between 280 °C and 330 °C. The concentration of the each shell precursor was 20 mM, and octane was used as the solvent. Detailed conditions were shown in table 5.2.

Table 5.2: Flowrates of the total CdS shell precursors, temperatures at the sequential injection reactor and annealing reactors for InP / CdS core-shell QDs, and the corresponding optical properties.

Photoluminescence Emission Peak (nm)	Total CdS precursor Flow (μl / min)	Temperature at the sequential injection stage (°C)	Temperature at the annealing stage (°C)	FWHM (nm)
608	10	280	280	75
648	20	280	300	74
683	20	290	320	74
702	50	290	320	81
721	70	290	330	84
768	90	290	330	102

In figure 5.8, as the flowrates of the shell precursors increased, the absorbance and photoluminescence peaks shifted to red although the residence time was decreased. We were able to observe prominent emission shifts from 608 nm to 768 nm with a same InP core as CdS shell thicknesses increased. The total residence time for the synthesis of InP / CdS core-shell QDs emitting at 768 nm was less than 4.5 minutes. The photoluminescence peak locations and their FWHMs of those InP / CdS core-shell QDs were shown in table 5.2. As seen in table 5.2, the FWHM of those QDs were as narrow as 75 nm. The seven samples in figure 5.8-(a) corresponded to the each absorption spectrum. This photograph was taken under room light without UV illuminations, and we were able to compare color changes and brightness of the samples. Figure 5.8-(c,d) shows two different InAs / CdS core-shell QDs emitting at 721 nm and 768 nm, and the sizes were 3.1 nm to 4.1 nm respectively. We were able to confirm the QDs with thicker shell emitted at lower energy. However, the sizes of those QDs emitting at lower than 702 nm were too small to be measured accurately.

Since the lattice constants of cubic InP (5.8686 Å) and CdS (5.8320 Å) were very similar, the PL quantum yields of InP / CdS QDs were as high as 50 % (608 nm emitting QDs), which was higher than InP / ZnS QDs. However, we were not able to obtain even higher quantum yields (e.g. almost unity quantum efficiency) that could be found in CdSe / CdS core-shell QDs.[105] This could be because the conduction band energies of InP and CdS were similar. An excited electron in InP core could move to the CdS shell, and the electron could be trapped in defects on the particle surface, potentially decreasing the quantum efficiency. Due to this conduction band energy similarity, InP / CdS QDs behaved pseudo-type-II core-shell QDs. As a result, the red-shifts by the shell formation were more significant compared to InP / ZnS core-shell QDs. For the synthesis of InP / ZnS core-shell QDs, we needed to control the InP core size to control emissions, and we reached up to 691 nm with a large (4.5 nm in diameter) InP core. However, in InP / CdS syntheses, we were able to tune emissions to 768 nm without changing the size of an InP core, and therefore providing a wider emission tuning window. In order to obtain even higher quantum yield of InP / CdS core-shell QDs, it could be necessary to coat the QDs with higher band gap materials such as a ZnS.

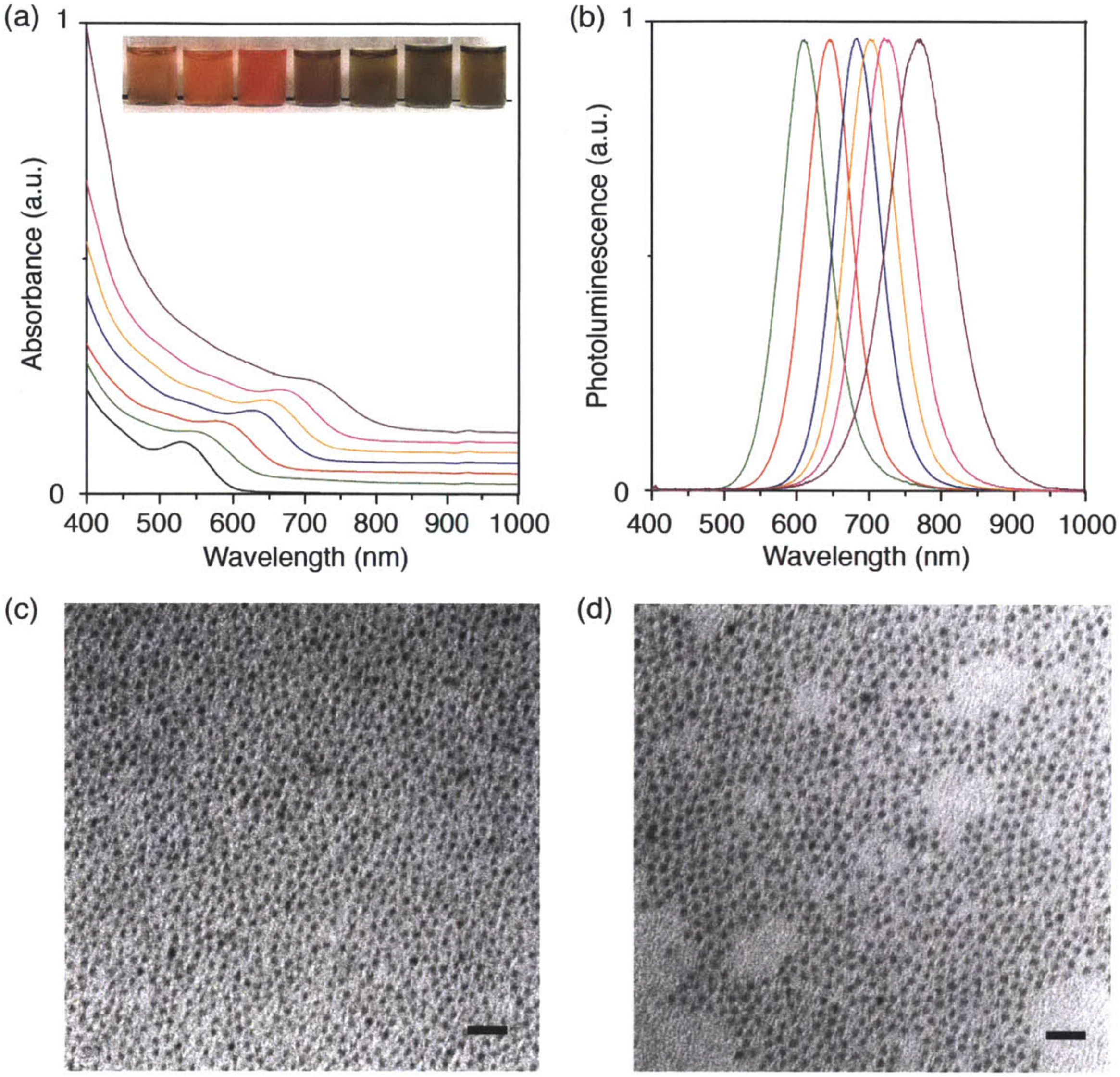

Figure 5.8: (a) Absorbance and (b) photoluminescence spectra of the InP / CdS core-shell nanocrystals. The black line at the absorbance spectra is corresponding to the InP core. Each sample in the photograph (from the left to the right) shown in (a) is corresponding to each absorption spectrum (from the bottom to the top). The emissions are tunable from 608 nm to 768 nm by controlling the CdS shell thickness with an identical InP core. (c) and (d) are TEM images of InP / CdS core-shell QDs emitting 721 nm and 768 nm respectively. The scale bar is corresponding to 20 nm.

Instead of InP core, we also synthesized InAs core by replacing TMS_3P with tristrimethylsilyl arsine (TMS_3As) (figure 5.9). The aging temperature (the second step) was maintained at 290 °C. At the shell formation microreactor, we alternately injected 20 mM $In(MA)_3$ and TMS_3P at 230 °C to form InP shell on InAs core. The detail of the synthesis of InAs core in microflow will be reported later. The emissions were successfully tuned from 680 to 783. Table 5.3 shows the each peak location and FWHM of the emission spectra in figure 5.10. Figure 5.11 is two TEM images of the two different InAs / InP core-shell nanocrystals with identical InAs core and different InP shell thickness. We were able to confirm the InP shell growth also by the size difference. Since the shape of the core-shell nanocrystals are not very uniform, it is hard to estimate the absolute sizes. However, by applying a consistent criterion for the nanocrystal diameter measurements, the diameter of the CS1 is 3 nm (± 0.4 nm) and the CS2 has 4.0 nm (± 0.3 nm). Unfortunately, we were not able to measure the size of the InAs core since the particle sizes were too tiny to be measured with TEM and the particles were easily oxidized (within 10 minutes in dry atmosphere) when those to air.

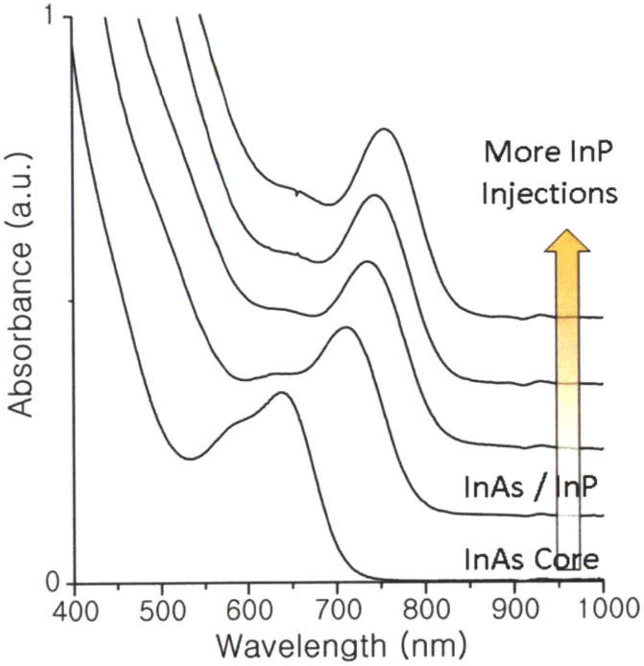

Figure 5.9: Absorbance InAs / InP core-shell nanocrystals with 3-step microfluidic system consisting of mixing, aging, and shell formation microreactors. At the shell formation microreactor, $In(MA)_3$ and TMS_3P was alternately injected into the main channel.

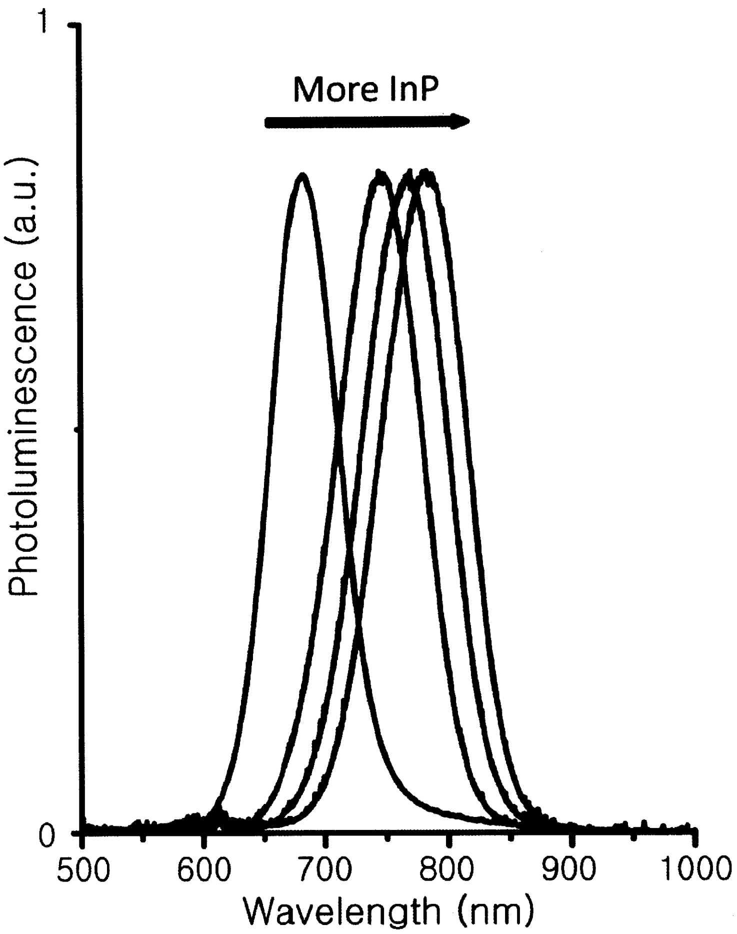

Figure 5.10: Photoluminescence spectra of the InAs / InP core-shell nanocrystals. We were able to tune the emissions from 680 nm to 783 nm.

Table 5.3: The peak locations and FWHMs of the photoluminescence spectra in figure 5.10.

	Core	CS1	CS2	CS3
Peak	680	744	770	783
FWHM	65	79	80	81

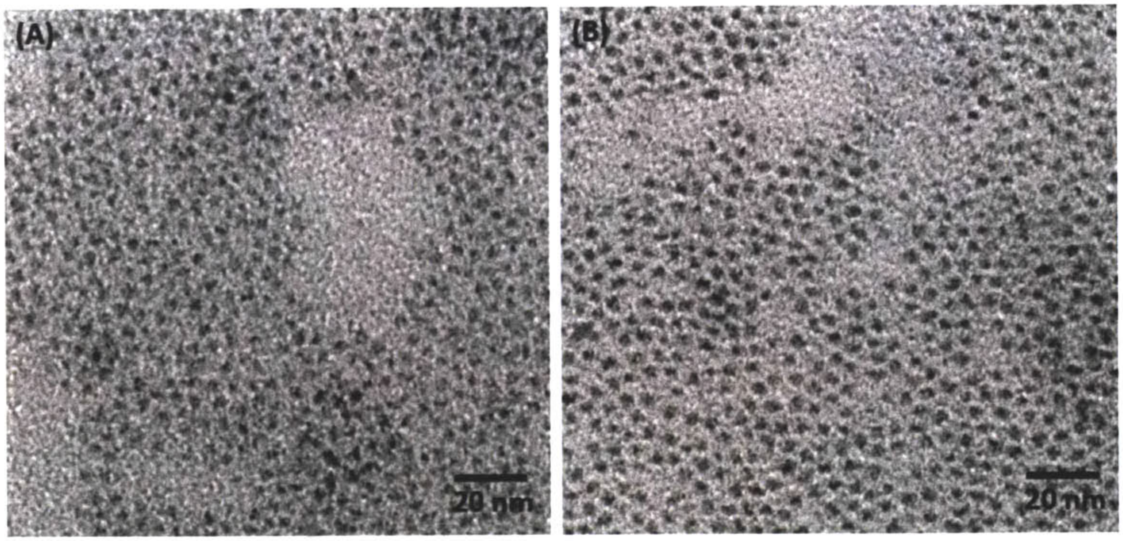

Figure 5.11: TEM images of InAs / InP core-shell structured nanocrystals. (A) is the CS1 showing emission at 744 nm with a size of 3 nm (± 0.4 nm) in diameter, and (B) is the CS3 with a size of 4.0 nm (± 0.3 nm) emitting at 783 nm.

The PL quantum yields of InP / CdS were as high as 50% (605 nm emitting QDs) and those of InAs / InP core-shell QDs were increasing up to 35 % by the surface passivation with high band-gap shell materials, although the quantum yield of the bare InAs core is typically less than 10%. InAs / InP core-shell QDs showed redder emissions than InP / ZnS or InP / CdS core-shell QDs at the near infra-red, could potentially be better material for near infra-red applications.

5.6. Summary

In conclusion, we have designed a multi-step microfluidic system operating at high pressure and high temperature for the synthesis of InP / ZnS core-shell QDs. The multi-step microfluidic system combined with an in-line measurement device allowed for precise and improved control of reaction parameters at each synthetic step, and provided continuous synthesis of structured nanoparticles such as the core-shell type. The high pressure and high temperature conditions enabled the use of low-molecular-weight solvents which enhanced the mixing in the system, resulting in a narrow size distribution of InP QDs as well as allowing the usage of precursors, which were difficult to use in conventional batch synthesis systems. We overcoated a ZnS shell on InP QD cores without incorporating any batch procedures between steps, and the resulting InP / ZnS core-shell QDs showed tunable emissions from visible to near-infra-red with FWHMs as narrow as 175 meV. This multi-step platform was also applied to the other types of structured QDs such as InP / CdS and InAs / InP core-shell QDs. This work could form the basis for continuous synthesis of high quality structured nanoparticles with improved step-by-step controls.

Chapter 6

Indium Arsenide Phosphide Alloy Synthesis

6.1. Introduction

Semiconductor nanocrystals[67, 77, 106],so called quantum dots (QDs), are attractive due to their size dependent properties. Tunable emissions allow for potential usage in displays or photovoltaics, as well as bio-imaging.[45, 49, 60] III-V semiconductor nanocrystals[16, 18, 66, 73, 103, 107] are of interest because of their excellent optical and electronic properties as well as relatively lower toxicity than II-VI materials that incorporate cadmium, lead or mercury. However, synthesis of III-V QDs is challenging, and the level of understanding on those particle growth has not reached to the sophisticated level of II-VI QDs. Furthermore, although some of II-VI QDs such as CdSeS[108-110] or CdZnSe[111] are known to form alloy compound at nano-scale sizes, alloy formation of III-V materials is still an open question.[90]

Indium phosphide arsenide (InP_xAs_{1-x}) alloy quantum dots provided controlled emissions from visible to near-infra-red as III-V semiconductor materials. Although pure InAs or InP nanocrystals[9, 14, 65-66] could be used for near-infra-red emitters, these materials that could access the near-infra-red are limited to the larger (> 6 nm) InP QDs, for which a robust synthesis is limited, or smaller InAs (< 2 nm) QDs that have an absorbance lower than desired. For various applications such as bio-imaging, larger absorption cross sections are always better. InP_xAs_{1-x} quantum dots could overcome these limitations for practical applications.

Precise temperature control and fast heating up after mixing of the two precursors are very important for the InP_xAs_{1-x} synthesis. Since thermal stability of two precursors, $(TMS)_3P$ and $(TMS)_3As$, are poor, it is observed that those materials decompose at an elevated temperature as low as or lower than 180 °C. Therefore, $In(MA)_3$ needs to be mixed with those precursors at low temperature. However, the desired growth temperature of both InP and InAs QDs is as high as 300 °C. Because InAs QDs tend to grow at lower temperature than InP QDs, slow heating up would promote first growth of InAs QDs instead of alloy compound formation. In order to minimize the growth selectivity between InP and InAs, hot temperature growth conditions (eg. above 300 °C) are desired. In traditional batch synthesis,[25-26, 66] obtaining fast heating up with precise temperature control is very difficult, and typically, controllable heating up time in batch synthesis is longer than 10 – 30 minutes. Furthermore, in batch system, precise composition control of phosphorus and arsenic with a fixed residence time, which is critical for the investigation of alloy compound, is challenging.

Microreactor systems[5, 7] provide a large surface-to-volume ratio, and enable fast heating up with precise temperature control. The excellent controllability in flow and temperature is essential for the study of III-V alloy QD synthesis.[9] Utilization of supercritical solvent[21] provides excellent mixing and homogeneous reaction condition in microreactors. This homogeneous reaction approach is important for particle synthesis that incorporates fast reaction such as InP or InAs synthesis, and thus it is also important for InP_xAs_{1-x} alloy nanocrystal synthesis. An in-line UV-Vis device connected to the outlet of the microreactor system and capable of operating at high pressure (>80 bar) allows fast screening of reaction conditions.[6, 8]

6.2. Methods: system and operation

Figure 6.1 illustrates a two-stage high-temperature, high-pressure microfluidic system consisting of a heating stage and an aging stage operating at 68 Bar. We generated temperature gradient in the heating stage by heating the top of the microreactor. Tris(trimethylsilyl) phosphine (($(TMS)_3P$) and tris(trimethylsilyl) arsine [$(TMS)_3As$] in octane, each at a concentration of 30 mM, were mixed in a micro-mixer. The resulting mixture contacted indium myristate ($In(MA)_3$) in a 1:1 flow ratio in the heating stage at 120 °C. The solution was continuously heated up to 280 °C within 1.5 minutes. The concentration of $In(MA)_3$ was 90 mM, and therefore, the amount $In(MA)_3$ to the mixture of $(TMS)_3As$ and $(TMS)_3P$ was always maintained at 3. We varied the flow ratio of $(TMS)_3As$ to $(TMS)_3P$ in three steps: 2, 1, and 0.5. The total flowrate of the mixture was always kept at 30 µl / min.

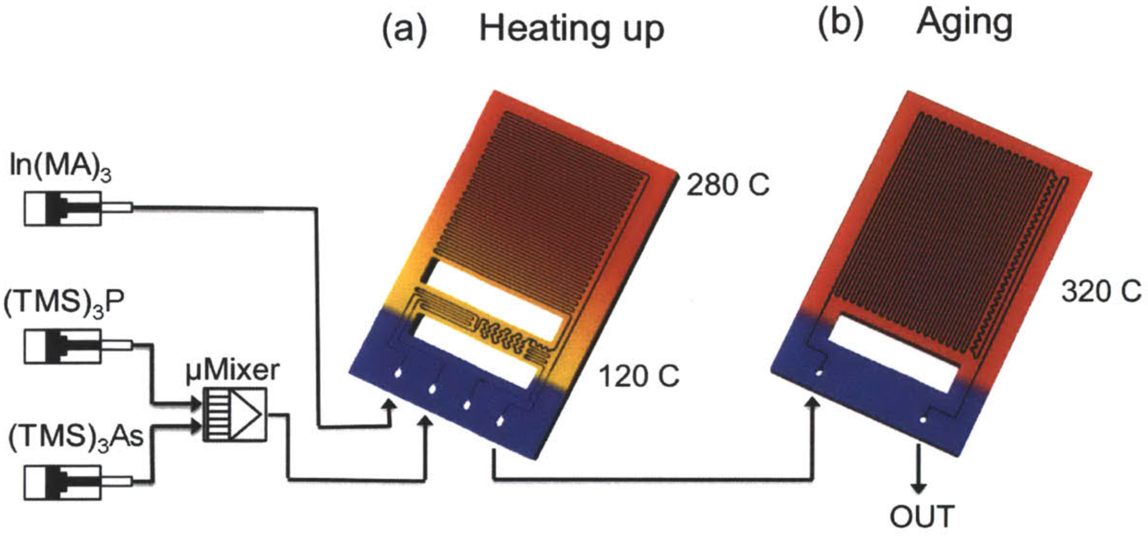

Figure 6.1: Two-stage microfluidic system operating at high-pressure and high-temperature. $(TMS)_3P$ and $(TMS)_3As$ is pre-mixed with micro-mixer, and flows into (a) a heating up stage. The mixture of $(TMS)_3P$ and $(TMS)_3As$ is mixed with $In(MA)_3$ at 120 °C, and heated up to 280 °C within 1.5 minutes. In order to realize this fast heat-up process, gradient temperature was used. The product is continuously transferred to (b) an aging stage at 320 °C for further growth for 2.5 minutes.

After the fast heat up in 1.5 min from 120 °C to 280 °C, the solution was transferred to the second step, the aging reactor, without any batch manipulations between the steps. The temperature of this reactor was maintained at 320 °C, and the residence time was 2.5 minutes. This reactor was maintained at such a high temperature since the particle growth could be by an inter-particle process. Assuming that energy barrier of the inter-particle growth of InP and InAs could be different, high temperature could be a solution to minimize the energy barrier difference, and promote to form alloy nanocrystals. At this temperature, octane (T_c=296.17 °C and P_C=2.50 MPa) as the solvent, forms supercritical phase, providing fast diffusivity of the solutes. The improved mixing allowed for the alloy nanocrystal production in 3.5 minutes, or less.

6.3. Results

6.3.1. Optical characterization

Figure 6.2 is (a) absorbance and (b) photoluminescence spectra of InP_xAs_{1-x} quantum dots. We precisely controlled the amount of the two group-V precursors: $(TMS)_3P$ and $(TMS)_3As$. The first absorption peak was shifted from 521 nm to 673 nm as the amount of $(TMS)_3As$ increased. Each of the first absorption peak was located at 521nm (InP), 536nm ($InP_{0.6}As_{0.4}$), 547nm ($InP_{0.5}As_{0.5}$), 578 nm ($InP_{0.3}As_{0.7}$), and 673 nm (InAs). The corresponding photoluminescence peaks were also measured (Figure 6.2-(b)). However, since the InP QDs have very low quantum efficiency, we only were able to observe emissions from $InP_{0.5}As_{0.5}$, $InP_{0.3}As_{0.7}$, and InAs QDs.

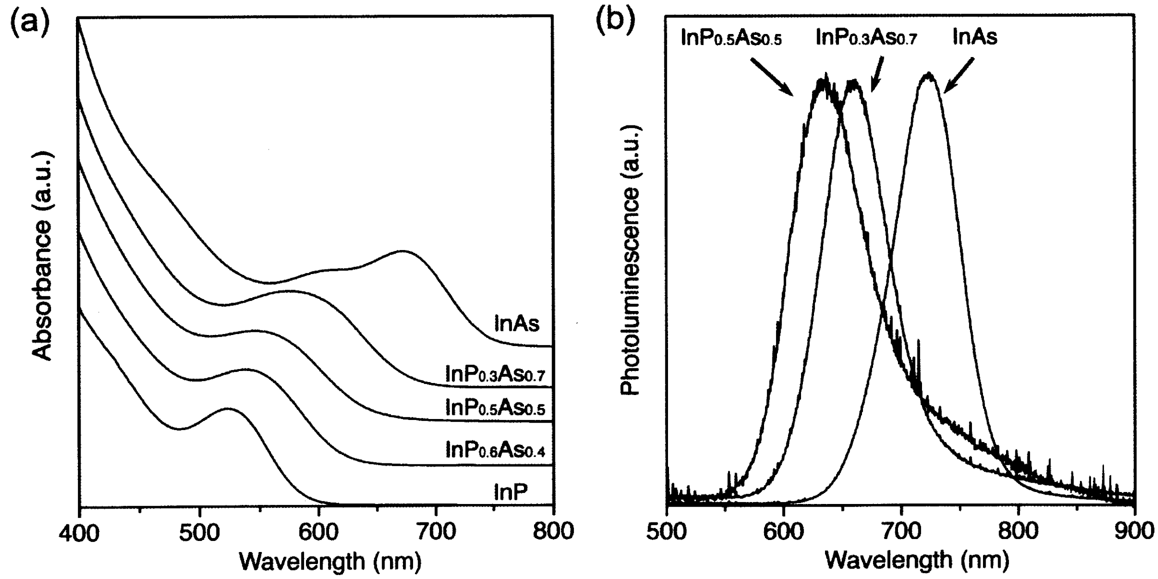

Figure 6.2: (a) Absorption and (b) photoluminescence spectra of InP_xAs_{1-x} alloy QDs.

6.3.2. XRD and WDS characterization

The crystal structures of those ally particles were measured by wide-angle X-ray scattering (WAXS). In figure 6.3, The peaks corresponding (111), (220), and (311) lattice planes of pure InP were exactly matched with references. As the $(TMS)_3As$ amount increases, all the peaks were gradually shifted to high angles, indicating that the lattice constant increased. These gradual changes in lattice constant, in addition to the peak shifts of the first absorption spectra, indicate InP_xAs_{1-x} alloy formation. The composition of each alloy compound was measured by wavelength dispersive spectroscopy (table 6.1). This composition data is also an indicative that shows the successful and controllable incorporation of phosphorus and arsenic in the alloy QDs. The actual ratios between $(TMS)_3P$ and $(TMS)_3As$ were 1.52, 0.95, and 0.39, although the injection amount ratios were set to 2, 1, and 0.5. In general, $(TMS)_3As$ was slightly more incorporated in the alloy nanocrystals than the $(TMS)_3P$.

Table 6.1: Compositions of the InP_xAs_{1-x} alloy QDs measured by WDS.

Sample	$InP_{0.6}As_{0.4}$	$InP_{0.5}As_{0.5}$	$InP_{0.3}As_{0.7}$	InAs
Indium (atomic %)	59.7 (±5.1)	54.2 (±5.0)	58.1 (±3.9)	54.1 (±5.1)
Phosphorus (atomic %)	24.3 (±4.6)	22.3 (±2.6)	11.8 (±1.1)	0.3 (±0.06)
Arsenic (atomic %)	16.0 (±3.1)	23.6 (±3.7)	30.1 (±3.6)	45.6 (±3.5)
Ratio P to As	1.52	0.95	0.39	0.01

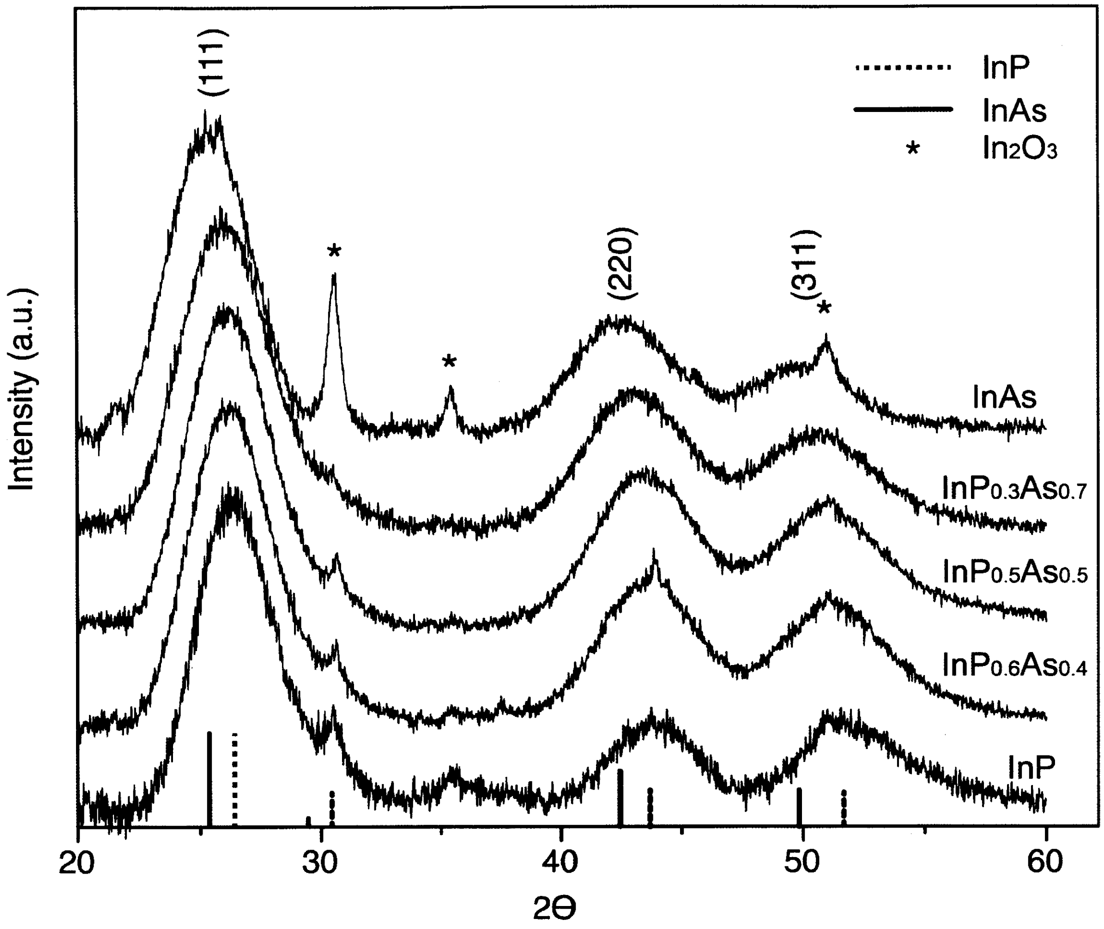

Figure 6.3: WAXS patterns of InP_xAx_{1-x} QDs. The peaks marked with * are from indium oxide.

6.4. InP_xAs_{1-x} / ZnS core-shell nanocrystals

Since the multi-step microfluidic system allows for the synthesis of structured nanocrystals, we connected two additional steps to the two-step alloy nanocrystal system. This four-stage system allowed for the synthesis of InP_xAs_{1-x} / ZnS core-shell QDs. Figure 6.4 shows the absorption spectra and photoluminescence spectra of those QDs with different group-V material compositions. The photoluminescence intensity increased due to the surface passivation by a ZnS shell, a high band-gap material. We were able to observe tunable emissions with narrow FWHMs. The quantum efficiency of the InP / ZnS core-shell QDs were as high as 35%. However, since it is very difficult to overcoat pure InAs with ZnS, the quantum yield enhancement of InAs / ZnS core-shell QDs from the bare InAs cores was not significant.

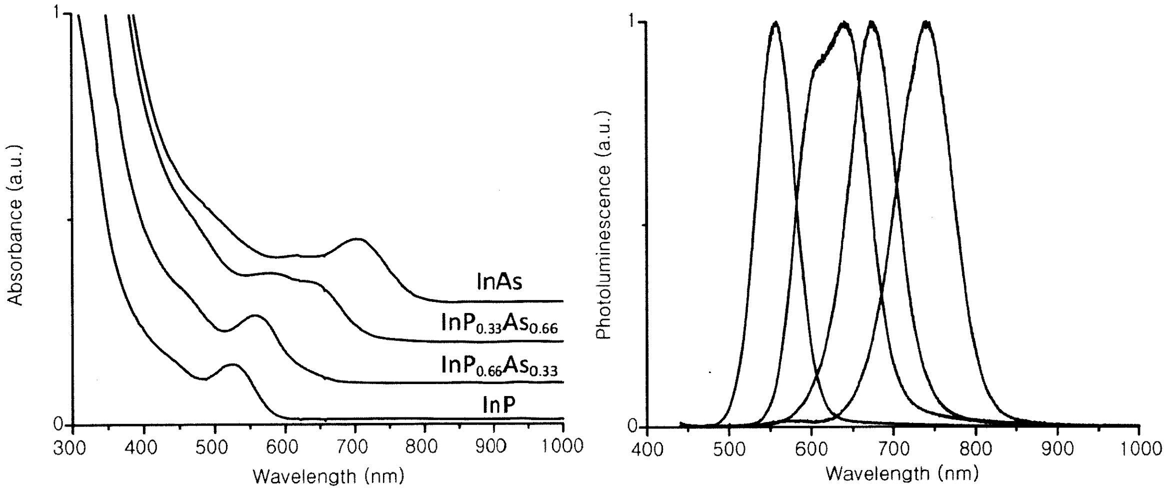

Figure 6.4: (a) absorbance and (b) photoluminescence spectra of InP_xAs_{1-x} / ZnS core-shell QDs

We observed bimodal emissions from $InP_{0.66}As_{0.33}$ / ZnS core-shell nanocrystals although the corresponding absorption spectrum was unimodal. Each of the two peak locations are different from either InP / ZnS or InAs / ZnS core-shell nanocrystals. Therefore, the bimodal emission could be due to either a broad size (diameter) or a composition (P / As) distribution of $InP_{0.66}As_{0.33}$ alloy nanocrystals.

6.5. Summary

To summarize, we successfully synthesized InP_xAs_{1-x} alloy compound using high-pressure and high-temperature microfluidic system with a mixing reactor with temperature gradient. This microfluidic system with temperature gradient allowed for the controlled synthesis of III-V alloy compound in a short residence time. These alloy compounds could have superior properties to pure InP or InAs QDs, especially for near-infra-red applications. This microfluidic system could potentially be also applied for other ally compound synthesis such as $InAs_xSb_{1-x}$ or InP_xSb_{1-x}. We also successfully synthesized the InP_xAs_{1-x} / ZnS alloy core and shell QDs. The emissions were tunable from visible to near infra-red (NIR). However finding a good shell material for both InP and InAs passivation remains a challenge.

Chapter 7

Investigation of the Indium Arsenide Growth from Different Arsenic Monomers: tris(trimethylsilyl)arsine (TMS_3As) vs tris(trimethylgermyl)arsine (TMG_3As)

7.1. Introduction

Investigation of the growth of III-V quantum dots has been of interest due to increasing demand for less toxic materials such as InP, or for near infra-red applications with InAs or InSb.[15, 17, 65-66, 91] However, the understanding and quality of synthesis for III-V quantum dots has not reached the level of the II-VI or IV-VI quantum dot synthesis. Moreover, the growth behavior of III-V quantum dots appears to be different from the growth of II-VI quantum dots,[9, 65, 83] as would be explained from the different of material properties of II-VI and III-V quantum dot systems. For example, the bonding in III-V materials is more covalent. Another main reasons could be different reactivity of the monomer precursors for nanocrystal synthesis.[65, 83]

It has been known that the reaction in III-V nanocrystal synthesis is typically so fast that all the monomer precursors are depleted quickly after anion precursor injections to cationic precursors at elevated temperature. Therefore, the fast initial reaction pricludes particle size focusing[70, 77, 112] that is induced by continuous monomer supply during particle growth. Commonly precursors for II-VI or IV-VI nanocrystal synthesis such as cadmium oleate ($Cd(OA)_2$), zinc oleate ($Zn(OA)_2$), tri-n-butyl phosphine selenide (TBPSe), or tri-n-octylphosphine sulfide (TOPS) have low reactivity. As a result, those II-VI or IV-VI group nanocrystals such as CdSe, CdS, PbSe, or PbS showed better size distribution than III-V semiconductor nanocrystals such as InP.

The fast monomer depletion observed in III-V nanoparticle synthesis is mostly owing to the highly reactive anionic precursor such as tristrimetylsilyl phosphine (TMS_3P) or tristrimethylsilyl arsine (TMS_3As). By decreasing the reactivity of these anionic precursors, we could expect to observe nanocrystal size focusing behavior by continuous monomer supply during the reaction. Some groups tried to use tris(tert-butyldimethylsilyl)phosphine, which has lower reactivity than TMS_3P, to synthesize InP, and they reported that they were able to obtain better size distribution.[113]

In our work, we synthesized tris(trimethylgermyl) arsenide TMG_3As, which is less reactive than TMS_3As, and investigated InAs growth from this precursor. Daniel Harris (Materials Science department, MIT) synthesized TMG_3As from chlorotrimethylgermane and tris(trimethylsilyl)arsine. In order to control concentration and temperature precisely, we used two-stage microfluidic system operating at 65 Bar.

7.2. Methods

7.2.1. System description

We systematically investigated the effect of anionic precursor reactivity on the InAs nanocrystal growth. We utilized two-stage microfluidic system. Since the monomer depletion rate at elevated temperature is very fast (we speculate that it takes only less than several second above 150 °C), and potentially wall deposition may occur, we designed jet-shaped mixing microreactor (figure 7.1). $In(MA)_3$ is divided into two streams (each channel has 100 μm in width) at cold regime and pre-heated prior to be mixed with the arsenic precursor, TMS_3As or TMG_3As. The arsenic precursor is flowing through a channel (80 μm in width), and also pre-heated before the mixing. Two indium precursors are flowing on the side wall to protect any potential InAs deposition, and arsenic precursors are flowing at the center.

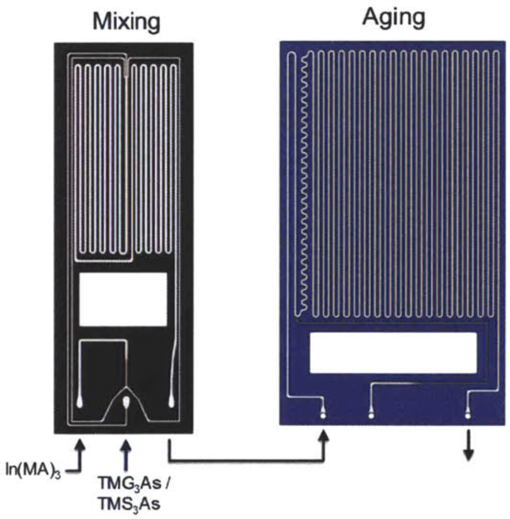

Figure 7.1: Two-stage system for InAs synthesis from two different arsenic sources: TMS_3As and TMG_3As. Jet-shape microreactor was used as a mixing reactor to prevent any potential side effects such as wall deposition since the monomer reaction rate is very fast.

7.2.2 Precursor solution preparation and system operation

Indium myristate (In(MA)$_3$) was dissolved in octane containing 4.5 vol % tri-n-octylphosphine (TOP). TMS$_3$As or TMG$_3$As was dissolved in octane without TOP. Concentrations of In(MA)$_3$ solution was 45 mM, and TMS$_3$As or TMG$_3$As had 30 mM concentration. Those precursors are mixed with a 2:1 ratio between In and As. The residence time was 2 minutes at the first mixing stage, and was approximately 2.5 minutes at the aging stage. The residence time at the aging reactor slightly varied due to the solvent density change as different temperatures.

7.3. Results

7.3.1. Effect of aging temperature

By utilizing two-stage microfluidic system, we investigated aging temperature effect of the InAs nanocrystals grown from two different arsenic monomer precursors. The mixing temperature was fixed at 150 °C. Figure 7.2 shows aging temperature effect on InAs nanocrystals. InAs nanocrystals synthesized from TMG_3As shows better first absorption spectra. Above 220 °C at the aging stage, the first absorption peak from TMS_3As was continuously shifted to longer wavelength. On the contrary, the first absorption peak from InAs nanocrystals synthesized from TMG_3As shifted to blue regime as a temperature increase above 220 °C at the aging stage, indicating that there could be some different behavior other than inter-particle process occurs such as growth by continuous monomer supply.

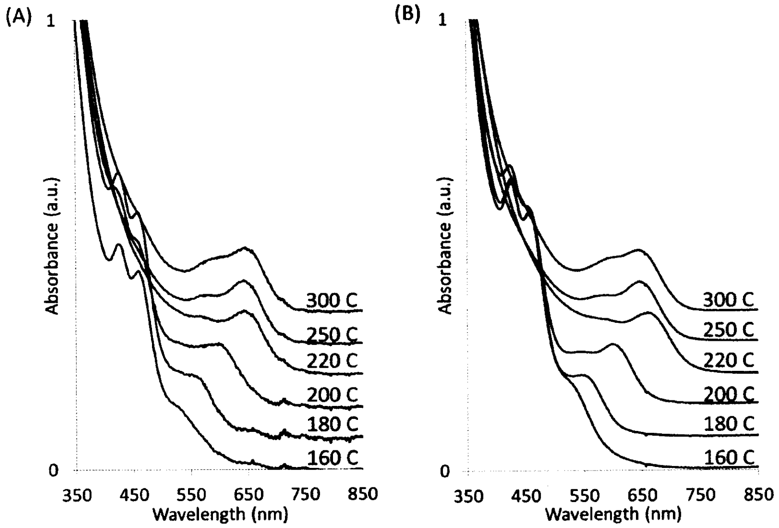

Figure 7.2: Absorbance spectra of InAs quantum dots synthesized from a) TMS_3As and b) TMG_3As. InAs nanocrystals are synthesized with two-stage microreactor system with a fixed mixing temperature at 150 °C and a variety of aging temperatures. All the other conditions such as concentration, residence time, system pressure, and solvent were identical.

We speculate that TMG_3As monomer precursor could show growth behavior by the continuous monomer supply during the growth. This could be because TMG_3As has lower reactivity than TMS_3As. If the monomer precursors are not depleted at the early stage of the nanocrystal synthesis, we may observe a behavior similar to the nucleation and growth model.[26, 70, 77] In order to observe a process similar to nucleation, we also need to investigate temperature effect on the mixing stage.

7.3.2. Effect of mixing temperature

Since we observed different phenomena from the absorbance spectra of InAs synthesized from TMS_3As and TMG_3As, we investigated effect of mixing temperatures. In order to observe more significant effect of different mixing temperature, and detect a growth behavior by continuous monomer supply, we decreased aging temperatures to 210 °C. This is because inter-particle process also could be very significant at high aging temperature, and therefore the observation of the growth behavior could be obstructed.

Figure 7.3 shows absorption spectra of InAs nanocrystals synthesized from different arsenic precursors (TMS_3As and TMG_3As) at different mixing temperatures (110 °C, 130 °C, 145 °C, and 160 °C) and a fixed aging temperature (210 °C). The concentration of the $In(MA)_3$ was 45 mM, and $In(MA)_3$ was mixed with arsine precursors, with a ratio of 3. 30 mM TMS_3As or TMG_3As dissolved in octane was used as the arsine precursors. Although it was possible to run experiment at an identical condition for both precursors, preparing the precursors with an identical concentration was difficult. We carefully prepared the two precursor solutions, and the concentrations were precisely confirmed by NMR analysis (done by Daniel Harris).

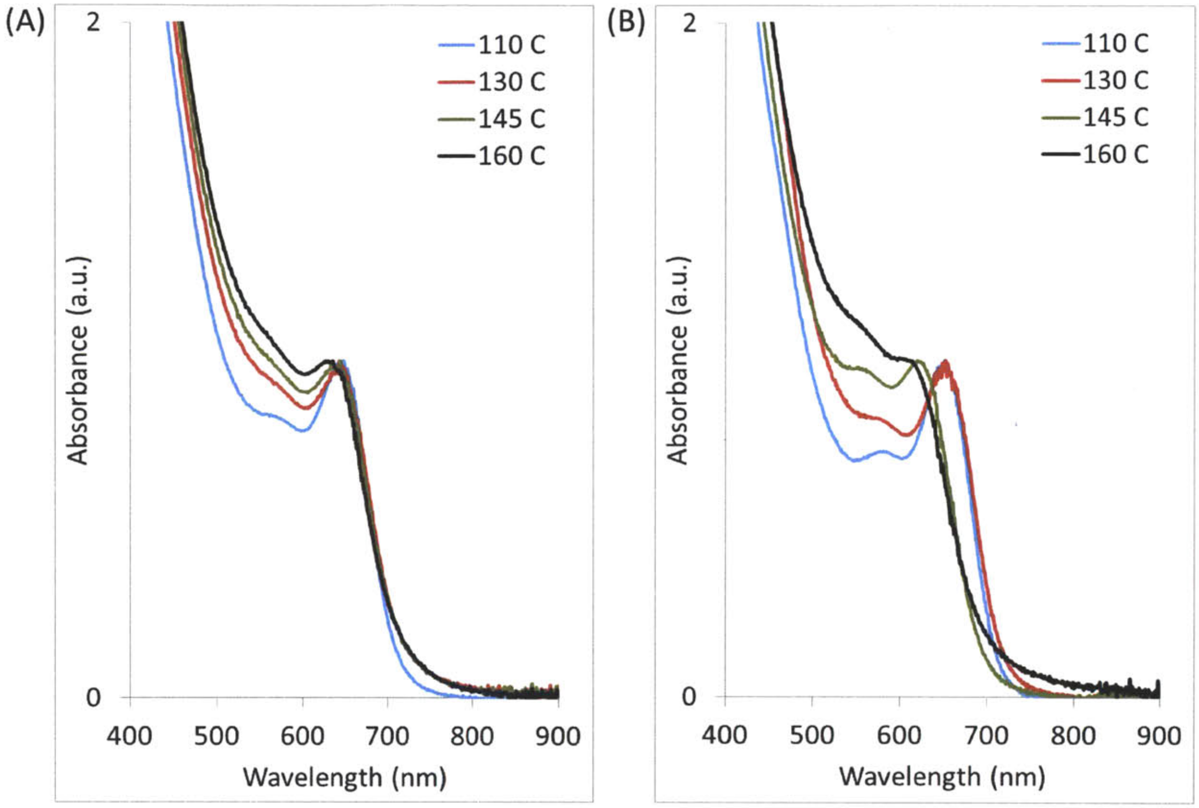

Figure 7.3: Absorbance spectra of InAs quantum dots synthesized from different arsenic sources: a) TMS_3As and b) TMG_3As. Two-stage microreactor system was used for the synthesis. The mixing temperature was changed from 110 °C to 160 °C, and the aging temperature was fixed at 210 °C. All the other conditions such as concentration, residence time, system pressure, and solvent were identical.

We were able to find the more pronounce blue shift of the first absorption feature from the TMG_3As case as the mixing stage temperature increase. This could be because the reaction between $In(MA)_3$ and TMG_3As is not as fast as the reaction between $In(MA)_3$ and TMS_3As, and therefore, the number of the InAs nuclei could be less. Unreacted arsenic monomers (TMG_3As) could further react with $In(MA)_3$ during particle growth and grow on the top the existing InAs nuclei or particles.

Figure 7.4 is the photoluminescence spectra of the InAs nanocrystals. Since less reactive arsenic precursor, TMG_3As, could extend the time for the monomer supply during the particle formation, the particle size focusing behavior by continuous monomer supply during the particle growth also could happen. This results in sharper first absorption spectra and narrow FWHM of the photoluminescence (Figure 7.4).

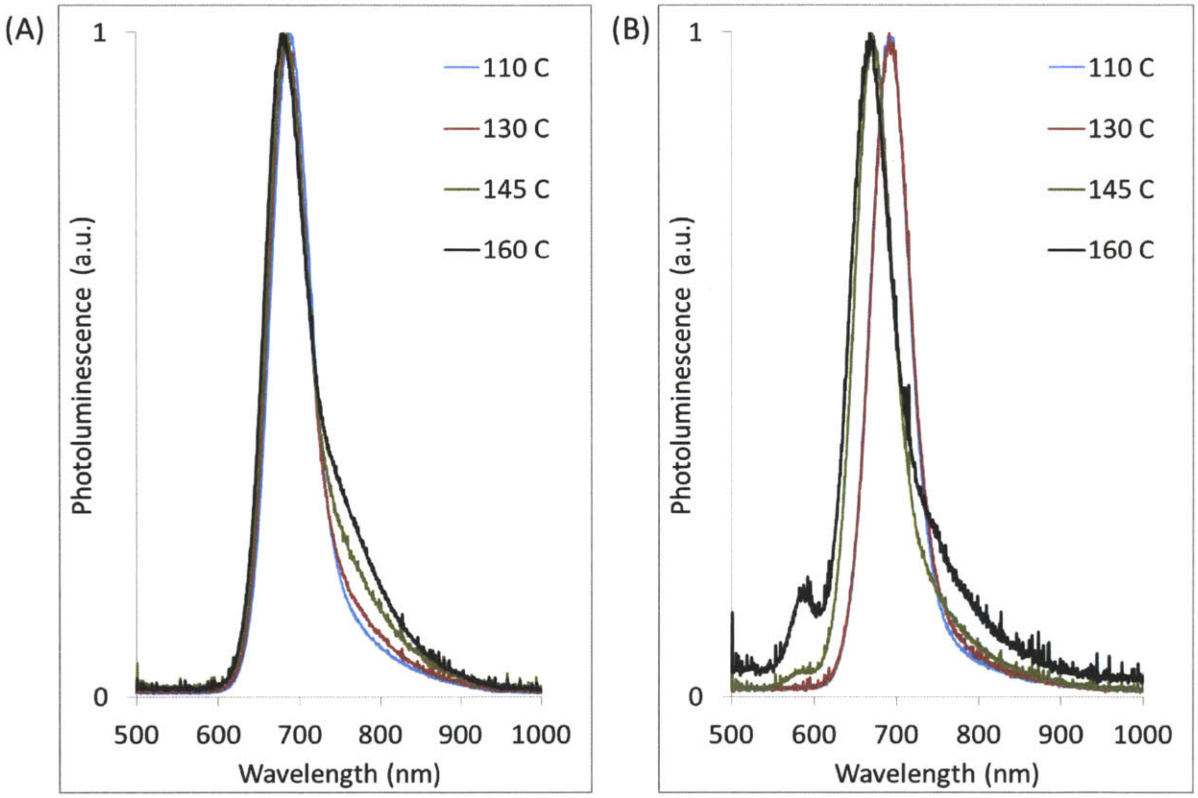

Figure 7.4: Photoluminescence spectra of InAs quantum dots shown in figure 7.3.

However, measurement of the total number of the InAs in the nanocrystals or the number of nanocrystal concentration provides better understanding of the growth. Unfortunately, direct measurement of the number of nanocrystals is difficult. Instead of a direct measurement of particle concentrations, absorption spectra at short wavelength (approximately 300 – 400 nm) provide estimation of the reaction yields. Figure 7.5 shows all the absorption spectra normalized with intensities of the each first absorption peak (the original data are the same as figure 7.4). From the short wavelengths regime between 350 nm and 400 nm, the reaction yields are similar for all the eight cases. Small differences in the absorption intensities at this regime are within measurement errors. Measurement of size dependent extinction coefficient at the first absorption peak could be useful to measure reaction yield more exactly. However, since the size difference of InAs diameters synthesized from those eight conditions is within 0.15 nm in diameter, and therefore, the extinction coefficient differences for those eight InAs nanocrystals could be still within measurement error.

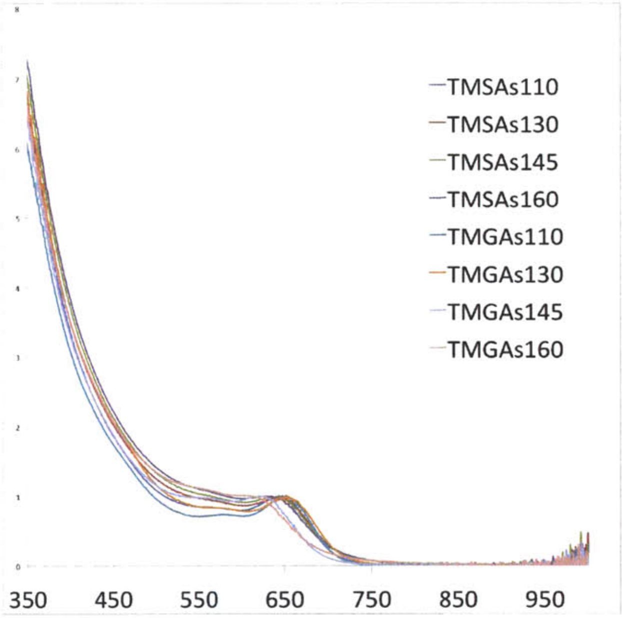

Figure 7.5: Overlap of all the absorption spectra shown in figure 7.3.

7.3.3. Growth by sequential injections

In Chapter 4, we showed InAs growth via sequential injections, and we were able to tune the sizes of the InAs nanocrystals. In this chapter, we found that TMG_3As monomer precursor showed better shape of the first absorption feature, indicating that the resulting InAs nanocrystals were more monodisperse than the nanocrystals from TMS_3As precursor. Nanocrystals with narrower size distribution is a better starting point for the larger nanocrystal synthesis with narrow size distribution.

In order to perform the sequential injection process, the monomers need to have such a fast reactivity that all the monomers need to be consumed in a short residence time (approximately ten seconds) at high reaction temperature. Presumably, both TMG_3As and TMS_3As are satisfying this condition. However, in order to promote size focusing during the growth, the arsenic monomer needs to have such a low reactivity that the monomers can continue to react and add to existing nuclei throughout the residence time.

Since the reactivity of TMG_3As is lower than TMS_3As, we were able to obtain better result from the sequential growth (figure 7.5). The first absorption spectra were sharper than the result from TMS_3As, indicating that the TMG_3As could help to focus nanocrystal size distribution during the sequential injection process.

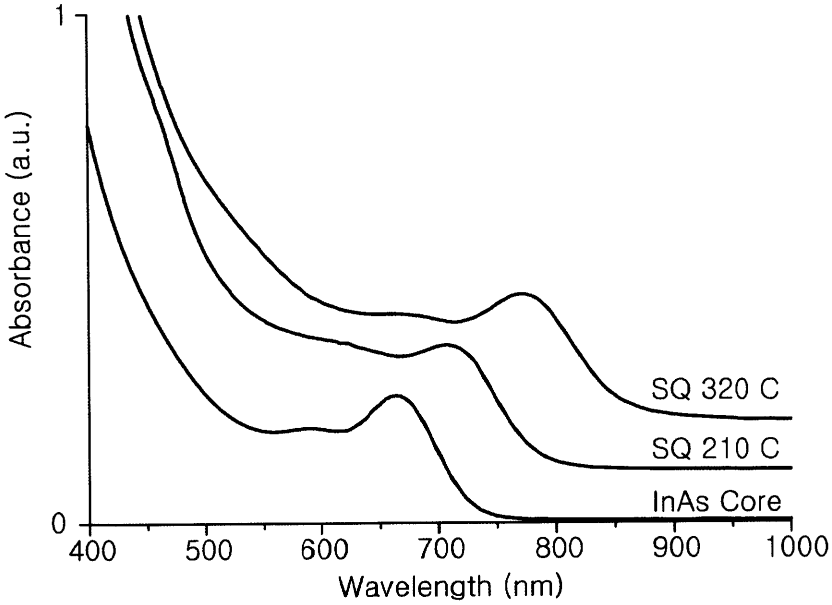

Figure 7.5: InAs nanocrystal growth via sequential injection. TMG_3As was used as the arsenic source.

Chapter 8

Summary and Future Opportunities

8.1. Summary

A microfluidic reactor system provides several advantages over conventional batch systems including fast heat and mass transfer, improved control, lower reagent consumption during optimization, and in-situ reaction monitoring. High-pressure and high-temperature conditions expand the reaction space by allowing the use of solvents, reactants and ligands that are not easily used in batch systems. We have developed a continuous multi-stage microfluidic system operating at high-pressure and high-temperature for the systematic study of III-V quantum dot growth, in particular InP and InAs nanocrystals. This multi-stage system was also used for core-shell structured quantum dot syntheses of InP / ZnS, InP / CdS, InAs / InP, and InAs / CdS. We have designed a shell formation microreactor with 6 or 10 side-channels. This special design allowed maintaining a low concentration of the injected materials and suppressing undesired particle formation. By generating a temperature gradient, we were able to improve the production of nanocrystals, and synthesize InP_xAs_{1-x} alloy quantum dots. We also studied InAs growth with tristrimethylgermyl arsine (TMG_3As), a less reactive arsenic compound than the more common, tristrimethylsilyl arsine (TMS_3As). We were able to observe InAs nanoparticle growth attributed to monomer precursors, and obtained InAs nanocrystals with a better size distribution than those from TMS_3As as the arsenic precursor. The results suggest that a multi-stage microfluidic system is a useful tool for the synthesis of new materials as well as complex nanostructures.

8.2. Future Opportunity

8.2.1. Novel nitride nanocrystal synthesis (InN)

Nitride materials such as indium nitride (InN) or gallium nitride (GaN) have been very intriguing due to their unique properties including band gap and stability.[114] Promising nitride-based quantum dots such as GaN or InN could be synthesized with ammonia or azides as a nitrogen source. Ammonia is liquefied and loaded in to high pressure pump as further mixed in a microchannel with a solution consisting with Ga or In precursors such as $Ga(C_2H_5)_3$, GaX_3[114], $In(CH_3)_3$,[18] or InX_3[115] in hexane or octane ($X =$ Cl, Br, or I). Sodium azide (NaN_3) or trimethylsilyl azide (TMS-N_3) also can be a source for the nitride synthesis.[114-115]

Temperature requirement for the synthesis of crystalline GaN nanocrystals is up to 700 °C due to a thermally stable intermediate compound.[114] Therefore, it is required to have a high reaction temperature (figure 8.1). However, synthesis of InN nanocrystals requires in a range of temperatures of 200 to 400 °C and pressures of 100 to 200 bars in order to obtain well crystallized materials and to work in fluids having sufficient densities to solvate the nanoparticles.[115] This condition is within the operational range of a silicon-based microfluidic system. Since the nitrogen sources could be ammonia (gas) or azides (explosive), a high-pressure microreactor system could be an excellent tool for the nitride synthesis.

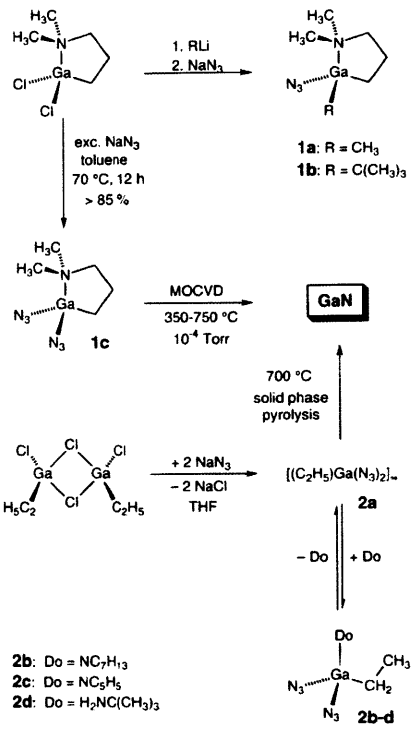

Figure 8.1: An example scheme of GaN synthesis.

One potential difficulty could be the solubility of precursors or intermediates. Protic materials such as alcohols are good solvents to dissolve ionic compounds such as InX_3 or NaN_3. However, in order to avoid oxidation of nanocrystals, it is generally necessary to avoid the use of protic solvents. Although it is reported that a limited amount of $InBr_3$ or InI_3 is soluble in toluene, NaN_3 is still insoluble in any aliphatic or aromatic solvents. In our preliminary experiments, we also checked that an intermediate $[In(CH_3)NH]_3$ is not soluble in organic solvents. From molecular structures, we can speculate most of the intermediates from InX_3 would be also insoluble in non-polar organic solvents.

Since TMS-N_3 is soluble in organic solvents, use of TMS-N_3 as a nitrogen source could be a possibility, but no successful synthesis has been reported. Still, an intermediate compound could have limited solubility. Therefore, developing a synthetic method using TMS-N_3 in non-protic polar solvent such as tetrahydrofuran or ethers could be an approach for InN nanocrystal synthesis.

8.2.2. In-line measurement system for infrared (IR) and near infrared (NIR)

Quantum dots emitting at the infrared (IR) or near infrared (NIR, 700-900 nm) regime have been interesting for applications such as solar cell or biological imaging. However, synthesis of bright quantum dots with narrow size distribution has been challenging due to the synthetic difficulty.[13]

Although we successfully synthesized InAs quantum dots with narrow size distribution using a multi-stage microfluidic system, it was difficult to optimize the synthesis of InAs / CdS or InAs / CdZnS core-shell quantum dots without a suitable in-line measurement device.

We may not need to change the in-line measurement device since current in-line measurement device is using a quartz capillary, which is transparent in NIR regime. Simply by installing suitable light sources, detectors, and optical fibers we could develop a system for quantum dots emitting in the IR or NIR regime.

Development of this in-line measurement system would enable to obtain high quality InAs / CdS or InAs / CnZnS core-shell nanocrystals. This system could allow for the investigation of new materials synthesis, emitting at IR regimes such as InSb nanocrystals, since InSb is a promising material for IR or NIR applications for the replacement of HgTe.[116-117] After successful syntheses of InSb nanocrystals, synthesis of $InAs_xSb_{1-x}$ alloy nanocrystals using the in-line measurement (IR or NIR) could be also interesting.

8.2.3. Integration of multi-step into a single reactor

As described in this thesis, multi-stem microfluidic systems provide advantages to obtain high quality single or structured nanocrystals. Since we improved the fabrication processes (Chapter 2), we could integrate a multi-stage system into a single silicon wafer. For example, all the mixing, aging, and sequential injection microreactors could be integrated on a 6-inch silicon wafer.

The most important operational issue would be control of temperatures. In order to minimize the temperature conduction from one part to another part of the wafer, wider insulating zone would be necessary. Not only with heating blocks, it would be also essential to control temperatures with cooling blocks maintained at a constant temperature.

This integration reduces the number of connections in a multi-stage microfluidic system, resulting in significant decrease of dead volumes and potential leaking at connections. Therefore, we can conduct a multi-stage chemical synthesis even more precisely, and the time for optimization process will be less. Ultimately, we can build a small factory.

The platform would also be applicable to other chemical transformations, such as those involved in synthesis of fine chemicals or pharmaceuticals.[118]

References

1. Gunther, A.; Khan, S. A.; Thalmann, M.; Trachsel, F.; Jensen, K. F., Transport and reaction in microscale segmented gas-liquid flow. *Lab Chip* **2004,** *4* (4), 278-286.

2. Gunther, A.; Jhunjhunwala, M.; Thalmann, M.; Schmidt, M. A.; Jensen, K. F., Micromixing of miscible liquids in segmented gas-liquid flow. *Langmuir* **2005,** *21* (4), 1547-1555.

3. Gervais, T.; Jensen, K. F., Mass transport and surface reactions in microfluidic systems. *Chem Eng Sci* **2006,** *61* (4), 1102-1121.

4. Jensen, K. F., Microreaction engineering - is small better? *Chem Eng Sci* **2001,** *56* (2), 293-303.

5. Marre, S.; Jensen, K. F., Synthesis of micro and nanostructures in microfluidic systems. *Chem Soc Rev* **2010,** *39* (3), 1183-1202.

6. Jahnisch, K.; Hessel, V.; Lowe, H.; Baerns, M., Chemistry in microstructured reactors. *Angew Chem Int Edit* **2004,** *43* (4), 406-446.

7. Jensen, K. F., Silicon-based microchemical systems: Characteristics and applications. *Mrs Bull* **2006,** *31* (2), 101-107.

8. Marre, S.; Baek, J.; Park, J.; Bawendi, M. G.; Jensen, K. F., High-Pressure/High-Temperature Microreactors for Nanostructure Synthesis. *Jala-J Lab Autom* **2009,** *14* (6), 367-373.

9. Baek, J.; Allen, P. M.; Bawendi, M. G.; Jensen, K. F., Investigation of Indium Phosphide Nanocrystal Synthesis Using a High-Temperature and High-Pressure Continuous Flow Microreactor. *Angew Chem Int Edit* **2011,** *50* (3), 627-630.

10. Marre, S.; Park, J.; Rempel, J.; Guan, J.; Bawendi, M. G.; Jensen, K. F., Supercritical Continuous-Microflow Synthesis of Narrow Size Distribution Quantum Dots. *Adv Mater* **2008,** *20* (24), 4830-+.

11. Yen, B.; Gunther, A.; Thalmann, M.; Bawendi, M. G.; Jensen, K. F., A microfabricated segmented-flow reactor for the synthesis of cadmium selenide quantum dots. *Roy Soc Ch* **2005,** (297), 127-129.

12. Yen, B. K. H.; Stott, N. E.; Jensen, K. F.; Bawendi, M. G., A continuous-flow microcapillary reactor for the preparation of a size series of CdSe nanocrystals. *Adv Mater* **2003,** *15* (21), 1858-1862.

13. Allen, P. M.; Liu, W. H.; Chauhan, V. P.; Lee, J.; Ting, A. Y.; Fukumura, D.; Jain, R. K.; Bawendi, M. G., InAs(ZnCdS) Quantum Dots Optimized for Biological Imaging in the Near-Infrared. *J Am Chem Soc* **2010,** *132* (2), 470-+.

14. Cao, Y. W.; Aksenton, J.; Soloviev, V.; Banin, U., Colloidal synthesis and properties of InAs/InP and InAs/CdSe core/shell nanocrystals. *Mater Res Soc Symp P* **2000,** *571*, 75-80.

15. Peng, X. G.; Wickham, J.; Alivisatos, A. P., Kinetics of II-VI and III-V colloidal semiconductor nanocrystal growth: "Focusing" of size distributions. *J Am Chem Soc* **1998,** *120* (21), 5343-5344.

16. Cao, Y. W.; Banin, U., Growth and properties of semiconductor core/shell nanocrystals with InAs cores. *J Am Chem Soc* **2000,** *122* (40), 9692-9702.

17. Xie, R.; Battaglia, D.; Peng, X., Colloidal InP nanocrystals as efficient emitters covering blue to near-infrared. *J Am Chem Soc* **2007,** *129* (50), 15432-+.

18. Xu, S.; Kumar, S.; Nann, T., Rapid synthesis of high-quality InP nanocrystals. *J Am Chem Soc* **2006,** *128* (4), 1054-1055.

19. Nakamura, H.; Yamaguchi, Y.; Miyazaki, M.; Maeda, H.; Uehara, M.; Mulvaney, P., Preparation of CdSe nanocrystals in a micro-flow-reactor. *Chem Commun* **2002,** (23), 2844-2845.

20. Hussain, S.; Won, N.; Nam, J.; Bang, J.; Chung, H.; Kim, S., One-Pot Fabrication of High-Quality InP/ZnS (Core/Shell) Quantum Dots and Their Application to Cellular Imaging. *Chemphyschem* **2009,** *10* (9-10), 1466-1470.

21. Eckert, C. A.; Knutson, B. L.; Debenedetti, P. G., Supercritical fluids as solvents for chemical and materials processing. *Nature* **1996,** *383* (6598), 313-318.

22. Desmoulins-Krawiec, S.; Aymonier, C.; Loppinet-Serani, A.; Weill, F.; Gorsse, S.; Etourneau, J.; Cansell, F., Synthesis of nanostructured materials in supercritical ammonia: nitrides, metals and oxides. *J Mater Chem* **2004,** *14* (2), 228-232.

23. Marre, S.; Adamo, A.; Basak, S.; Aymonier, C.; Jensen, K. F., Design and Packaging of Microreactors for High Pressure and High Temperature Applications. *Ind Eng Chem Res* **2010,** *49* (22), 11310-11320.

24. McMullen, J. P.; Jensen, K. F., Rapid Determination of Reaction Kinetics with an Automated Microfluidic System. *Org Process Res Dev* **2011,** *15* (2), 398-407.

25. Murray, C. B.; Nirmal, M.; Norris, D. J.; Bawendi, M. G., Synthesis and Structural Characterization of Ii-Vi Semiconductor Nanocrystallites (Quantum Dots). *Z Phys D Atom Mol Cl* **1993,** *26*, S231-S233.

26. Murray, C. B.; Norris, D. J.; Bawendi, M. G., Synthesis and Characterization of Nearly Monodisperse Cde (E = S, Se, Te) Semiconductor Nanocrystallites. *J Am Chem Soc* **1993,** *115* (19), 8706-8715.

27. Hines, M. A.; Guyot-Sionnest, P., Synthesis and characterization of strongly luminescing ZnS-Capped CdSe nanocrystals. *J Phys Chem-Us* **1996,** *100* (2), 468-471.

28. Michalet, X.; Pinaud, F. F.; Bentolila, L. A.; Tsay, J. M.; Doose, S.; Li, J. J.; Sundaresan, G.; Wu, A. M.; Gambhir, S. S.; Weiss, S., Quantum dots for live cells, in vivo imaging, and diagnostics. *Science* **2005,** *307* (5709), 538-544.

29. Fox, M., *Optical Properties of Solids*. Oxford: 2008.

30. Beard, M. C.; Knutsen, K. P.; Yu, P. R.; Luther, J. M.; Song, Q.; Metzger, W. K.; Ellingson, R. J.; Nozik, A. J., Multiple exciton generation in colloidal silicon nanocrystals. *Nano Lett* **2007,** *7* (8), 2506-2512.

31. Ellingson, R. J.; Beard, M. C.; Johnson, J. C.; Yu, P. R.; Micic, O. I.; Nozik, A. J.; Shabaev, A.; Efros, A. L., Highly efficient multiple exciton generation in colloidal PbSe and PbS quantum dots. *Nano Lett* **2005,** *5* (5), 865-871.

32. Semonin, O. E.; Luther, J. M.; Choi, S.; Chen, H. Y.; Gao, J. B.; Nozik, A. J.; Beard, M. C., Peak External Photocurrent Quantum Efficiency Exceeding 100% via MEG in a Quantum Dot Solar Cell. *Science* **2011,** *334* (6062), 1530-1533.

33. Guzelian, A. A.; Banin, U.; Kadavanich, A. V.; Peng, X.; Alivisatos, A. P., Colloidal chemical synthesis and characterization of InAs nanocrystal quantum dots. *Appl Phys Lett* **1996,** *69* (10), 1432-1434.

34. Reiss, P.; Protiere, M.; Li, L., Core/Shell Semiconductor Nanocrystals. *Small* **2009,** *5* (2), 154-168.

35. Dabbousi, B. O.; RodriguezViejo, J.; Mikulec, F. V.; Heine, J. R.; Mattoussi, H.; Ober, R.; Jensen, K. F.; Bawendi, M. G., (CdSe)ZnS core-shell quantum dots: Synthesis and characterization of a size series of highly luminescent nanocrystallites. *J Phys Chem B* **1997,** *101* (46), 9463-9475.

36. Micic, O. I.; Smith, B. B.; Nozik, A. J., Core-shell quantum dots of lattice-matched ZnCdSe2 shells on InP cores: Experiment and theory. *J Phys Chem B* **2000,** *104* (51), 12149-12156.

37. Li, J. J.; Wang, Y. A.; Guo, W. Z.; Keay, J. C.; Mishima, T. D.; Johnson, M. B.; Peng, X. G., Large-scale synthesis of nearly monodisperse CdSe/CdS core/shell nanocrystals using air-stable reagents via successive ion layer adsorption and reaction. *J Am Chem Soc* **2003,** *125* (41), 12567-12575.

38. Bae, W. K.; Nam, M. K.; Char, K.; Lee, S., Gram-Scale One-Pot Synthesis of Highly Luminescent Blue Emitting Cd1-xZnxS/ZnS Nanocrystals. *Chem Mater* **2008,** *20* (16), 5307-5313.

39. Chen, Y.; Vela, J.; Htoon, H.; Casson, J. L.; Werder, D. J.; Bussian, D. A.; Klimov, V. I.; Hollingsworth, J. A., "Giant" multishell CdSe nanocrystal quantum dots with suppressed blinking. *J Am Chem Soc* **2008,** *130* (15), 5026-+.

40. Ryu, E.; Kim, S.; Jang, E.; Jun, S.; Jang, H.; Kim, B.; Kim, S. W., Step-Wise Synthesis of InP/ZnS Core-Shell Quantum Dots and the Role of Zinc Acetate. *Chem Mater* **2009,** *21* (4), 573-575.

41. Lim, J.; Bae, W. K.; Lee, D.; Nam, M. K.; Jung, J.; Lee, C.; Char, K.; Lee, S., InP@ZnSeS, Core@Composition Gradient Shell Quantum Dots with Enhanced Stability. *Chem Mater* **2011,** *23* (20), 4459-4463.

42. Liu, W. H.; Greytak, A. B.; Lee, J.; Wong, C. R.; Park, J.; Marshall, L. F.; Jiang, W.; Curtin, P. N.; Ting, A. Y.; Nocera, D. G.; Fukumura, D.; Jain, R. K.; Bawendi, M. G., Compact Biocompatible Quantum Dots via RAFT-Mediated Synthesis of Imidazole-Based Random Copolymer Ligand. *J Am Chem Soc* **2010,** *132* (2), 472-483.

43. Schlamp, M. C.; Peng, X. G.; Alivisatos, A. P., Improved efficiencies in light emitting diodes made with CdSe(CdS) core/shell type nanocrystals and a semiconducting polymer. *J Appl Phys* **1997,** *82* (11), 5837-5842.

44. Son, D. I.; Park, D. H.; Choi, W. K.; Kim, T. W., Electroluminescence of a single active layer polymer-nanocrystal hybrid light-emitting diode with inversion symmetry. *Nanotechnology* **2009,** *20* (27).

45. Coe, S.; Woo, W. K.; Bawendi, M.; Bulovic, V., Electroluminescence from single monolayers of nanocrystals in molecular organic devices. *Nature* **2002,** *420* (6917), 800-803.

46. Choudhury, K. R.; Song, D. W.; So, F., Efficient solution-processed hybrid polymer-nanocrystal near infrared light-emitting devices. *Org Electron* **2010,** *11* (1), 23-28.

47. Steckel, J. S.; Coe-Sullivan, S.; Bulovic, V.; Bawendi, M. G., 1.3 mu m to 1.55 mu m tunable electroluminescence from PbSe quantum dots embedded within an organic device. *Adv Mater* **2003,** *15* (21), 1862-1866.

48. Malko, A. V.; Mikhailovsky, A. A.; Petruska, M. A.; Hollingsworth, J. A.; Htoon, H.; Bawendi, M. G.; Klimov, V. I., From amplified spontaneous emission to microring lasing using nanocrystal quantum dot solids. *Appl Phys Lett* **2002,** *81* (7), 1303-1305.

49. Klimov, V. I.; Mikhailovsky, A. A.; Xu, S.; Malko, A.; Hollingsworth, J. A.; Leatherdale, C. A.; Eisler, H. J.; Bawendi, M. G., Optical gain and stimulated emission in nanocrystal quantum dots. *Science* **2000,** *290* (5490), 314-317.

50. Kazes, M.; Lewis, D. Y.; Ebenstein, Y.; Mokari, T.; Banin, U., Lasing from semiconductor quantum rods in a cylindrical microcavity. *Adv Mater* **2002,** *14* (4), 317-+.

51. Iikawa, F.; Godoy, M. P. F.; Nakaema, M. K. K.; Brasil, M. J. S. P.; Maialle, M. Z.; Degani, M. A.; Ribeiro, E.; Medeiros-Ribeiro, G.; Carvalho, W.; Brum, J. A., Optical properties of type-I and II quantum dots. *Braz J Phys* **2004,** *34* (2B), 555-559.

52. Yu, K.; Zaman, B.; Romanova, S.; Wang, D. S.; Ripmeester, J. A., Sequential synthesis of type II colloidal CdTe/CdSe core-shell nanocrystals. *Small* **2005,** *1* (3), 332-338.

53. Ivanov, T.; Donchev, V.; Germanova, K.; Gomes, P. F.; Iikawa, F.; Brasil, M. J. S. P.; Cotta, M. A., Optical properties of multi-layer type II InP/GaAs quantum dots studied by surface photovoltage spectroscopy. *J Appl Phys* **2011,** *110* (6).

54. Mullin, J. W., *Crystallization*. 3rd ed.; Boston, 1993.

55. Adamson, A. W., *Physical Chemistry of Surfaces*. 5th ed.; Wiley: 1990.

56. Wagner, C., Theorie Der Alterung Von Niederschlagen Durch Umlosen (Ostwald-Reifung). *Z Elektrochem* **1961,** *65* (7-8), 581-591.

57. Sugimoto, T., *Monodispersed Particles*. 1 ed.; Elsevier: Amsterdam, 2001.

58. Jun, S.; Jang, E. J.; Chung, Y. S., Alkyl thiols as a sulfur precursor for the preparation of monodisperse metal sulfide nanostructures. *Nanotechnology* **2006,** *17* (19), 4806-4810.

59. Peterson, J. J.; Krauss, T. D., Fluorescence spectroscopy of single lead sulfide quantum dots. *Nano Lett* **2006,** *6* (3), 510-514.

60. Bruchez, M.; Moronne, M.; Gin, P.; Weiss, S.; Alivisatos, A. P., Semiconductor nanocrystals as fluorescent biological labels. *Science* **1998,** *281* (5385), 2013-2016.

61. Deen, W. M., *Analysis of transport phenomena*. Oxford University: New York, 1998.

62. Berker, *Handbuch der physik*. Springer-Verlag: Berlin, 1963; Vol. VII/2.

63. NIST NIST Thermodynamic Database. http://webbook.nist.gov/chemistry/.

64. Keybl, J. A microreactor system for high-pressure, multiphase homogeneous and heterogeneous catalyst measurements under continuous flow. Ph.D., Massachusetts Institute of Technology, Cambridge, 2011.

65. Allen, P. M.; Walker, B. J.; Bawendi, M. G., Mechanistic Insights into the Formation of InP Quantum Dots. *Angew Chem Int Edit* **2010,** *49* (4), 760-762.

66. Battaglia, D.; Peng, X. G., Formation of high quality InP and InAs nanocrystals in a noncoordinating solvent. *Nano Lett* **2002,** *2* (9), 1027-1030.

67. Liu, H. T.; Owen, J. S.; Alivisatos, A. P., Mechanistic study of precursor evolution in colloidal group II-VI semiconductor nanocrystal synthesis. *J Am Chem Soc* **2007,** *129* (2), 305-312.

68. Pradhan, N.; Reifsnyder, D.; Xie, R. G.; Aldana, J.; Peng, X. G., Surface ligand dynamics in growth of nanocrystals. *J Am Chem Soc* **2007,** *129* (30), 9500-9509.

69. Qu, L. H.; Peng, X. G., Control of photoluminescence properties of CdSe nanocrystals in growth. *J Am Chem Soc* **2002,** *124* (9), 2049-2055.

70. Rempel, J. Y.; Bawendi, M. G.; Jensen, K. F., Insights into the Kinetics of Semiconductor Nanocrystal Nucleation and Growth. *J Am Chem Soc* **2009,** *131* (12), 4479-4489.

71. Rempel, J. Y.; Trout, B. L.; Bawendi, M. G.; Jensen, K. F., Properties of the CdSe(0001), (0001), and (1120) single crystal surfaces: Relaxation, reconstruction, and adatom and admolecule adsorption. *J Phys Chem B* **2005,** *109* (41), 19320-19328.

72. Kikkeri, R.; Laurino, P.; Odedra, A.; Seeberger, P. H., Synthesis of Carbohydrate-Functionalized Quantum Dots in Microreactors. *Angew Chem Int Edit* **2010,** *49* (11), 2054-2057.

73. Nightingale, A. M.; de Mello, J. C., Controlled Synthesis of III-V Quantum Dots in Microfluidic Reactors. *Chemphyschem* **2009,** *10* (15), 2612-2614.

74. Li, L.; Protiere, M.; Reiss, P., Economic synthesis of high quality InP nanocrystals using calcium phosphide as the phosphorus precursor. *Chem Mater* **2008,** *20* (8), 2621-2623.

75. Polte, J.; Erler, R.; Thunemann, A. F.; Sokolov, S.; Ahner, T. T.; Rademann, K.; Emmerling, F.; Kraehnert, R., Nucleation and Growth of Gold Nanoparticles Studied via in situ Small Angle X-ray Scattering at Millisecond Time Resolution. *Acs Nano* **2010,** *4* (2), 1076-1082.

76. Epifani, M.; Arbiol, J.; Pellicer, E.; Morante, J. R., Growth of CdSe nanocrystals by a catalytic redox activation of ostwald ripening: A case study of the concept of traveling solubility perturbation. *Chem Mater* **2007,** *19* (20), 4919-4924.

77. Xie, R. G.; Li, Z.; Peng, X. G., Nucleation Kinetics vs Chemical Kinetics in the Initial Formation of Semiconductor Nanocrystals. *J Am Chem Soc* **2009,** *131* (42), 15457-15466.

78. Alivisatos, A. P., Semiconductor clusters, nanocrystals, and quantum dots. *Science* **1996,** *271* (5251), 933-937.

79. Kim, S.; Lim, Y. T.; Soltesz, E. G.; De Grand, A. M.; Lee, J.; Nakayama, A.; Parker, J. A.; Mihaljevic, T.; Laurence, R. G.; Dor, D. M.; Cohn, L. H.; Bawendi, M. G.; Frangioni, J. V., Near-infrared fluorescent type II quantum dots for sentinel lymph node mapping. *Nat Biotechnol* **2004,** *22* (1), 93-97.

80. Zimmer, J. P.; Kim, S. W.; Bawendi, M. G., Small water-soluble InAs/ZnSe quantum dots for biological imaging. *Abstr Pap Am Chem S* **2005,** *229*, U1082-U1082.

81. Liu, W. H.; Choi, H. S.; Zimmer, J. P.; Tanaka, E.; Frangioni, J. V.; Bawendi, M., Compact cysteine-coated CdSe(ZnCdS) quantum dots for in vivo applications. *J Am Chem Soc* **2007,** *129* (47), 14530-+.

82. Choi, H. S.; Liu, W.; Misra, P.; Tanaka, E.; Zimmer, J. P.; Ipe, B. I.; Bawendi, M. G.; Frangioni, J. V., Renal clearance of quantum dots. *Nat Biotechnol* **2007,** *25* (10), 1165-1170.

83. Xie, R. G.; Peng, X. G., Synthetic scheme for high-quality InAs nanocrystals based on self-focusing and one-pot synthesis of InAs-based core-shell nanocrystals. *Angew Chem Int Edit* **2008,** *47* (40), 7677-7680.

84. Thessing, J.; Qian, J. H.; Chen, H. Y.; Pradhan, N.; Peng, X. G., Interparticle influence on size/size distribution evolution of nanocrystals. *J Am Chem Soc* **2007,** *129* (10), 2736-+.

85. Geyer, S. M.; Allen, P. M.; Chang, L. Y.; Wong, C. R.; Osedach, T. P.; Zhao, N.; Bulovic, V.; Bawendi, M. G., Control of the Carrier Type in InAs Nanocrystal Films by Predeposition Incorporation of Cd. *Acs Nano* **2010,** *4* (12), 7373-7378.

86. Allen, P. M.; Liu, W. H.; Bawendi, M. G., Core(shell) InAs(CdZnS) quantum dots optimized for biological imaging in the near-infrared. *Abstr Pap Am Chem S* **2009,** *238*.

87. Ben-Lulu, M.; Mocatta, D.; Bonn, M.; Banin, U.; Ruhman, S., On the Absence of Carrier Multiplication in InAs Core/Shell/Shell Nanocrystals. *Springer Series Chem* **2009,** *92*, 280-282.

88. Aharoni, A.; Mokari, T.; Popov, I.; Banin, U., Synthesis of InAs/CdSe/ZnSe core/shell1/shell2 structures with bright and stable near-infrared fluorescence. *J Am Chem Soc* **2006,** *128* (1), 257-264.

89. Mokari, T.; Aharoni, A.; Popov, I.; Banin, U., Diffusion of gold into InAs nanocrystals. *Angew Chem Int Edit* **2006,** *45* (47), 8001-8005.

90. Kim, S. W.; Zimmer, J. P.; Ohnishi, S.; Tracy, J. B.; Frangioni, J. V.; Bawendi, M. G., Engineering InAsxP1-x/InP/ZnSe III-V alloyed core/shell quantum dots for the near-infrared. *J Am Chem Soc* **2005,** *127* (30), 10526-10532.

91. Cao, Y. W.; Banin, U., Synthesis and characterization of InAs/InP and InAs/CdSe core/shell nanocrystals. *Angew Chem Int Edit* **1999,** *38* (24), 3692-3694.

92. Banin, U.; Lee, C. J.; Guzelian, A. A.; Kadavanich, A. V.; Alivisatos, A. P.; Jaskolski, W.; Bryant, G. W.; Efros, A. L.; Rosen, M., Size-dependent electronic level structure of InAs nanocrystal quantum dots: Test of multiband effective mass theory. *J Chem Phys* **1998,** *109* (6), 2306-2309.

93. Wells, R. L.; Aubuchon, S. R.; Kher, S. S.; Lube, M. S.; White, P. S., Synthesis of Nanocrystalline Indium Arsenide and Indium-Phosphide from Indium(Iii) Halides and Tris(Trimethylsilyl)Pnicogens - Synthesis, Characterization, and Decomposition Behavior of I3in-Center-Dot-P(Sime(3))(3). *Chem Mater* **1995,** *7* (4), 793-800.

94. Qu, L. H.; Peng, Z. A.; Peng, X. G., Alternative routes toward high quality CdSe nanocrystals. *Nano Lett* **2001,** *1* (6), 333-337.

95. Colvin, V. L.; Schlamp, M. C.; Alivisatos, A. P., Light-Emitting-Diodes Made from Cadmium Selenide Nanocrystals and a Semiconducting Polymer. *Nature* **1994,** *370* (6488), 354-357.

96. Tessler, N.; Medvedev, V.; Kazes, M.; Kan, S. H.; Banin, U., Efficient near-infrared polymer nanocrystat light-emitting diodes. *Science* **2002,** *295* (5559), 1506-1508.

97. Battaglia, D.; Li, J. J.; Wang, Y. J.; Peng, X. G., Colloidal two-dimensional systems: CdSe quantum shells and wells. *Angew Chem Int Edit* **2003,** *42* (41), 5035-5039.

98. Yang, Y. A.; Wu, H. M.; Williams, K. R.; Cao, Y. C., Synthesis of CdSe and CdTe nanocrystals without precursor injection. *Angew Chem Int Edit* **2005,** *44* (41), 6712-6715.

99. Chan, E. M.; Alivisatos, A. P.; Mathies, R. A., High-temperature microfluidic synthesis of CdSe nanocrystals in nanoliter droplets. *J Am Chem Soc* **2005,** *127* (40), 13854-13861.

100. Shestopalov, I.; Tice, J. D.; Ismagilov, R. F., Multi-step synthesis of nanoparticles performed on millisecond time scale in a microfluidic droplet-based system. *Lab Chip* **2004,** *4* (4), 316-321.

101. Roig, Y.; Marre, S.; Cardinal, T.; Aymonier, C., Synthesis of Exciton Luminescent ZnO Nanocrystals Using Continuous Supercritical Microfluidics. *Angew Chem Int Edit* **2011,** *50* (50), 12071-12074.

102. Wang, F.; Yu, H.; Li, J.; Hang, Q.; Zemlyanov, D.; Gibbons, P. C.; Wang, L. W.; Janes, D. B.; Buhro, W. E., Spectroscopic properties of colloidal indium phosphide quantum wires. *J Am Chem Soc* **2007,** *129* (46), 14327-14335.

103. Li, L.; Reiss, P., One-pot synthesis of highly luminescent InP/ZnS nanocrystals without precursor injection. *J Am Chem Soc* **2008,** *130* (35), 11588-+.

104. Kim, S. W.; Ryu, E.; Kim, S.; Jang, E.; Jun, S.; Jang, H.; Kim, B., Step-Wise Synthesis of InP/ZnS Core-Shell Quantum Dots and the Role of Zinc Acetate. *Chemistry of Materials* **2009,** *21* (4), 573-575.

105. Park, J.; Kim, S.; Kim, S.; Yu, S. T.; Lee, B.; Kim, S. W., Fabrication of highly luminescent InP/Cd and InP/CdS quantum dots. *J Lumin* **2010,** *130* (10), 1825-1828.

106. Manna, L.; Scher, E. C.; Alivisatos, A. P., Synthesis of soluble and processable rod-, arrow-, teardrop-, and tetrapod-shaped CdSe nanocrystals. *J Am Chem Soc* **2000,** *122* (51), 12700-12706.

107. Katz, D.; Millo, O.; Levi, Y.; Banin, U.; Cao, Y. W., Size-dependent tunneling spectroscopy of InAs nanocrystals. *Physica B* **2000,** *284*, 1760-1761.

108. Jang, E.; Jun, S.; Pu, L., High quality CdSeS nanocrystals synthesized by facile single injection process and their electroluminescence. *Chem Commun* **2003,** (24), 2964-2965.

109. Al-Salim, N.; Young, A. G.; Tilley, R. D.; McQuillan, A. J.; Xia, J., Synthesis of CdSeS nanocrystals in coordinating and noncoordinating solvents: Solvent's role in evolution of the optical and structural properties. *Chem Mater* **2007,** *19* (21), 5185-5193.

110. Sarma, D. D.; Nag, A.; Santra, P. K.; Kumar, A.; Sapra, S.; Mahadevan, P., Origin of the Enhanced Photoluminescence from Semiconductor CdSeS Nanocrystals. *J Phys Chem Lett* **2010,** *1* (14), 2149-2153.

111. Wang, X. Y.; Ren, X. F.; Kahen, K.; Hahn, M. A.; Rajeswaran, M.; Maccagnano-Zacher, S.; Silcox, J.; Cragg, G. E.; Efros, A. L.; Krauss, T. D., Non-blinking semiconductor nanocrystals. *Nature* **2009,** *459* (7247), 686-689.

112. Peng, X. G.; Thessing, J., Controlled synthesis of high quality semiconductor nanocrystals. *Struct Bond* **2005,** *118*, 79-119.

113. Joung, S.; Yoon, S.; Han, C. S.; Kim, Y.; Jeong, S., Facile synthesis of uniform large-sized InP nanocrystal quantum dots using tris(tert-butyldimethylsilyl)phosphine. *Nanoscale Res Lett* **2012,** *7*, 1-8.

114. Manz, A.; Birkner, A.; Kolbe, M.; Fischer, R. A., Solution synthesis of colloidal gallium nitride at unprecedented low temperatures. *Adv Mater* **2000,** *12* (8), 569-573.

115. Choi, J.; Gillan, E. G., Low-temperature solvothermal synthesis of nanocrystalline indium nitride and Ga-In-N composites from the decomposition of metal azides. *J Mater Chem* **2006,** *16* (38), 3774-3784.

116. http://www.ioffe.ru/SVA/NSM/Semicond/InSb/index.html.

117. Piepenbrock, M. O. M.; Stirner, T.; Kelly, S. M.; O'Neill, M., A low-temperature synthesis for organically soluble HgTe nanocrystals exhibiting near-infrared photoluminescence and quantum confinement. *J Am Chem Soc* **2006,** *128* (21), 7087-7090.

118. Hartman, R. L.; Jensen, K. F., Microchemical systems for continuous-flow synthesis. *Lab Chip* **2009,** *9* (17), 2495-2507.

119. Gupta, A.; Swihart, M. T.; Wiggers, H., Luminescent Colloidal Dispersion of Silicon Quantum Dots from Microwave Plasma Synthesis: Exploring the Photoluminescence Behavior Across the Visible Spectrum. *Adv Funct Mater* **2009,** *19* (5), 696-703.

120. Lu, X. M.; Ziegler, K. J.; Ghezelbash, A.; Johnston, K. P.; Korgel, B. A., Synthesis of germanium nanocrystals in high temperature supercritical fluid solvents. *Nano Lett* **2004,** *4* (5), 969-974.

121. Ding, Z. F.; Quinn, B. M.; Haram, S. K.; Pell, L. E.; Korgel, B. A.; Bard, A. J., Electrochemistry and electrogenerated chemiluminescence from silicon nanocrystal quantum dots. *Science* **2002,** *296* (5571), 1293-1297.

122. Holmes, J. D.; Ziegler, K. J.; Doty, R. C.; Pell, L. E.; Johnston, K. P.; Korgel, B. A., Highly luminescent silicon nanocrystals with discrete optical transitions. *J Am Chem Soc* **2001,** *123* (16), 3743-3748.

Appendix A

Germanium Nanocrystal Synthesis

A.1. Introduction

Solution-based synthesis of group IV nanocrystals has been challenging due to their covalent bonding. This bonding covalence requires high temperature to form crystalline structures. Although some groups have reported synthesis of silicon nanocrystals in solution phase, the temperatures for the synthesis of silicon particles were as high as 650 °C, which was almost at the decomposition temperature of the thermally stable solvents such as toluene or benzene.

Currently many groups are focusing on study of the silicon nanocrystal properties rather than solution phase synthesis of silicon nanocrystals. This is because the optical and electronic properties of the silicon nanocrystals are still not well studied. Recently solid phase synthetic method to obtain high quality silicon nanocrystal was reported, and this method requires over 1100 °C. Decomposition of the silane precursors by plasma in gas phase is an alternative synthetic method.[119] Since it is very difficult to obtain high quality silicon nanocrystal in solution phase, advances of the synthetic method are toward those methods rather than finding a new synthetic way in solution phase.

Among group IV materials, synthesis of germanium nanocrystal could have a better chance to be synthesized in a solution phase. This is because germane precursors have lower decomposition temperature than silane precursors due to the weaker atomic bonding. It is reported that germanium film can crystallize at a temperature as low as 415 °C, which is below decomposition temperature of commonly used organic solvents.[120-122]

We synthesized germanium nanocrystals by thermal decomposition of diphenylgermane, and tetrapropylgermane with high pressure and high temperature continuous microfluidic system. We used a synthetic condition of over 400 °C and 65 bar, which is not easily obtainable from batch system.

A.2. Methods

A.2.1. Decomposition of diphenylgermane

Diphenylgermane was used for germanium nanocrystal synthesis. 1:1 vol % mixture of octane and butanol or a 1:1 vol% mixture of dodecane and octanol was used as solvents. The diphenylgermane precursor concentration was 40 mM and the typical reaction temperature was controlled at between 400 °C and 410 °C. The system pressure was maintained at 70 Bar, and the residence times were varied from 20 seconds to 1 minute.

A.2.2. Decomposition of tetrapropylgermane

Tetrapropylgermane has higher decomposition temperature than diphenylgermane, and therefore the decomposition occurs above 480 °C. We used 1:1 vol % mixture of octane and butanol as a solvent.

A.2.3. Reactor and operation

A single channel silicon based microreactor with a channel width of 300 μm, a depth of 280 μm, and a total volume of 140 μl was used for the synthesis.

A.3. Results and discussion: diphenylgermane decomposition

Figure A.1 shows the transmission electron microscope images of the germanium nanocrystals synthesized at 410 °C for different residence times: 30 seconds and 20 seconds. Since the sizes of the germanium particles are small (2 - 3 nm in diameter) and the contrast of the images is poor due to low atomic electronic density of germanium, it is difficult to compare the sizes of the particles.

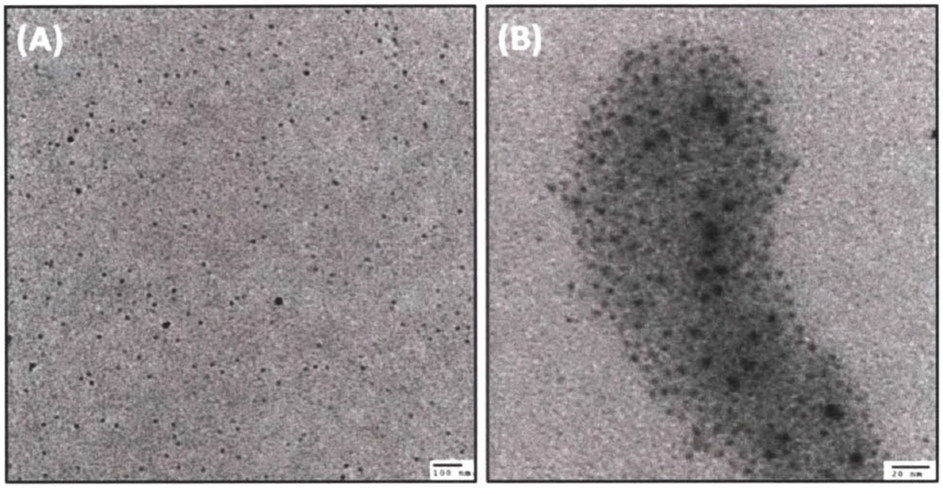

Figure A.1: TEM images of the germanium nanocrystals synthesized at a temperature of 410 °C for (A) 30 seconds and (B) 20 seconds.

Figure A.2 shows absorption spectra of germanium nanocrystals synthesized at different conditions. Since the first absorption features are not clear, it is difficult to understand the effect of temperatures and residence times from optical measurements. However, we speculates that the absorptions at between 300 nm and 350 nm are due to the germanium nanocrystal formation since we were not able to observe any particle formation as well as any absorptions at this range from the product solutions at below 390 °C. This absorption could be directly from the germanium nanocrystals or from the interface of the nanocrystals.

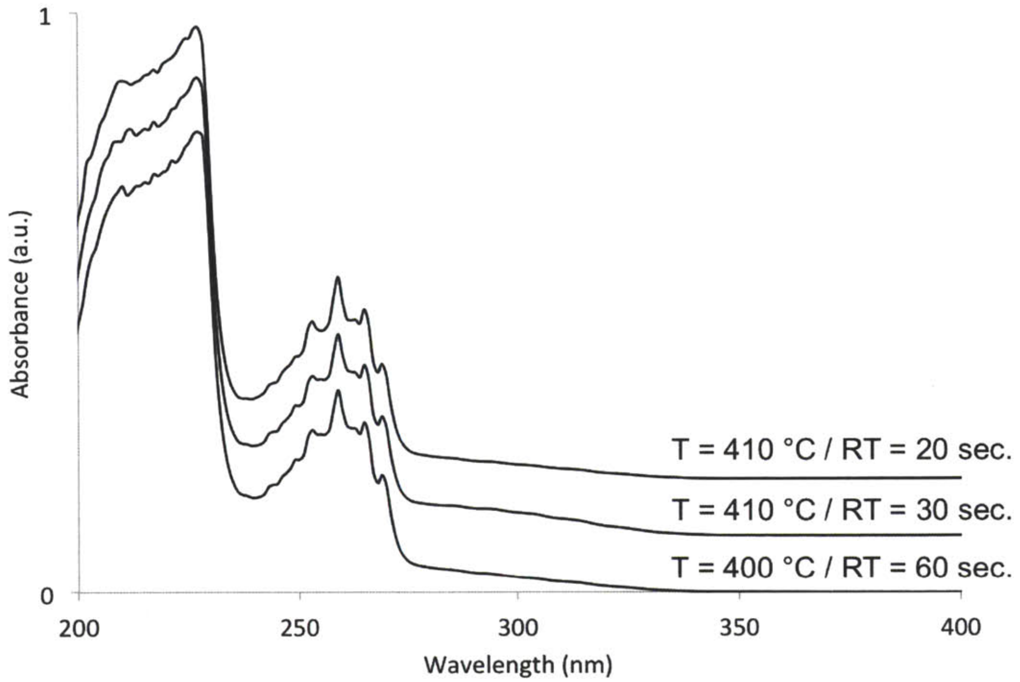

Figure A.2: Absorption spectra of germanium nanocrystals by thermal decomposition of diphenylgermane at different temperatures and residence times in octane and butanol.

Unfortunately, we observed black or shiny deposition on the channel walls at above 410 °C (Figure A.3). This could be due to the fast decomposition of the germane precursors in a low-density solvent as well as due to not sufficient surface passivation by the surfactant, butanol. The density of octane at 410 °C is less than 0.3 g / ml which is usually not sufficient density to hold nanoparticles. Perhaps, butanol is not a suitable surfactant for germanium nanoparticles.

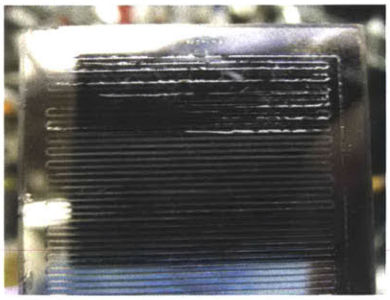

Figure A.3: Germanium deposition on the microreactor channel. This was observed when diphenylgermane decomposed above 410 °C. A 1:1 vol % mixture of octane and butanol was used as the solvent.

Since oleic acid has been widely used as surfactants for the synthesis of nanoparticles such as oxides or quantum dots, and has a hydroxyl group, 1:1 vol % mixture of octane and oleic acid was used as a solvent for the germanium particle synthesis. Oleic acid has longer chain than butanol or octane, and allows for obtaining sufficient solvent density to hold nanoparticles at high temperature. Figure A.4 is the absorption spectra of germanium nanocrystals synthesized at different temperature and flowrates. We were able to observe absorptions at a wavelength between 300 nm and 350 nm, but were not able to observe the clear first absorption feature.

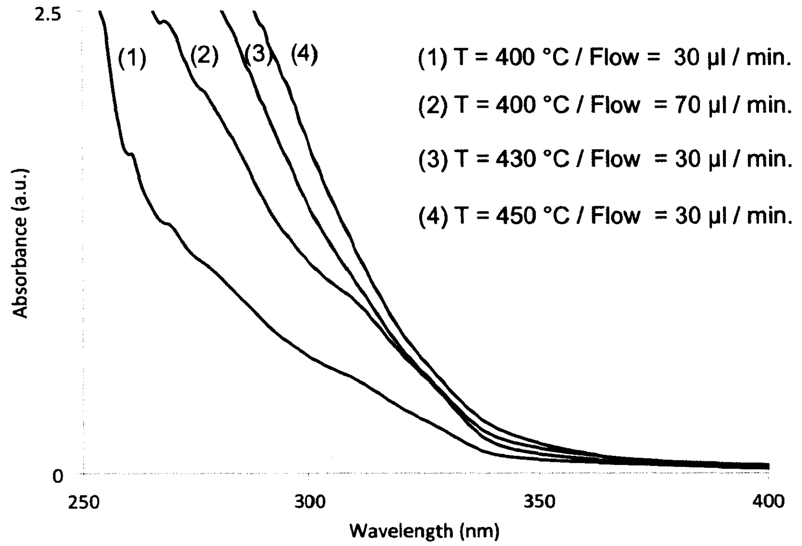

Figure A.4: Absorption spectra of germanium nanocrystals by thermal decomposition of diphenylgermane at different temperatures and residence times in octane and oleic acid.

Figure A.5 Shows the germanium particles synthesized in the octane and oleic acid mixture at 450 °C with 30 µl / min flow rate. Interstingly, we were able to use the temperature up to 430 °C without deposition. The sizes of the particles were small and the size distribution of the particles was worse than the previous case with octane and butanol solvent. We were also able to observe some aggregated particle clusters. We observed black deposition in the reactor channels after 10 minutes at 450 °C.

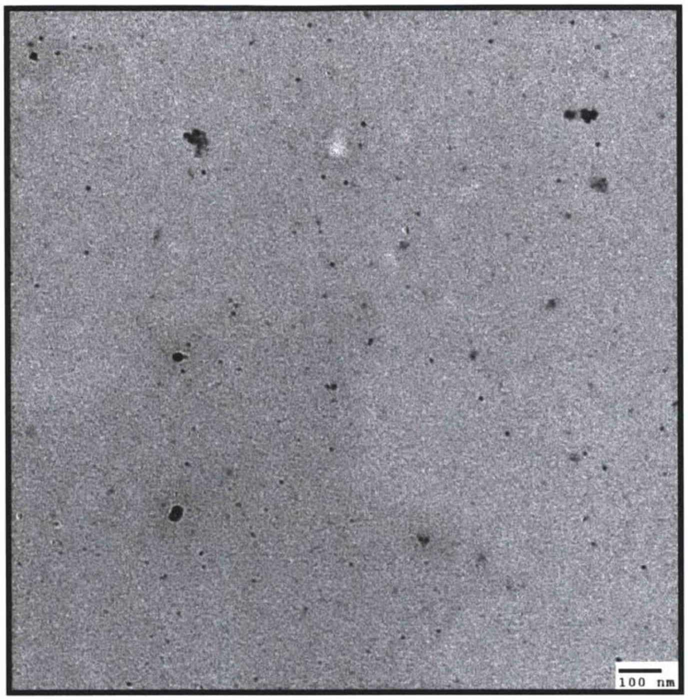

Figure A.5: TEM images of the germanium nanocrystals synthesized from diphenylgermane at a temperature of 450 °C with a flow rate of 30 µl / min

Since alcohols could be better surfactant than carboxylic acid, and higher solvent density could be better for the larger particle synthesis, we also used dodecane and octanol mixture as a solvent. This 1:1 vol % mixture of dodecane and octanol solvent has higher density than octane and butanol mixture at high temperature, so it can hold larger particles. From the previous experiment with using butanol and octane, we observed that a temperature of 390 °C is too low for the thermal decomposition of diphenylgermane precursor, and above 410 °C channel clogging was observed. So, we kept the reaction temperature at 400 °C. In order to understand effect of precursor concentration, we adjusted the concentration by utilizing additional syringe pump. The conditions for each sample are shown in the table A.1. Figure A.6 is TEM images of the germanium nanocrystals synthesized from the 9 mM precursor solution, with 220 µl / min flowrate. Figure A.7 is the germanium nanocrystals synthesized at different conditions described in table A.1.

Table A.1: Reaction conditions of germanium nanocrystal samples. Diphenylgermane is used as the precursors, and the temperature was fixed at 400 °C. 1:1 vol % mixture of dodecane and octane was used as the solvent.

Sample Name	Concentration	Temperature	Flowrate
DPG_DO_220_9	9 mM	400 C	220 µl / min
DPG_DO_350_71	71 mM	400 C	350 µl / min
DPG_DO_400_50	50 mM	400 C	400 µl / min
DPG_DO_400_25	25 mM	400 C	400 µl / min
DPG_DO_200_25	25 mM	400 C	200 µl / min

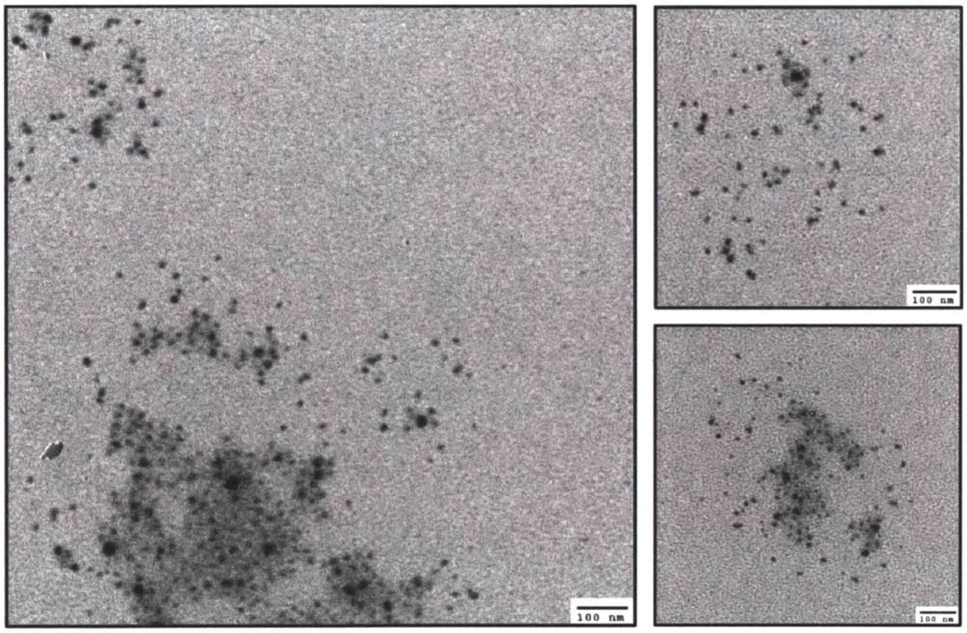

Figure A.6: TEM images of the DPG_DO_220_9 sample.

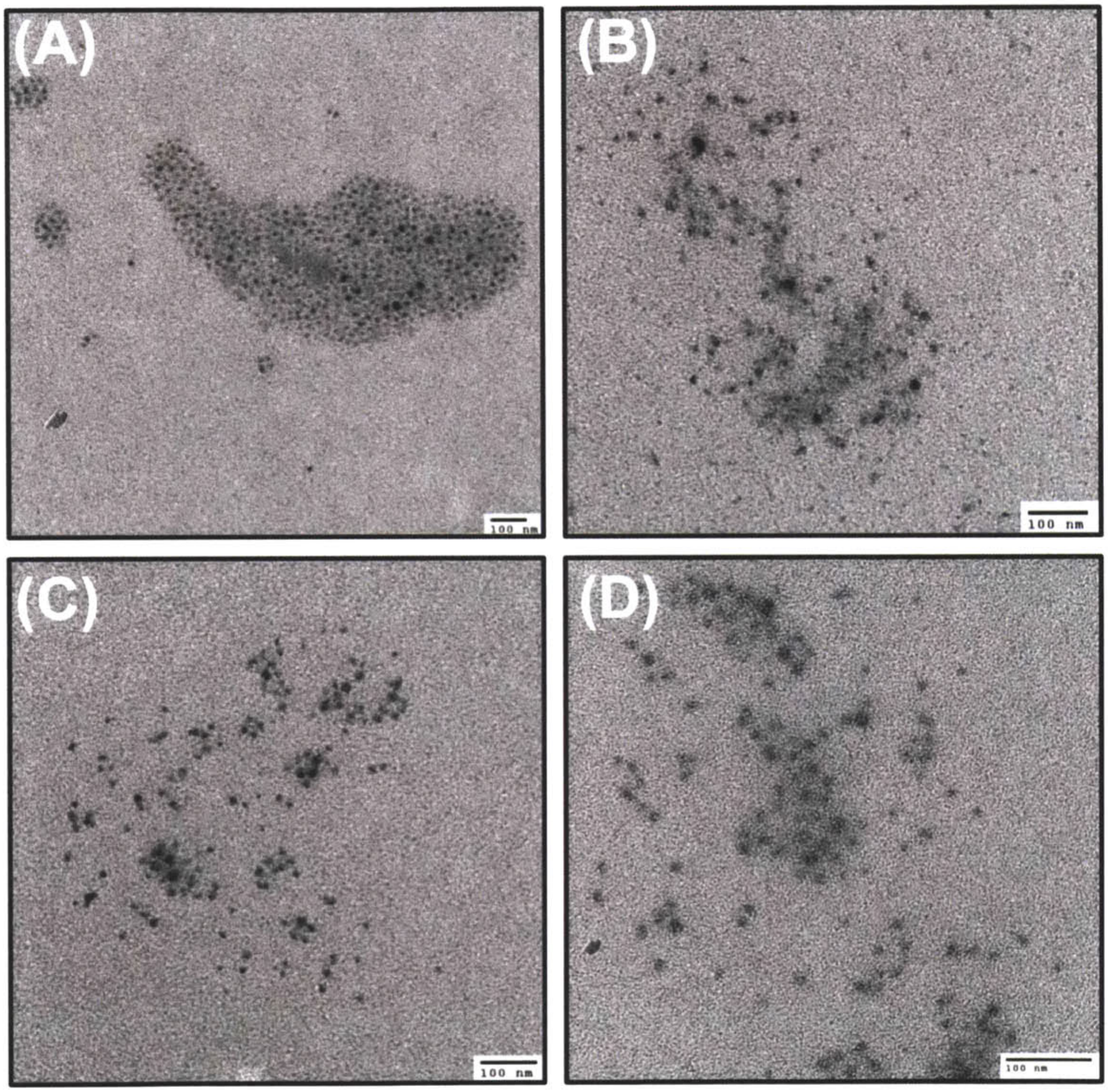

Figure A.7: TEM images of the (A) DPG_DO_350_71, (B) DPG_DO_400_50, and (C, D) DPG_DO_400_25 samples.

A.4. Results and discussion: tetrapropylgermane decomposition

At the decomposition temperature of tetrapropylgermane (480 °C), the density of the solvent is below 0.2 g / ml, which is not sufficient to hold the nanocrystals effectively. As a result we observed aggregated germanium clusters rather than particle formation. We were not able to observe clear first absorption feature from the absorbance (figure A.8).

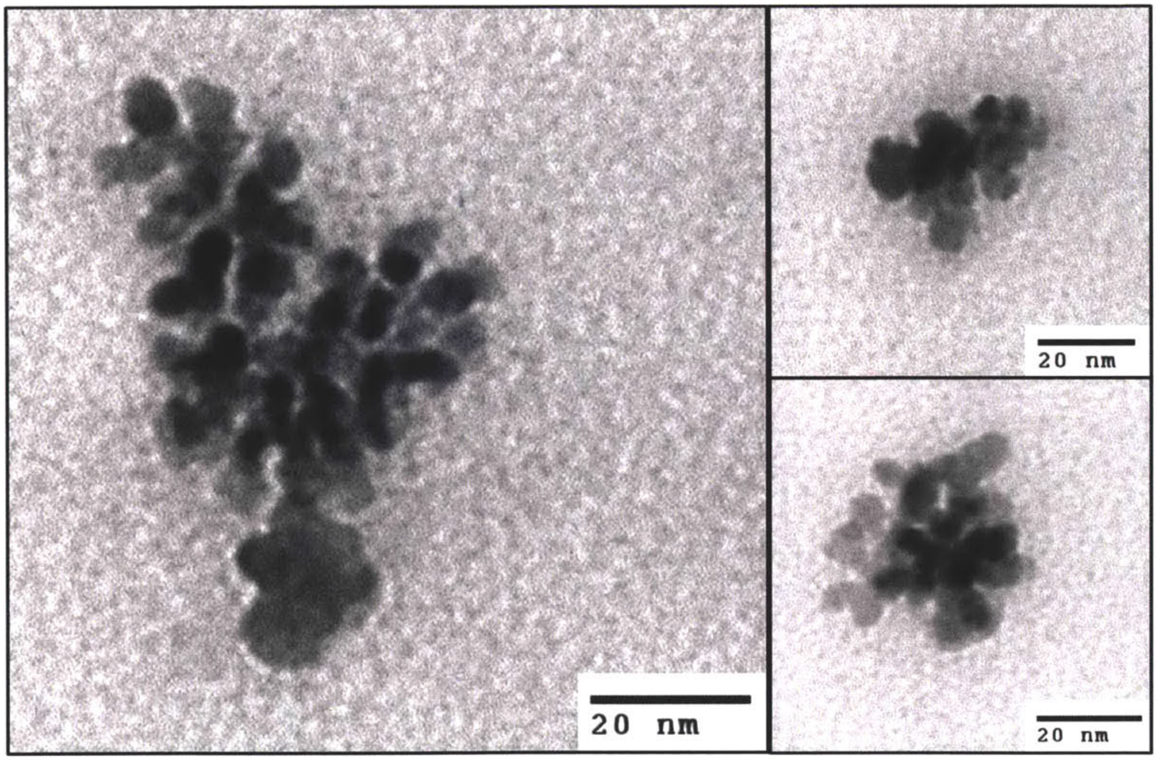

Figure A.8: TEM images of the gernamin nanocrystals by thermal decomposition of tetrapropylgermane in 1:1 vol% mixture of octane and butanol at 480 °C. The flowrate was 30 μl / min, and concentration of the precursor was 40 mM.

Appendix B. Supporting information of Chapter 7.

Previously, we ran another set of the experiment described in Chapter 7. We used different mixing reactor: T-shape mixing with larger reactor volume (120 μl). All the other conditions and concentrations were same. This time we changed temperature from 130 °C to 190 °C, instead of between 110 °C and 160 °C.

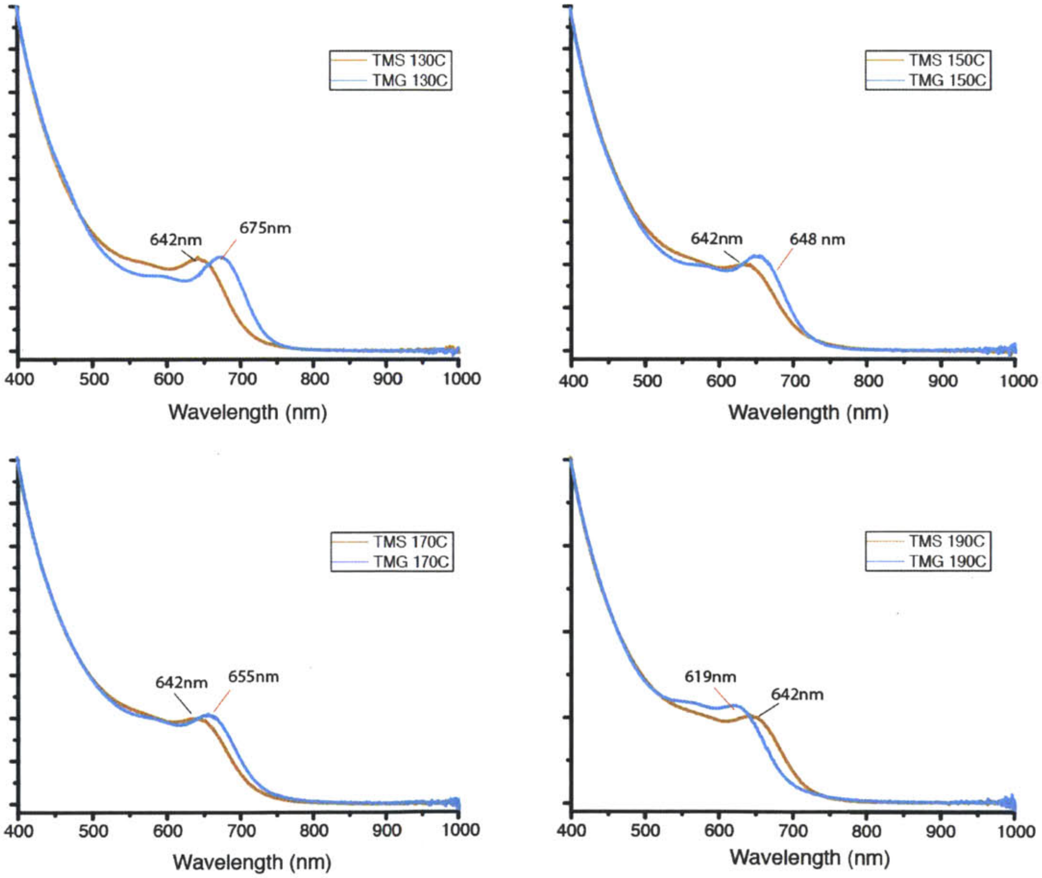

Figure B.1: Absorbance spectra of InAs quantum dots synthesized from different arsenic sources. All the conditions such as concentrations, system pressure, and solvent, aging reactor except for the mixing reactor were identical to the system described in Chapter 7.

Similarly to the result described in Chapter 7, as we increase mixing temperature, we were able to observe the first absorption feature was staying at the same position (642 nm) when TMS_3As was used as the arsenic source, and the feature was shifting to blue when TMG_3As was used. However, in this experiment, we were able to observe a phenomenon that the first absorption features were shifting about 7 nm to the longer wavelength as we increase temperature from 150 °C to 170 °C. Since we observed deposition of solids on the reactor walls, we attributed this shift to differences in deposition. In order to perform experiments more precisely, we used the jet-shaped reactor. We also adjusted the mixing temperature range to lower. These helped to operate system with more accuracy.

Appendix C. Calculation (MATLAB) of flow distributions

```
function FdisCalc

%Side Flow rates without units.
%unit: microliter / sec
Totflow = 10;


%Main Channel: Each Section Lengths and dimensions.
%c200 : cold         / 0.2 mm channel width.
%i200 : intermediate / 0.2 mm channel width.
%h200 : hot          / 0.2 mm channel width.
%h400 : hot          / 0.4 mm channel width.

Main_Large_depth = 0.45;            % unit: mm
Main_Large_width = 0.40;            % unit: mm
M_inlet_c = 4.356 + 7.959 + pi*0.6;   % unit: mm
M_inlet_i = 7;
M_inlet_h = 38.765 + 0.5*pi*0.6;

M1_c200 = 0.5*pi*0.4;
M1_i200 = 7;
M1_h200 = 1.014+0.3; % including half of bending
M1_h400 = 0.3 + 4.6 + 0.4 + 31.342 + 30.542*2 + 0.5*pi*0.6 + 2*pi*0.4 + pi*0.6;

M2_c200 = 0.5*pi*0.4;
M2_i200 = 7;
M2_h200 = 1.014+0.3; % including half of bending
M2_h400 = 0.3 + 3.8 + 0.375 + 32.142 + 30.542*2 + 2*1.25*pi*0.4 + pi*0.6;

M3_c200 = 0.5*pi*0.4;
M3_i200 = 7;
M3_h200 = 1.014+0.3; % including half of bending
M3_h400 = 0.3 + 2.992 + 0.275 + 0.4 + 3.601 + 31.342 + 4*30.542 + 2*2.25*pi*0.4 + 2*pi*0.6;

M4_c200 = 0.5*pi*0.4;
M4_i200 = 7;
M4_h200 = 1.014+0.3; % including half of bending
M4_h400 = 0.3 + 2.2 + 0.275 + 0.4 + 3.575 + 32.142 + 6*30.542 + 2*3.25*pi*0.4 + 2*pi*0.6;

M5_c200 = 0.5*pi*0.4;
M5_i200 = 7;
M5_h200 = 1.014+0.3; % including half of bending
M5_h400 = 0.3 + 1.377 + 0.174 + 0.4 + 3.575 + 0.415 + 11.599 + 31.342 + 10*30.542 +
```

```
2*4.25*pi*0.4 + 3*pi+0.6;

M6_c200 = 0.5*pi*0.4;
M6_i200 = 7;
M6_h200 = 1.014+0.3; % including half of bending
M6_h400 = 0.3 + 0.585 + 0.175 + 0.4 + 3.575 + 0.415 + 11.575 + 32.142 + 8*30.542 + 31.342 +
5.199*2 + 17.433*2 + 22*2 + 24.1 + 2*7.5*pi*0.4 + 4*pi+0.6 + 1.423;
M6_i400 = 7;
M6_c400 = 1.1 + 13.059 + 6.667 + pi+0.6;


%Temperature Profile
Intermed_Length = 9.081;  %The vertical length of the zone
Hot_T = 300;            %Temperature at reaction zone
Cold_T = 80;            %Temperature at cold zone


%Viscosity Value (example, octane at 65 Bar, Hot at 300C, Cold at 100C)
%Solvent viscosities. From NIST Thermodynamic Database.
Hot_vis = 0.000063041;
Cold_vis = 0.00026708;

%Average viscosity calculation
Discr = linspace(Cold_T, Hot_T,300);
Vis_sum = 0;

for m=1:300
Vis_sum = viscosity(Discr(m))+Vis_sum;
end
Inter_vis = Vis_sum / 300;


x0=[1 2 3 4 5 6 7 8];
L = fsolve(@(x) Len_Obj(x),x0);
SideStream1 = [L(1) L(2) L(3) L(4) (Totflow-L(1)-L(2)-L(3)-L(4))];
display(SideStream1)
Sratio1 = SideStream1 / Totflow;
display(Sratio1)

SideStream2 = [L(5) L(6) L(7) L(8) (Totflow-L(5)-L(6)-L(7)-L(8))];
display('--------------------------------------------')
display(SideStream2)
Sratio2 = SideStream2 / Totflow;
display(Sratio2)

end

%Viscosity function. (Fitting)
function Vis = viscosity(T)
%This expression is fitting data with NIST Thermodynamic Database
```

```
Vis = exp(-7.1424*10^(-3)*T)*0.0010591;
end


function k = Len_Obj(x)
%Temperature Profile
Intermed_Length = 9.081;
Hot_T = 300;
Cold_T = 100;

%Viscosity Value
Hot_vis = 0.000063041;
Cold_vis = 0.00026708;

Discr = linspace(Cold_T, Hot_T,300);
Vis_sum = 0;

for m=1:300
Vis_sum = viscosity(Discr(m))+Vis_sum;
end
Inter_vis = Vis_sum / 300;

%Main Channel Resist, (here the depth is 0.45 mm)
Rmi = Resis(0.4, 0.45, 26.94698, Cold_vis);
Rm1 = Resis(0.2, 0.45, 5.01832, Cold_vis) + Resis(0.2, 0.45, 13.798, Inter_vis) + 1.323644*
Resis(0.4, 0.45, 140.931, Hot_vis);
Rm2 = Resis(0.2, 0.45, 3.65664, Cold_vis) + Resis(0.2, 0.45, 14, Inter_vis)+ 1.323644 *
Resis(0.4, 0.45, 136.857, Hot_vis);
Rm3 = Resis(0.2, 0.45, 3.65664, Cold_vis) + Resis(0.2, 0.45, 14, Inter_vis)+ 1.323644 *
Resis(0.4, 0.45, 133.657, Hot_vis);
Rm4 = Resis(0.2, 0.45, 3.65664, Cold_vis) + Resis(0.2, 0.45, 14, Inter_vis)+ 1.323644 *
Resis(0.4, 0.45, 130.458, Hot_vis);
Rm5 = Resis(0.2, 0.45, 3.65664, Cold_vis) + Resis(0.2, 0.45, 14, Inter_vis)+ 1.323644 *
Resis(0.4, 0.45, 127.257, Hot_vis);
Rm6 = Resis(0.2, 0.45, 3.65664, Cold_vis) + Resis(0.2, 0.45, 14, Inter_vis)+ 1.323644 *
Resis(0.4, 0.45, 206.0848, Hot_vis);
Rm7 = Resis(0.2, 0.45, 3.65664, Cold_vis) + Resis(0.2, 0.45, 14, Inter_vis)+ 1.323644 *
Resis(0.4, 0.45, 280.1135, Hot_vis);
Rm8 = Resis(0.2, 0.45, 3.65664, Cold_vis) + Resis(0.2, 0.45, 14, Inter_vis)+ 1.323644 *
Resis(0.4, 0.45, 350.9817, Hot_vis);
Rm9 = Resis(0.2, 0.45, 3.65664, Cold_vis) + Resis(0.2, 0.45, 14, Inter_vis)+ 1.323644 *
Resis(0.4, 0.45, 562.7495, Hot_vis);
Rm10 = Resis(0.4, 0.45, 700, Hot_vis)
Side10 = Resis(0.08, 0.2, 190, Cold_vis)


%Side Channel Resist (here, the depth is 0.1 mm)
S1  = Resis(0.08, 0.1, 180.0, Cold_vis);
```

```
S2  = Resis(0.08, 0.1, 181.6, Cold_vis);
S3  = Resis(0.08, 0.1, 184.3, Cold_vis);
S4  = Resis(0.08, 0.1, 187.1, Cold_vis);
S5  = Resis(0.08, 0.1, 190.0, Cold_vis);
S6  = Resis(0.08, 0.1, 185.1, Cold_vis);
S7  = Resis(0.08, 0.1, 188.1, Cold_vis);
S8  = Resis(0.08, 0.1, 192.4, Cold_vis);
S9  = Resis(0.08, 0.1, 193.5, Cold_vis);
S10  = Resis(0.08, 0.1, 194.8, Cold_vis);


%Main Flow and Side Flow.
Main_Flow = 30;
Side_Flow = 10;
%Pressure Drops
P10 = 50*100000;  %Basis Pressure. Any pressure could be ok.



P10_9 = Rm6 * (Main_Flow + Side_Flow + x(5) + x(6) + x(7) + x(8));
P9_8 = Rm6 * (Main_Flow + x(1) + x(2) + x(3) + x(4) + x(5) + x(6) + x(7) + x(8));
P8_7 = Rm6 * (Main_Flow + x(1) + x(2) + x(3) + x(4) + x(5) + x(6) + x(7));
P7_6 = Rm6 * (Main_Flow + x(1) + x(2) + x(3) + x(5) + x(6) + x(7));
P6_5 = Rm5 * (Main_Flow + x(1) + x(2) + x(3) + x(5) + x(6));
P5_4 = Rm4 * (Main_Flow + x(1) + x(2) + x(5) + x(6));
P4_3 = Rm3 * (Main_Flow + x(1) + x(2) + x(5));
P3_2 = Rm2 * (Main_Flow + x(1) + x(5));
P2_1 = Rm1 * (Main_Flow + x(1));
P1_i = Rmi * (Main_Flow);

PS1 = P10 + P10_9 + S5 * (Side_Flow-x(1)-x(2)-x(3)-x(4));
PS2 = P10 + S10 * (Side_Flow - x(5) - x(6) - x(7) - x(8));

P9 = P10 + P10_9;
P8 = P10 + P10_9 + P9_8;
P7 = P10 + P10_9 + P9_8 + P8_7;
P6 = P10 + P10_9 + P9_8 + P8_7 + P7_6;
P5 = P10 + P10_9 + P9_8 + P8_7 + P7_6 +P6_5;
P4 = P10 + P10_9 + P9_8 + P8_7 + P7_6 +P6_5 +P5_4;
P3 = P10 + P10_9 + P9_8 + P8_7 + P7_6 +P6_5 +P5_4 + P4_3;
P2 = P10 + P10_9 + P9_8 + P8_7 + P7_6 +P6_5 +P5_4 + P4_3 +P3_2;
P1 = P10 + P10_9 + P9_8 + P8_7 + P7_6 +P6_5 +P5_4 + P4_3 +P3_2 +P2_1;

k(1) = PS2 - S9*x(8) - P8;
k(2) = PS1 - S4*x(4) - P7;
k(3) = PS2 - S8*x(7) - P6;
k(4) = PS1 - S3*x(3) - P5;
k(5) = PS2 - S7*x(6) - P4;
k(6) = PS1 - S2*x(2) - P3;
k(7) = PS2 - S6*x(5) - P2;
```

```
k(8) = PS1 - S1*x(1) - P1;
end

%Fluid Resist (Channel resist) calculation
function Resistance = Resis(Widths, Depths, Lengths, vis_cos)
%Definition: Del P = Resistance * vol Q  (All SI Units are used)
%Depth > Width
Wid = Widths * 0.001 / 2;
Dep = Depths * 0.001 / 2;
Length = Lengths * 0.001;

Term1 = 0;
for vir_k = 1:2:7
Term1 = tanh(vir_k*pi*Wid/2/Dep)/vir_k^5 + Term1;
end

Term2 = 1 - 192*Dep / pi^5 / Wid * Term1;
Resistance = 3*vis_cos/4/Wid/Dep^3*Length / Term2;

End
```

Appendix D. Photo-masks of microreactors

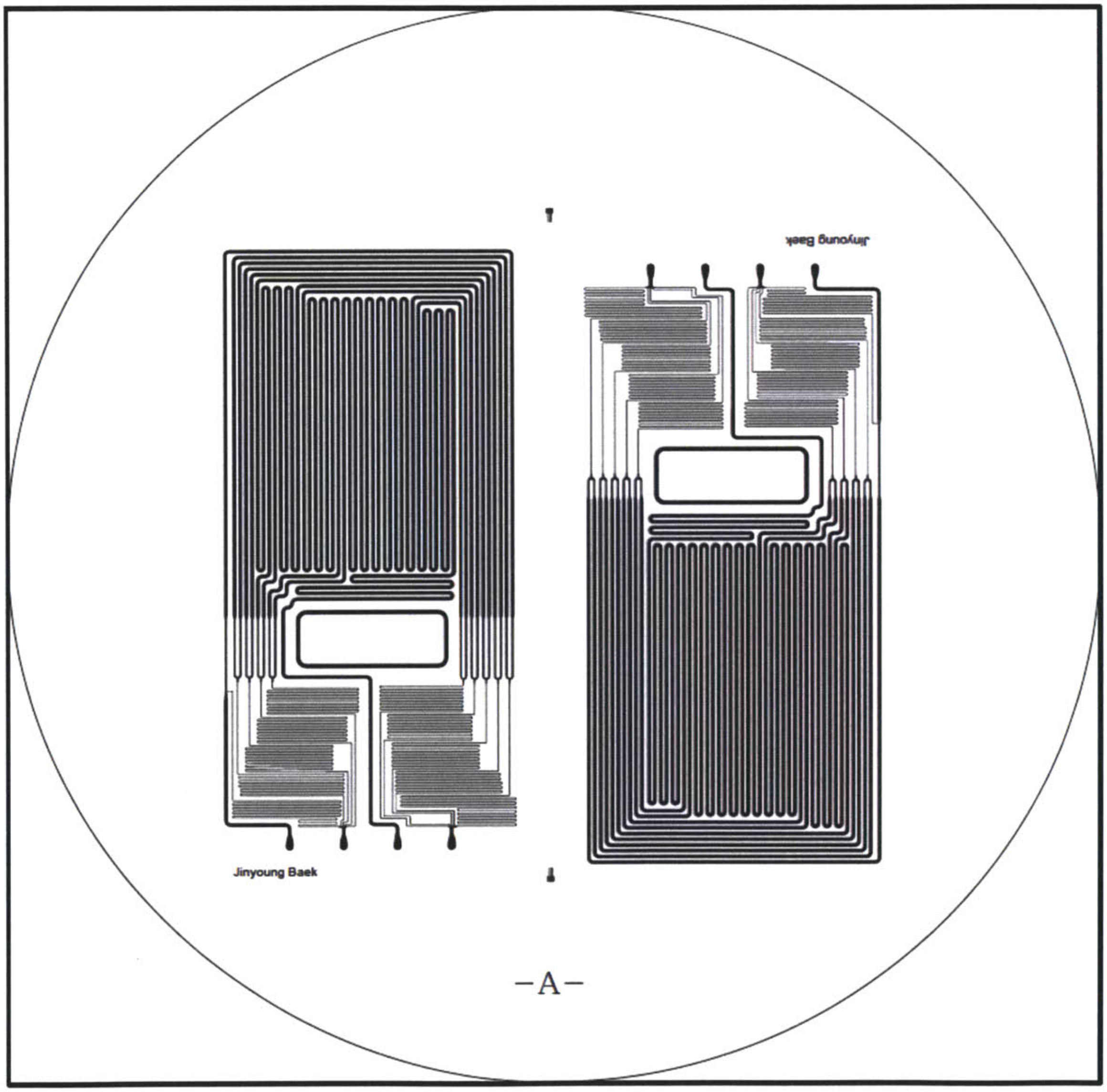

Figure D.1: Sequential Injection Microreactor: Front

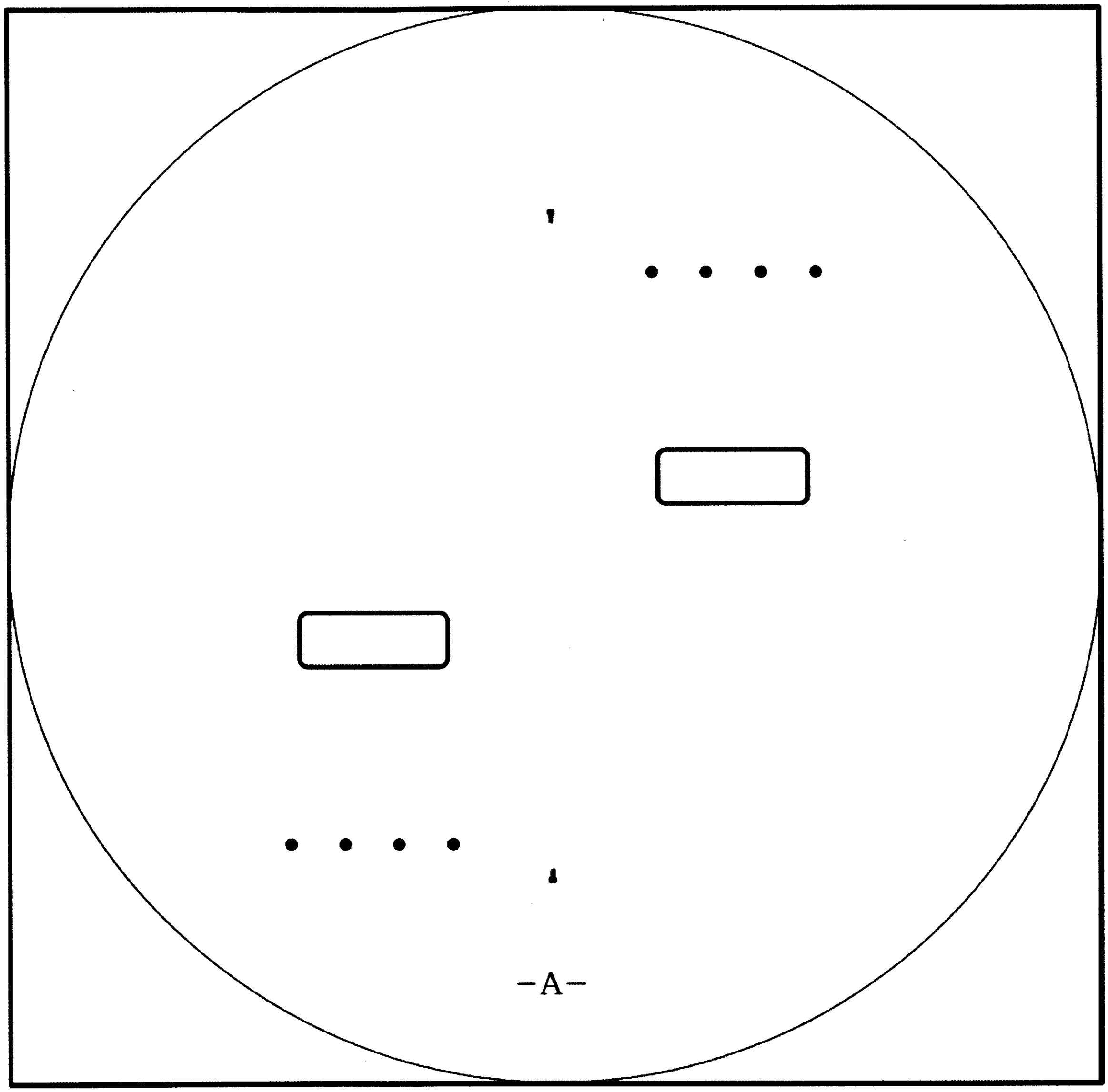

Figure D.2: Sequential Injection Microreactor: Back

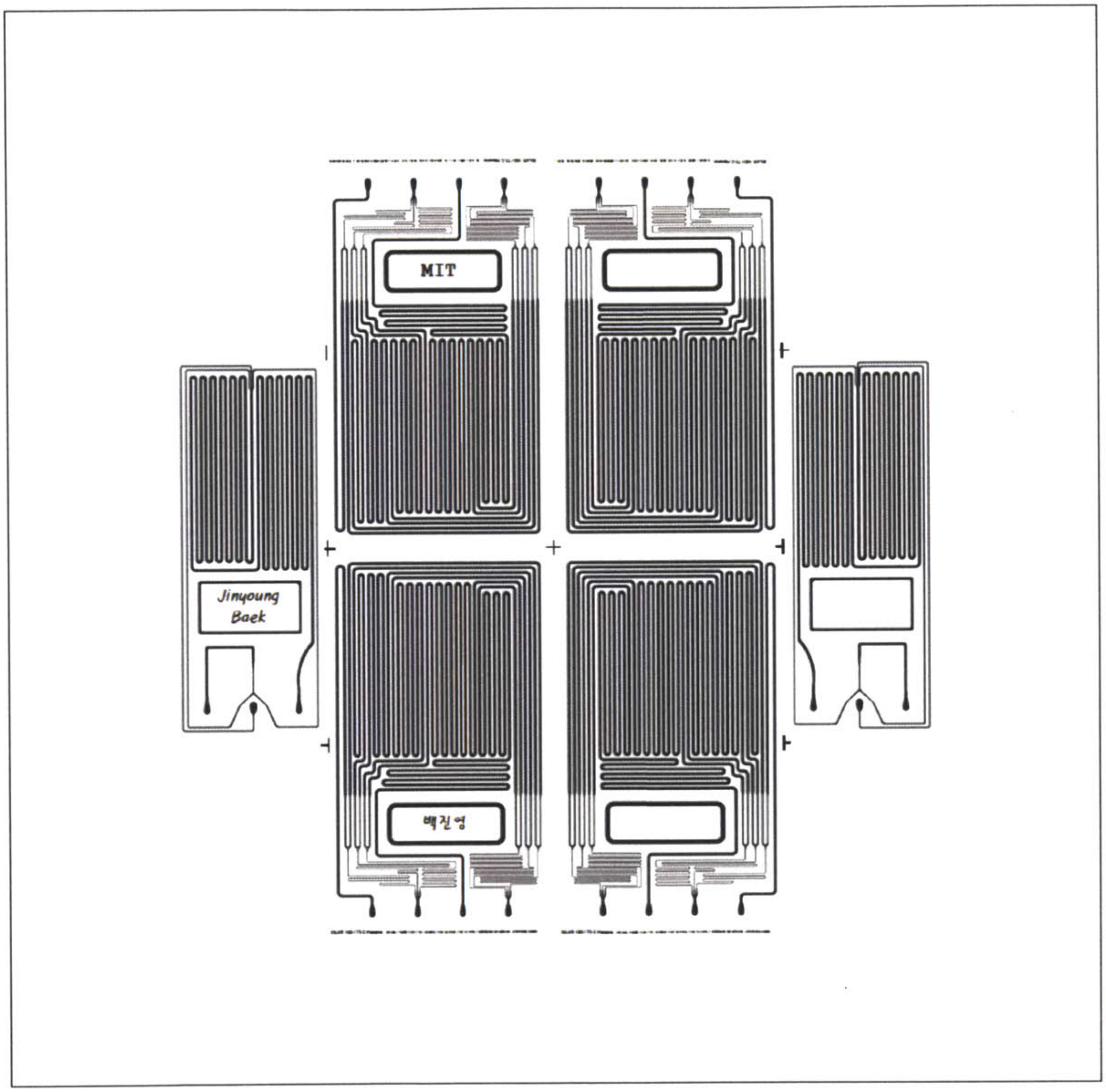

Figure D.3: Sequential (SILAR) Injection Microreactor. 6-additional injections at cold temperature : Front

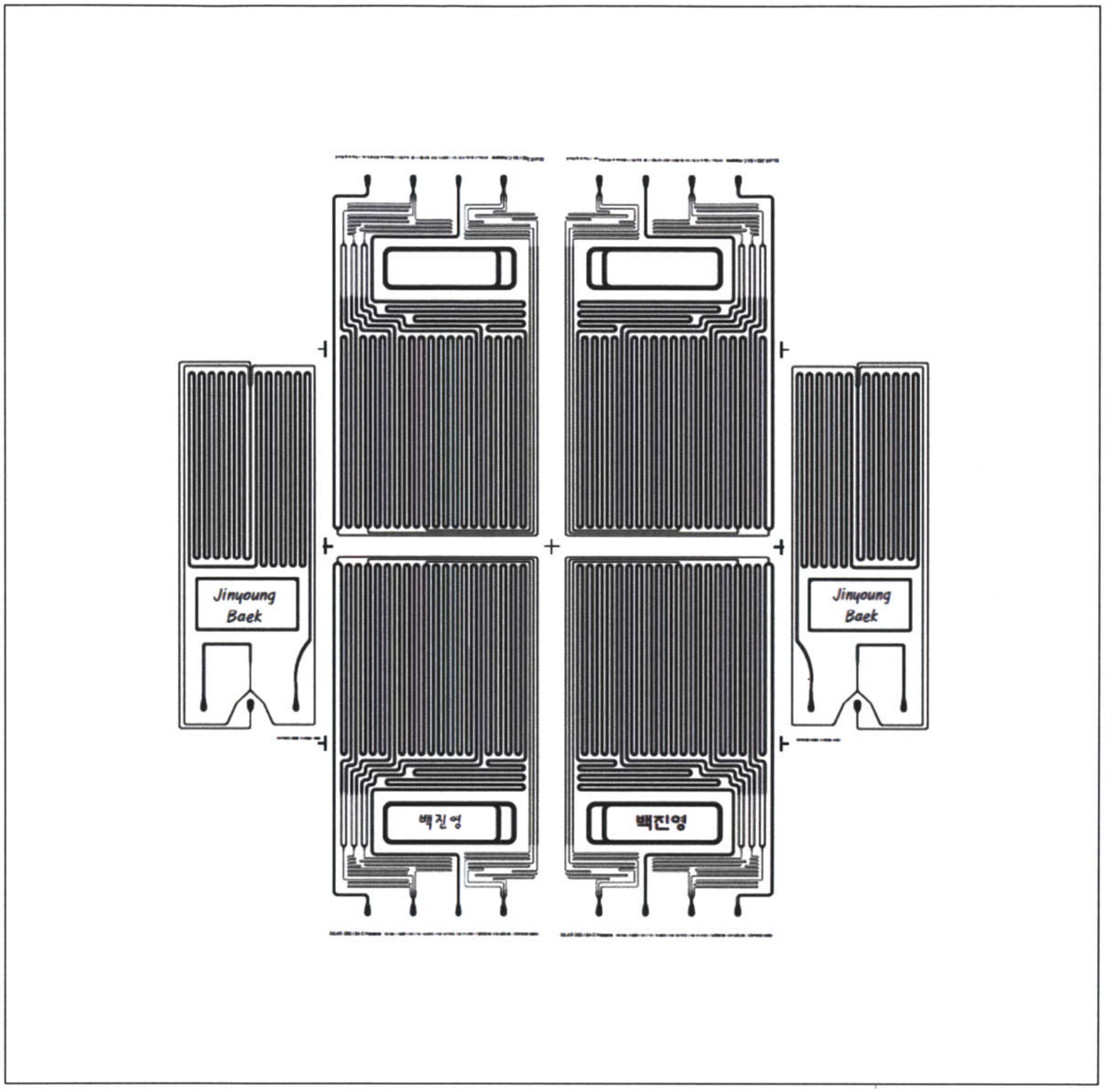

Figure D.4: Sequential (SILAR) Injection Microreactor. 3-additional injections at cold temperature and 3-additional injections at hot temperature : Front

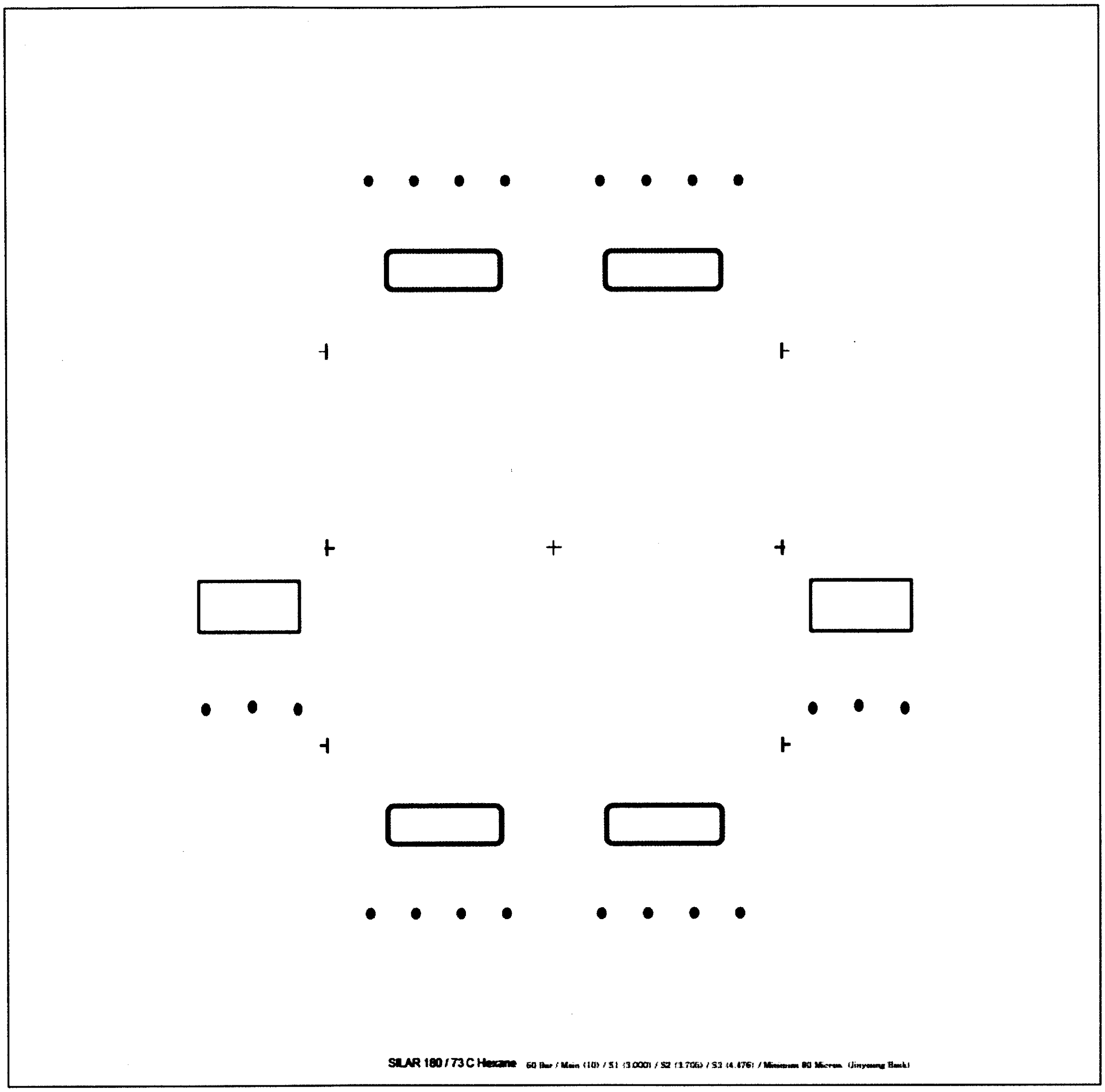

Figure D.5: Sequential (SILAR) Injection Microreactor: Back side mask for Figure 2B-3 and 4

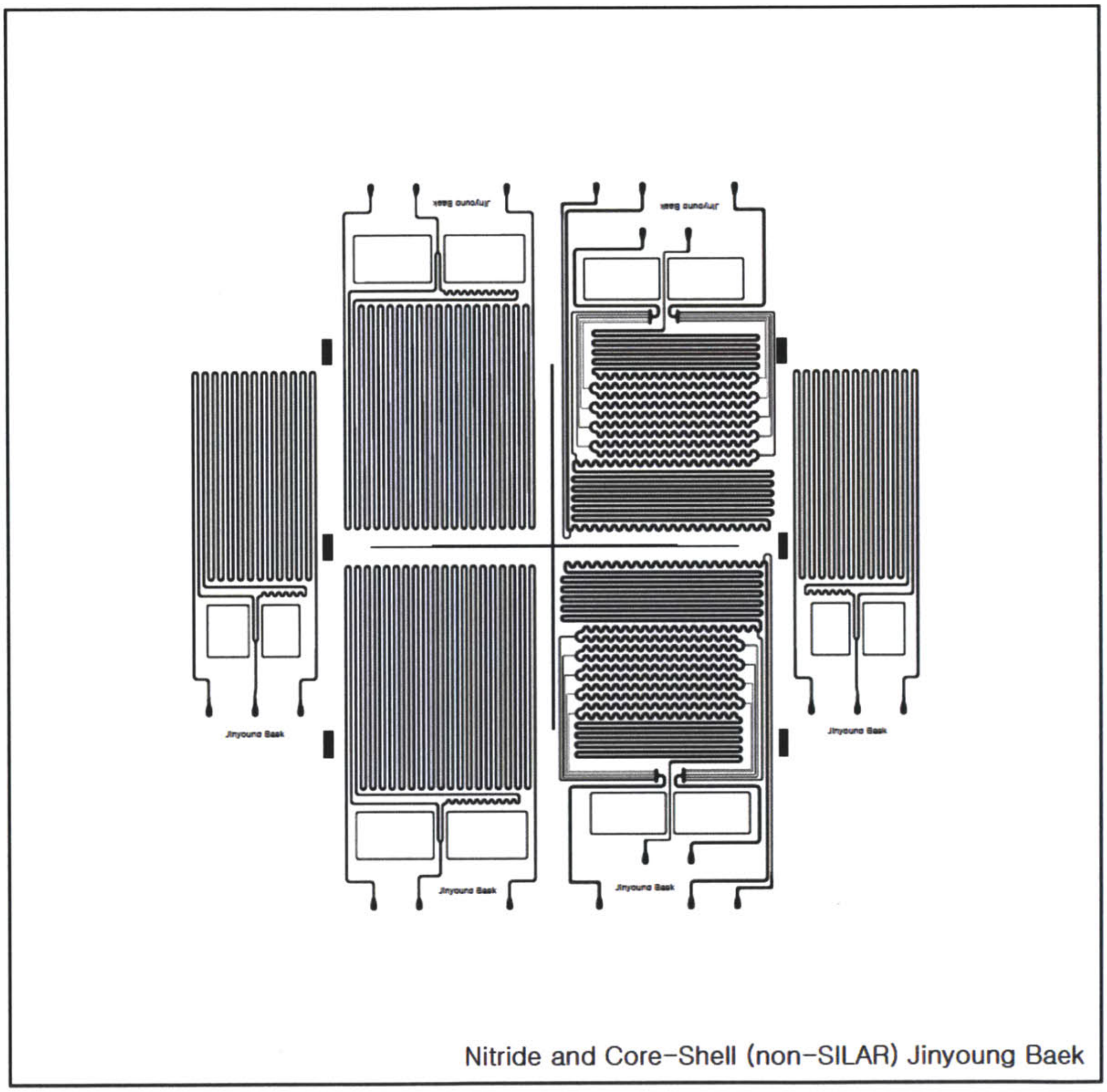

Figure D.6: Microreactor for nitride synthesis, and side injection microreactors: Front

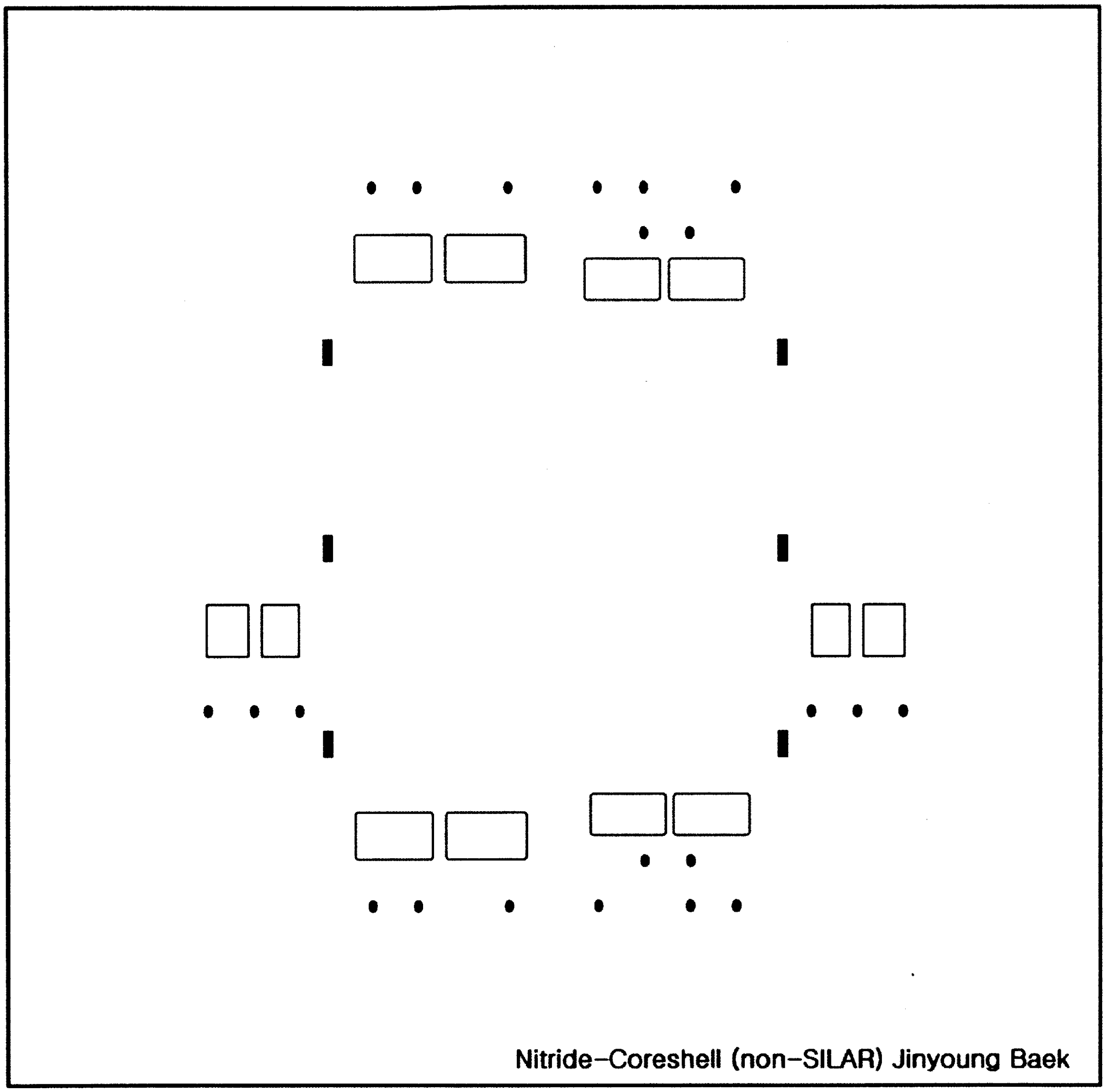

Figure D.7: Microreactor for nitride synthesis, and side injection microreactors: Back

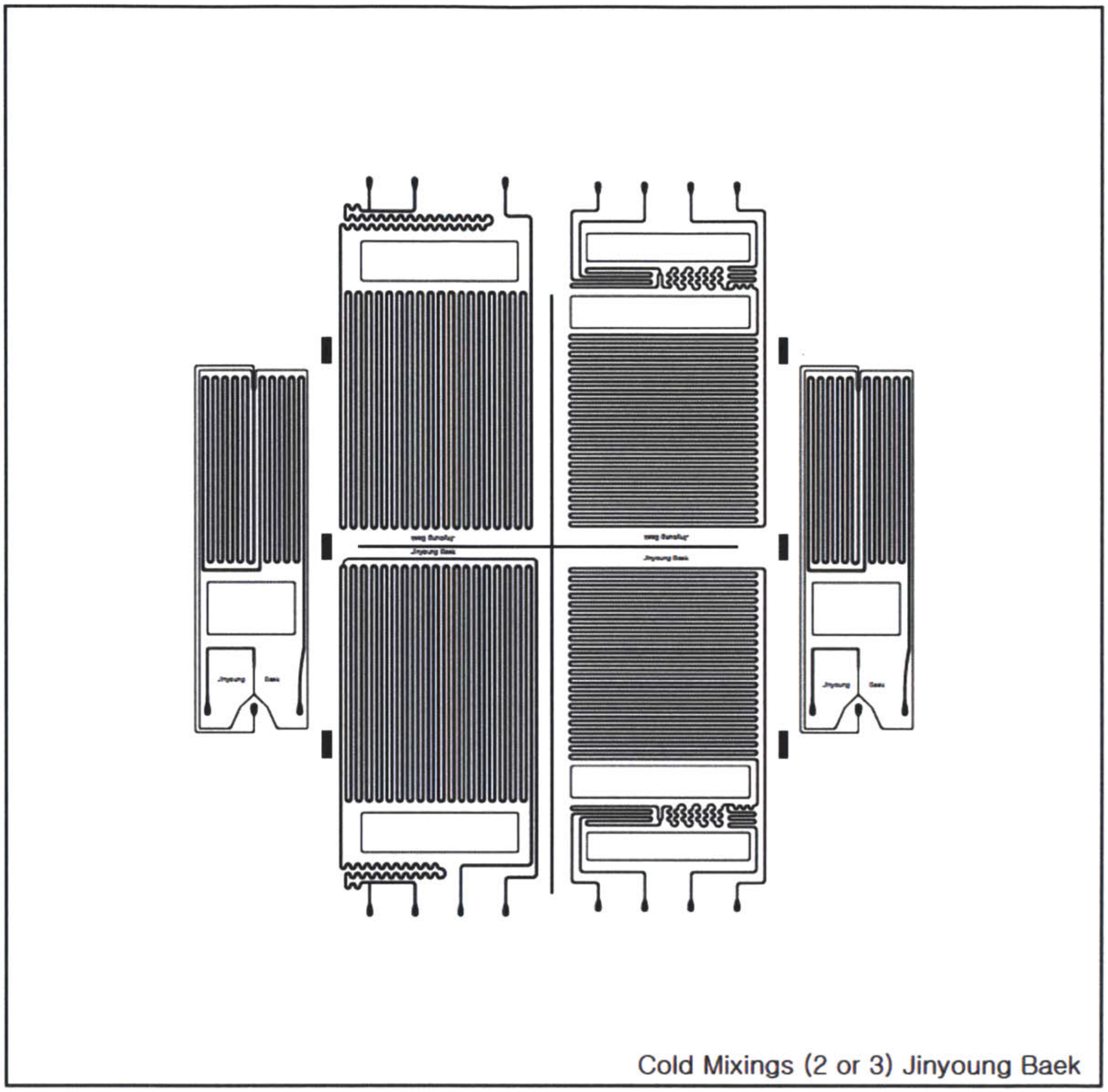

Figure D.8: Mixing reactors: Front

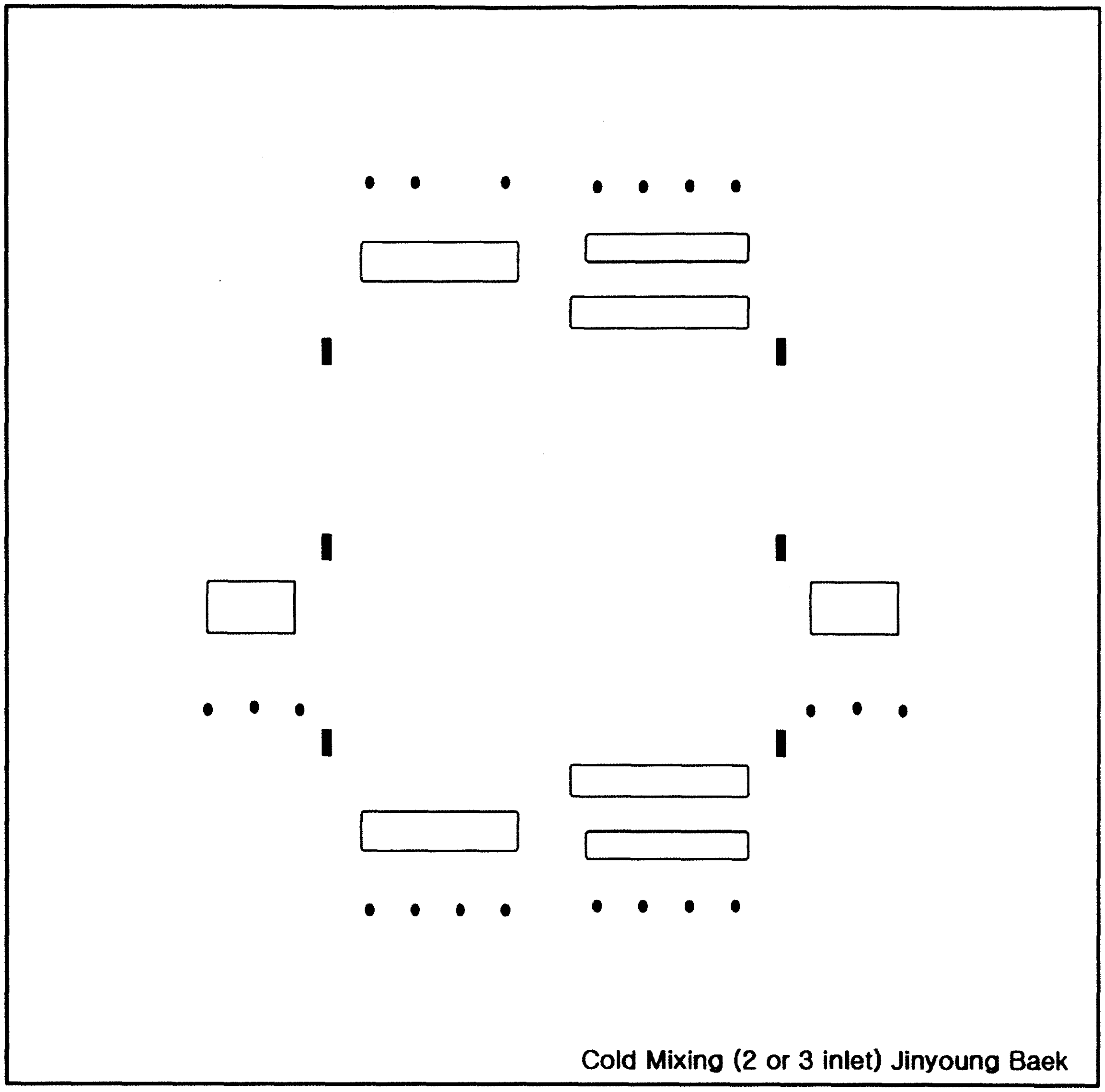

Figure D.9: Mixing reactors: Back

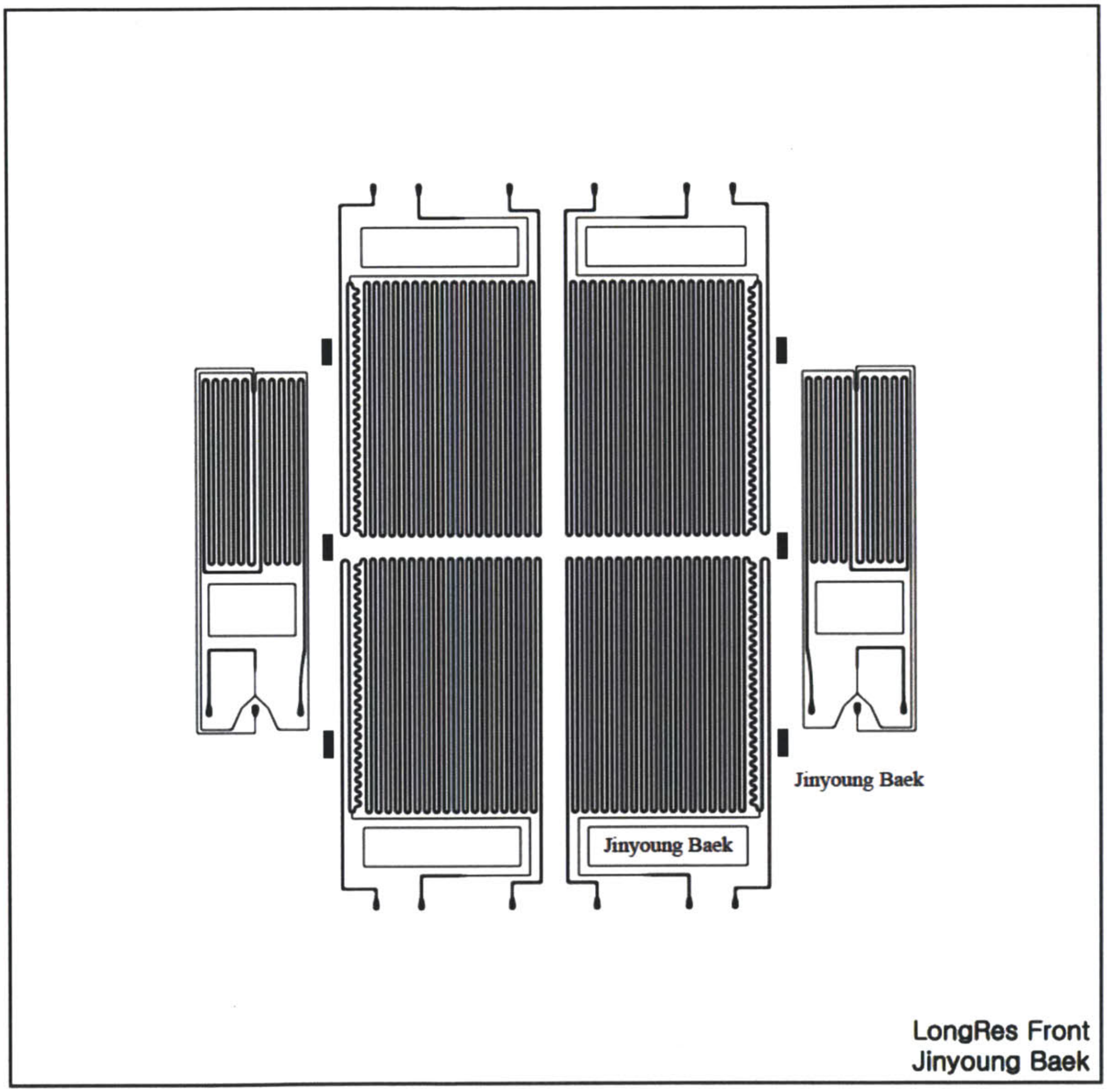

Figure D.10: Long residence time microreactor: Front

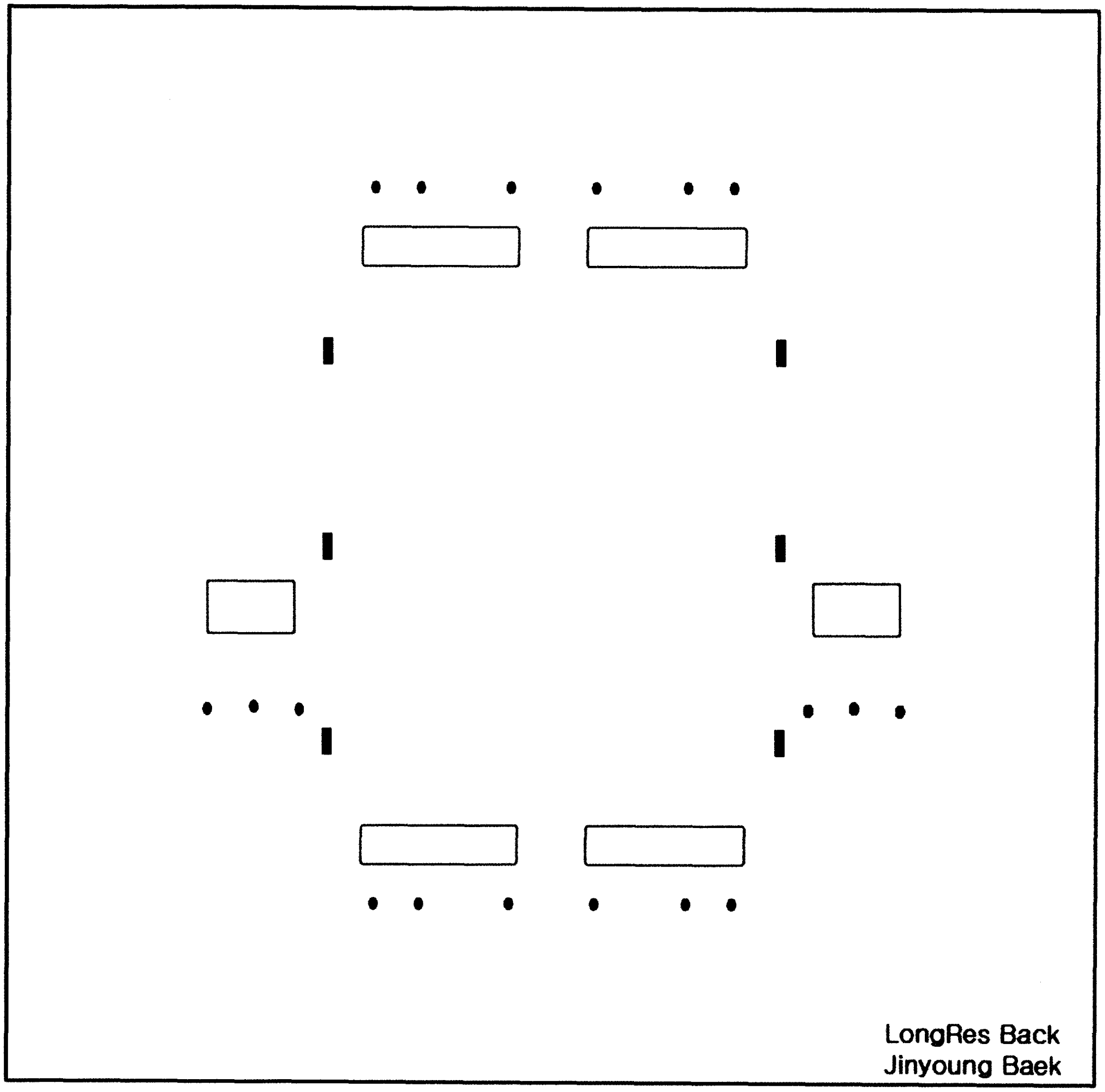

Figure D.11: Long residence time microreactor: Back

Appendix E. Fabrication procedure (The newest procedure, 2012)

Starting material: 1 double-side polished 6-inch silicon wafer with 1 micron oxide.

1 6-inch Pyrex wafer

Table E.1: Step-by-Step fabrication procedure

	Lab	Equipment	Description
1. Deposit thick oxides on the wafer			
1.1	TRL	acidhood	Piranha to clean wafers
1.2	ICL	DCVD	Deposit silicon oxides on the wafer
2. Photo-lithography (Front)			
2.1	TRL	HMDS	Coat with HMDS
2.2	TRL	coater	Spin Coat resist1 to 1 um
2.3	TRL	prebake	Bake 90 deg. C for 30minutes.
2.4	TRL	EV1	Expose resist for 2 seconds to UV
2.5	TRL	photowet	Development 1 minutes
2.6	TRL	postbake	Postbake at 110 deg. C for 30 minutes

3. Dry Reactive Ion Etching

3.1	TRL	acidhood	BOE etch for 40 minutes Need to protect the back-side of the wafer with Blue tapes.
3.2	TRL	STS2	STS etch, recipe JBETCH, about 100um
3.3	TRL	STS2	STS etch, after protect the small channels with Kapton tapes. recipe JBETCH, about 350um
3.4	TRL	acid hood	Remove resist using piranha (10-12 min)

4. Photo-lithography (Back)

4.1	TRL	HMDS	Coat with HMDS
4.2	TRL	coater	Spin Coat resist1 to 5 um
4.3	TRL	prebake	Bake 90 deg. C for 30minutes.
4.4	TRL	EV1	Expose resist for 15 seconds to UV
4.5	TRL	photowet	Development 3 minutes
4.6	TRL	postbake	Postbake at 110 deg. C for 30 minutes

5. Dry Reactive Ion Etching

5.1	TRL	acidhood	BOE etch for 10 minutes Better to protect the front-side of the wafer with Blue tapes. (But not necessary)
5.2	TRL	STS2	STS etch, recipe JBETCH, about 250 – 300 um
5.4	TRL	acidhood	Remove resist using piranha (10-12 min)

6. Strip-off and Cleaning

6.1	TRL	acidhood	Cleaning with piranha
6.2	TRL	acidhood	BOE for 40 mins.

7. Thermal Silicon-Oxide Growth

7.1	TRL	HMDS	Coat with HMDS
7.2	TRL	furnace tubeA2	furnace tubeA2 Thermal oxide growth (5000 A). (Wet oxidation process)

8. Cleaning and Bonding

8.1	TRL	acidhood	Cleaning with piranha (Red Process)
8.2	TRL	evaligner	align/contact
8.3	TRL	evbonder	anodic bond (400 deg.C, 1000V)
8.4	TRL	EV1	Expose resist for 15 seconds to UV
8.5	TRL	photowet	Development 3 minutes
8.6	TRL	postbake	Postbake at 110 deg. C for 30 minutes

9. Cutting

9.1	ICL	diesaw	Cutting with diesaw

Appendix F. Scale-up of microreactor / long residence time continuous reactor.

We tested scale-up of microfluidic system for nanocrystal synthesis by building a system consisting of different stainless steel tubes and an oil bath (Figure F.1). We synthesized CdSe nanocrystals using two tubes with different diameters and volumes. We controlled residence times and temperatures. We were able to synthesize CdSe nanocrystals with a FWHM of 24 nm from two different tubes: an inner diameter of 0.02" and 0.03". Since the length of the tubes were the same to each other, and therefore the tube volumes were different, the flowrates of the solutions were controlled to obtain a same residence time. The qualities of CdSe from two different tubes were similar to each other in terms of the size, and the size distribution. This result indicates that in this sub-milimeter tube scale, synthetic chemistry of CdSe synthesis could be more important than improvement of mixing properties. We used a 3:1 mixture of 1-octadecene and oleylamine as the solvent. This work was collaborated with Flurin Hanseler.

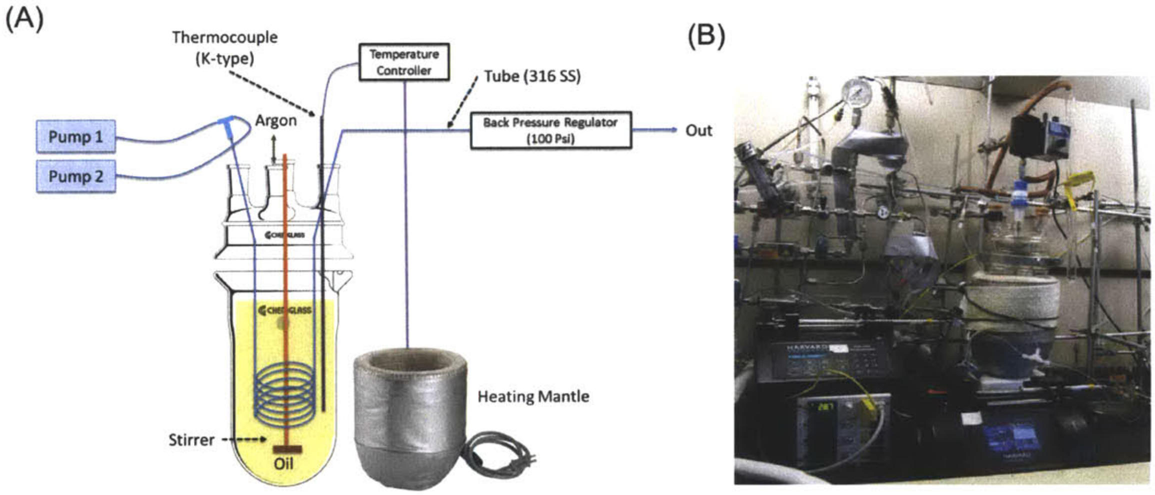

Figure F.1: System for scale-up of microfluidic system.

We also investigated effects of surfactants on particle growth. We were able to observe size defocusing only when we used a strong binding surfactant, tri-n-octylphosphine oxide (TOPO) (figure F.2). We were not able to observe any size broadening behavior, potentially caused by Ostwald ripening, when oleylamine or oleic acid was used as the surfactants. The reaction temperature was 290 °C, and the maximum residence time was 100 minutes.

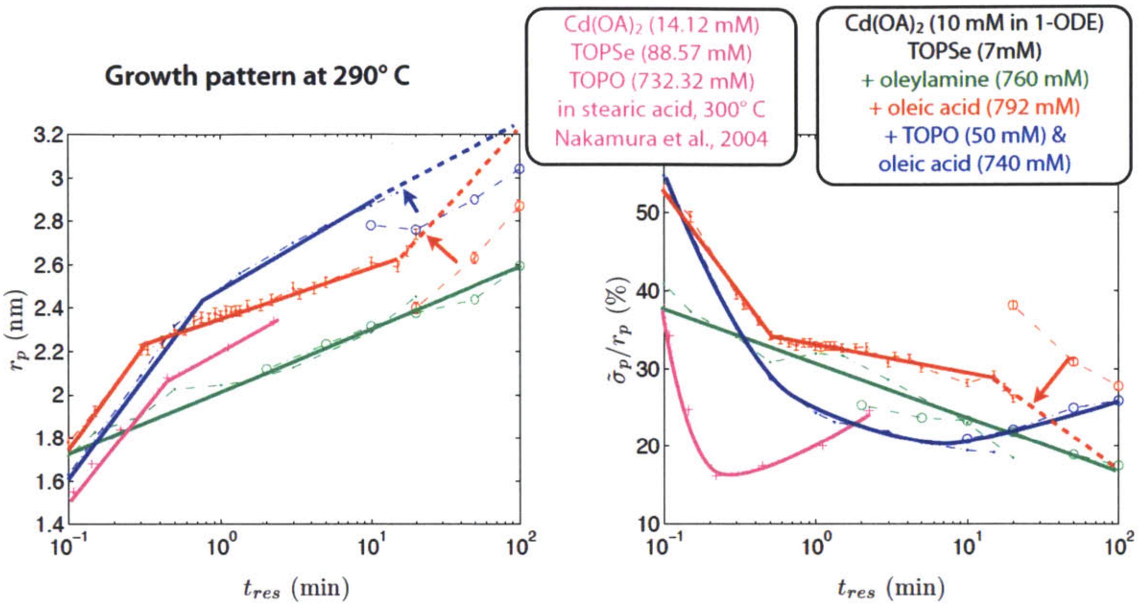

Figure F.2: Effects of different surfactants on CdSe particle growth. Oleylamine, oleic acid, and TOPO were tested. Size broadening behavior was observed only when TOPO was used as the surfactant. This work was collaborated with Flurin Hanseler.